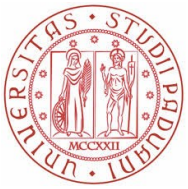

UNIVERSITÀ DEGLI STUDI DI PADOVA

DIPARTIMENTO DI SCIENZE CHIMICHE

CORSO DI LAUREA MAGISTRALE IN CHIMICA

TESI DI LAUREA MAGISTRALE

Controlled Radical Polymerization Enabled by Electrochemically Mediated Photoredox Catalysis

Relatore: Dr. Marco Fantin

Controrelatore: Prof. Andrea Sartorel

Laureando: Tobia Casadei

ANNO ACCADEMICO 2023/2024

Contents

Glossary of Acronyms

ATRP	Atom Transfer Radical Polymerization
BET	Back Electron Transfer
BrACN	Bromoacetonitrile
CDET	Concerted DET
CDTPA	4-cyano-4-[(dodecylsulfanylthiocarbonyl)sulfanyl]pentanoic acid
CE	Counter Electrode
conPET	Consecutive Photoinduced Electron Transfer
CRP	Controlled Radical Polymerization
CTA	Chain Transfer Agent
CV	Cyclic Voltammetry
Đ	Dispersity
DET	Dissociative Electro Transfer
DMF	*N*,*N*-Dimethylformamide
DP	Degree of Polymerization
DT	Degenrative Transfer
*e*ATRP	Electrochemically mediated Atom Transfer Radical Polymerization
EBP	Ethyl 2-bromopropionate
EC	Electrocatalyst
E_{pc}	Cathodic peak potential
e-PRC	Electrochemically Activated Photoredox Catalysis
*e*RAFT	Electrochemically mediated Reversibile Addition-Fragmentation ChainTransfer
ET	Electron Transfer
FRP	Free Radical Polymerization

GC	Glassy Carbon
GPC	Gel Permeation Chromatrography
HAT	Hydrogen Atom Transfer
IC	Internal Conversion
i_{pc}	Cathodic peak current intensity
iPEC	Interface Photo-Electrochemistry
ISC	Intersystem Crossing
ISET	Inner Sphere Electron Transfer
LAM	Less Active Monomer
LRP	Living Radical Polymerization
MAM	More Active Monomer
MBiB	Methylα-bromoisobutyrate
EBiB	Ethyl α-bromoisobutyrate
MBP	Methyl 2-bromopropionate
MCB	Methyl 4-chlorobenzoate
MMA	Methyl Methacrylate
M	Monomer
M_n	Average molar weight
M_w	Weighted average molar weight
NMP	Nitroxide Mediated Polymerization
NMR	Nuclear Magnetic Resonance
OQP	Oxidative Quenching Pathway
OSET	Outer Sphere Electron Transfer
PC	Photocatalyst
PDI	*N*,*N*'-Bis(2,6-diisopropylphenyl)-3,4,9,10-perylenetetracarboxylic Diimide

PET-*e*RAFT	Photoinduced Electron/Energy Transfer *e*RAFT
PET	Photoinduced Electron Transfer
PET-RAFT	Photoinduced Electron/Energy Transfer RAFT
PMMA	Poly(methyl methacrylate)
PRC	Photoredox Catalysis
PRE	Persistent Radical Effect
RAFT	Reversibile Addition-Fragmentation Chain Transfer
RDE	Rotating Disk Electrode
RDRP	Reversible-Deactivation Radical Polymerization
RE	Reference Electrode
RP	Radical Polymerization
RQP	Reductive Quenching Pathway
RX	Organic halide
SCE	Saturated calomel electrode
SDET	Stepwise DET
SET	Single Electron Transfer
SRP	Standard reduction potential
TBATFB	Tetrabuthyl ammonium tetrafluoroborate
UV-Vis	Ultraviolet - Visible
WE	Working Electrode

1. Introduction

Modern science is characterized by the intricate interplay of diverse disciplines, where boundaries blur and systems overlap in often unexpected ways. This complexity is particularly evident in chemistry, where molecular interactions underpin a vast array of phenomena.

Electricity powers our world, driving countless processes and devices essential to everyday life. Light, the foundation of photosynthesis and vision, plays a pivotal role in natural and artificial systems alike. Polymers, ubiquitous in nature and technology, form the basis of materials that shape our environment. This thesis explores the convergence of these fundamental elements investigating the synergistic interactions at the molecular level between electrochemistry and light, to develop novel approaches in controlled polymer synthesis.

This thesis explores the application of electro-photo catalytic (e-PRC) systems in reversible-deactivation radical polymerizations (RDRPs). RDRPs enable the synthesis of well-defined polymers by utilizing radical species that reversibly switch between active and dormant states. This controlled growth process results in polymers with narrow dispersity ($Đ < 1.5$) and defined molecular weight (M_n), while minimizing unwanted termination reactions and allowing for polymerization to be paused and restarted as needed.

e-PRC combines the injection of one electron (or hole) and one photon in a single catalytic cycle, effectively conducting photo-redox catalysis with a photoexcited catalyst in a reduced or oxidized form. This approach builds upon traditional photo-redox catalysis (PRC), aiming to enable challenging chemical reactions under mild conditions.
Our research focuses on *N*,*N*-bis(2,6-diisopropylphenyl)perylene-3,4,9,10-bis(dicarboximide) (PDI) as a catalyst. The photoexcitation of the PDI radical anion ($PDI^{\bullet-}$) could potentially facilitate reactions using low-energy red light and gentle electrochemical potentials, expanding the scope of accessible chemical transformations.
Motivated by the constructive interaction of light and electrical energy, we conducted a comprehensive investigation into the photochemical and electrochemical properties of PDI. Our primary goal was to evaluate its capacity to react with R-X substrates (with X = halogen atom or sulfur functional group) to generate radicals suitable for new polymerization pathways, particularly RDRPs. These processes require continuous cycles of radical generation and deactivation, demanding a catalyst that remains both stable and active throughout the reaction.

This work bridges the fields of photoredox catalysis, electrochemistry, and polymer science, aiming to develop novel, efficient, and controllable polymerization methods. By harnessing the combined power of light and electrons through PDI catalysis, we seek to expand the toolbox of synthetic polymer chemistry and pave the way for new materials with tailored properties. The insights gained from this research could potentially lead to more sustainable and energy-efficient polymerization processes, contributing to the broader field of materials science and green chemistry.

1.1. Photoelectrocatalysis

Single electron transfer in photoredox catalysis

Single electron transfer (SET) plays a fundamental role in many organic chemistry reactions. One could argue that life as we know it places its roots in SET driven reactions since it is Nature's solution to conduct photosynthesis. Over the centuries chemistry has evolved in the attempt to mimic Nature. Stripping down photosynthesis of its complexity we can reduce it to the bare concept of a photocatalyst (PC) absorbing visible light, entering an excited state, and thus enabling a redox reaction via electron transfer. The process of making use of a photoexcited PC to access redox reactivity goes by the name of Photoredox catalysis (PRC). A PRC process exploits the gain in energy after photon absorption (Scheme 1) to access higher energy states. The energy gained greatly depends on the accessed electronic state and the stability of the molecules in such states. Initial reports of PRC go back to the 1980s[1–4], and is currently living a true renaissance [5–7].

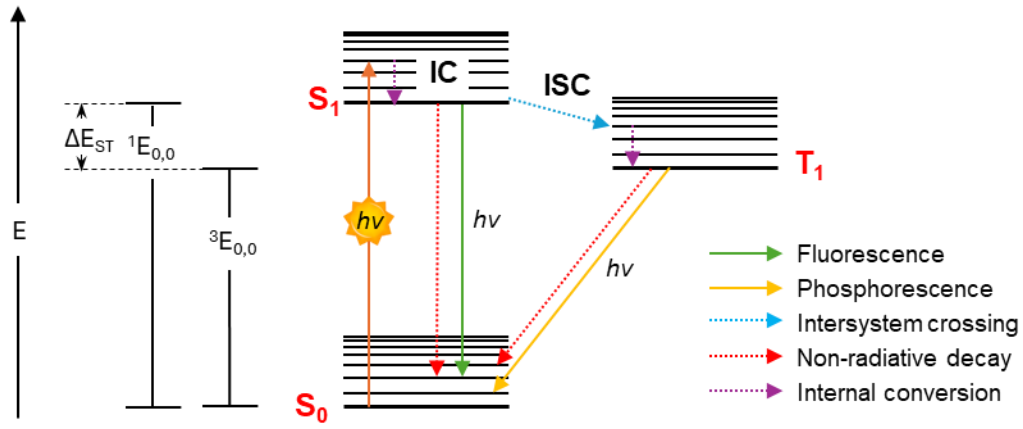

Scheme 1. Jablonski diagram of the photphysical process and Redox potentials after photon absorption by a generic molecule.

Several catalysts capable of enabling PRC reactions have been designed: Ruthenium and Iridium complexes [8–14], but also more sustainable organocatalysts such as eosin Y or acridinium salts [15–20]. PRC presents many interesting features [21], most notably the possibility to access high redox potentials

by simply shining light and the fact that it is possible to selectively excite the PC without interfering with other species in solution.

Nevertheless, PRC suffers from some limitations: the thermodynamic driving force of a PC is limited by the energy of visible photons (3,1-1,8 eV; 400nm-700nm); loss in excitation-energy from light absorption by the PC to substrate activation typically amounts to at least 25% (often around 50%) of the initial photon energy due to accumulated losses from internal conversion (IC), intersystem crossing (ISC) and the oxidation or reduction of the catalyst itself [22]; moreover increasing the photon energy is often not an option because many organic substrates directly absorb UV light, which can cause photodamage, undesired side reactions, and photo-bleaching of the PC. PRC can proceed via either oxidative or reductive quenching pathways, which are described in detail in section 1.3.2.4 in the context of photo-mediated polymerizations.

Single electron transfer in electrocatalysis

Another effective way to access SET reactivity is synthetic electrochemistry. The use of electricity to perform chemical reactions dates to the 1800s with Faraday's electrolysis experiments[23] and Kolbe's decarboxylation[24].

A generic electrocatalytic reaction setup consists of a power supply connected to a cathode and an anode inserted into a solution containing an electrolyte. By applying an electrical potential, we induce electron gain or loss at an electrode, resulting in reduction or oxidation reactions. Based on the location of electron transfer, these reactions can be divided into direct and indirect electrolysis. In direct electrolysis, the substrate directly gains or loses electrons at the electrode, leading to a heterogeneous reaction (Figure 1, left). Indirect electrolysis involves a redox mediator (electrocatalyst, EC) that transfers electrons between the substrate and the electrode, facilitating the reaction (Figure 1, right). Electrocatalytic methods provide a series of appealing and interesting features when compared to traditional organic synthesis. The use of electric current reduces the use of chemicals, gives access to milder conditions, limits energy consumption, avoids the generation of reagent waste, and increases atom economy[25]. Additionally, when using electrochemistry, one gains control over the reaction through the modulation of electrode potential. This feature gives access to a wider range of redox potential (exceeding the intrinsic limitations of photochemistry) and improves tolerance towards functional groups.

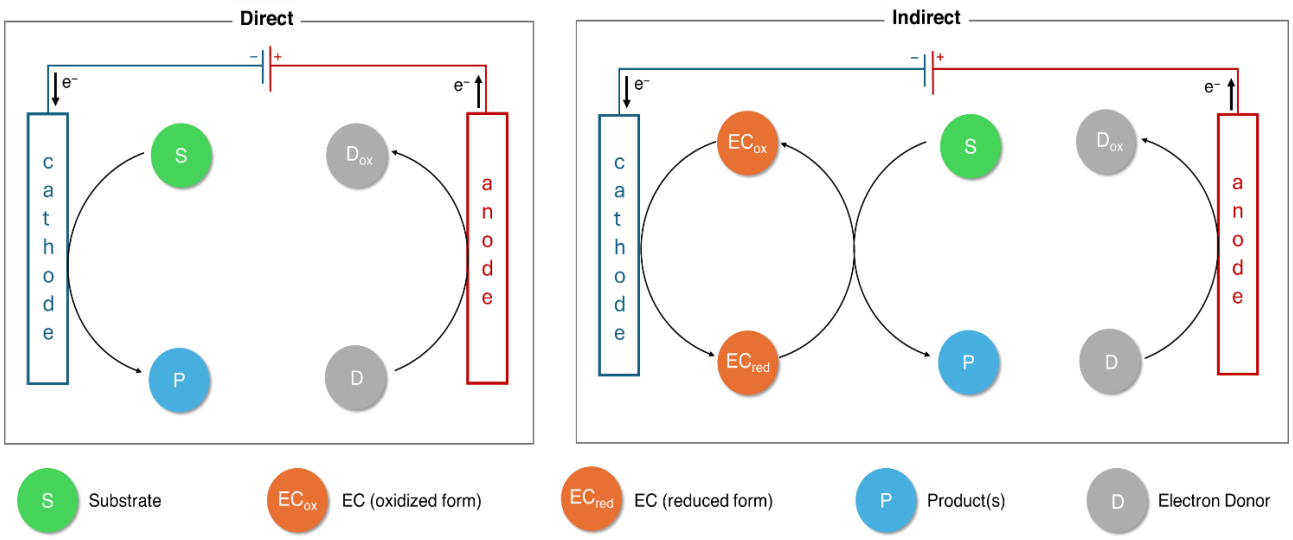

Figure 1. Schematic representation of direct and indirect electrocatalytic processes

However, electrochemical methods face limitations. Direct electrolysis has an inherent heterogeneous nature since the active species are generated at the electrode surface. Because of this reason the presence of excess electrons or holes in the electrode is often the rule. The generation of a high concentration of highly reactive species in the electrode diffusion layer can lead to side reactions such as coupling or undesired electron transfers before the active species are able to migrate to the solution. Additionally, the electrode surface can become contaminated by intermediates from starting material decomposition, leading to passivation.

In indirect electrolysis the reactions proceed away from the electrode surface. However the thermodynamic energy of mediators is limited by their redox potential, which is in turn limited by the electrochemical window imposed by the reduction/oxidation of the solvent.

In complex chemical reactions, a high potential may be required to produce active species, but at such extreme potentials the reaction can become poorly controlled due to over-oxidation or over-reduction processes that significantly reduce selectivity.

Alternative pathways for highly challenging reactions

To engage challenging moieties synthetic chemists have thus far relied on techniques that bypass direct SET activation. Such techniques have typically involved the ad-hoc design of PCs or ECs with tailored activity for a specific substrate. Taking for example C−H or carbonyl activation, these strategies can include:

i) in situ generated radicals or radical ions that undergo hydrogen atom transfer (HAT) chemistry.[26,27]

ii) photochemical excited states that directly engage in HAT chemistry.[28,29]

iii) proton-coupled electron transfer (PCET)[30,31]

Alternatively, to drive thermodynamically increasingly challenging reactions with visible light and well-established photocatalysts, the synthetically oriented photoredox community recently started to exploit multi-photon excitation. By this strategy, the thermodynamic obstacles are overcome by combining the energy of two (or more) photons per catalytic turnover in what is called consecutive photoinduced electron transfer (conPET). This procedure mimics Nature's own solution to the energy problem. Plants and photosynthetic bacteria efficiently capture two photons through type-I and type-II reaction centers: the first photon excites the primary electron donor, transferring an electron to the primary acceptor in picoseconds and the second photon further drives electron transfer through the system, ultimately leading to ATP formation[32].

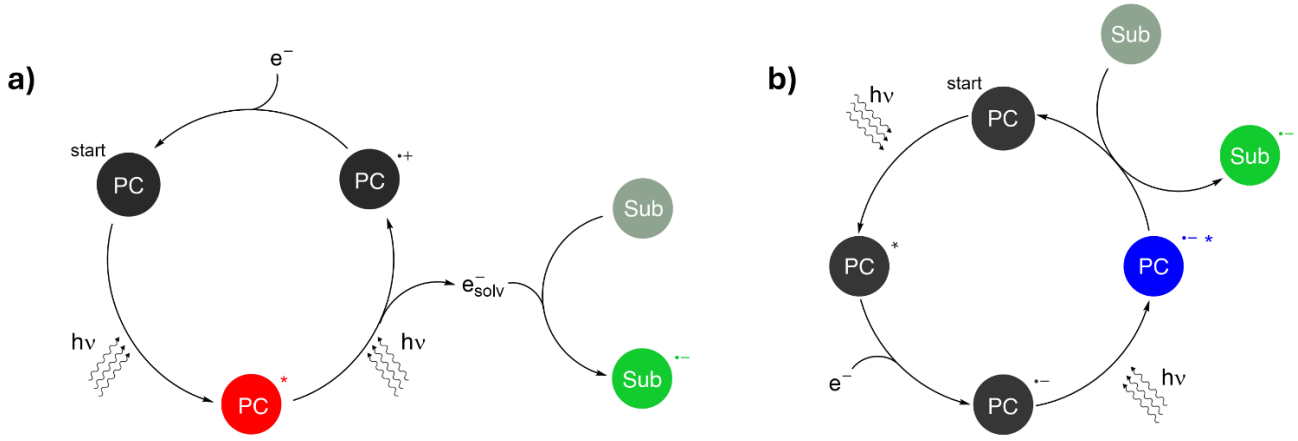

Scheme 2. a) Simplified reaction via high excited (triplet) states. b) Reaction via electronically excited one-electron reduced species. In both cases e⁻ can be provided by a sacrificial donor or by an electrode.

Multi-photon processes have been deeply studied. Scheme 2a shows one of the simplest two-photon reduction mechanisms: after the first photon absorption the excited state catalyst (*PC) absorbs another photon to expel a solvated electron that acts as the reductant. The apparent simplicity of this process is complicated by the short excited state lifetimes of *PC (µs-ns range) causing a need for high excitation densities[33]. Moreover, a sacrificial electron donor is typically used to regenerate the starting state of the catalyst. Scheme 2b presents a more efficient method, generating a stable radical anion first, then a potent reductant through subsequent excitation. Even if the stability of $PC^{\bullet-}$ make the latter process much more efficient than the one presented in Scheme 2a, this requires high excitation energies, specialized photocatalysts, and sacrificial redox reagents, which can reduce atom economy and reaction selectivity[34,35].

To access thermodynamically challenging reactions, electrochemistry has relied on inner sphere electron transfer (ISET) methods, which require specific interactions between the catalyst and substrate to lower the barrier of (electro)chemical transformations. ISET typically requires an *ad hoc* designed metal catalysts that interact specifically with the substrate, but these catalysts are often prone to catalyzing unwanted side reactions with radicals[36].

The combination of photo- and electrocatalysis

Recognizing the tremendous advantages of PRC and electrocatalysis naturally leads to the question of how these processes might be combined into a single system. The concept of utilizing both light and electrical energy with the same catalyst, to overcome the intrinsic limitations of the two methods, takes form with the name of photo-electrocatalysis.

By IUPAC definition photo-electrochemistry envelopes all the techniques which combine photochemical and electrochemical methods for the study of the oxidation-reduction chemistry of both ground and excited states of molecules or ions.

The first explorations in the field of photo-electrochemistry date back to the 1980s, with the works of Moutet and Riverdy [37,38] and of Scheffold [39]. In the last decade the interest in photoelectrocatalysis sprouted[40–43] and presents itself as the consequential evolution of photocatalysis to approach complicated and useful synthetic challenges in organic chemistry. The combination of photonics and electrochemistry opens a plethora of possibilities and advantages along with a series of questions that propel scientific research and debate.

Photoelectrochemical processes can be systematically classified into three main classes[43], described in the next paragraphs.

1.1.1. Interface Photo-Electrochemistry (iPEC)

iPEC is the traditional and most developed form of photo-electrochemistry. When talking about iPEC we refer to an heterogenous photocatalytic process coupled with a potential bias which improves the electron(e^-)/hole(h^+) separation (i.e. photocathodes or photoanodes). Having better charge separation helps prevent charge recombination. The charge separation is generally achieved by interaction of radiation with a semiconductor deposited on a photoactive material[44–46].

iPEC processes can be direct or indirect (Figure 2). In the first case the reaction occurs directly on the photoelectrode, in the second circumstance the reaction is promoted by a mediator which is regenerated at the photoelectrode.

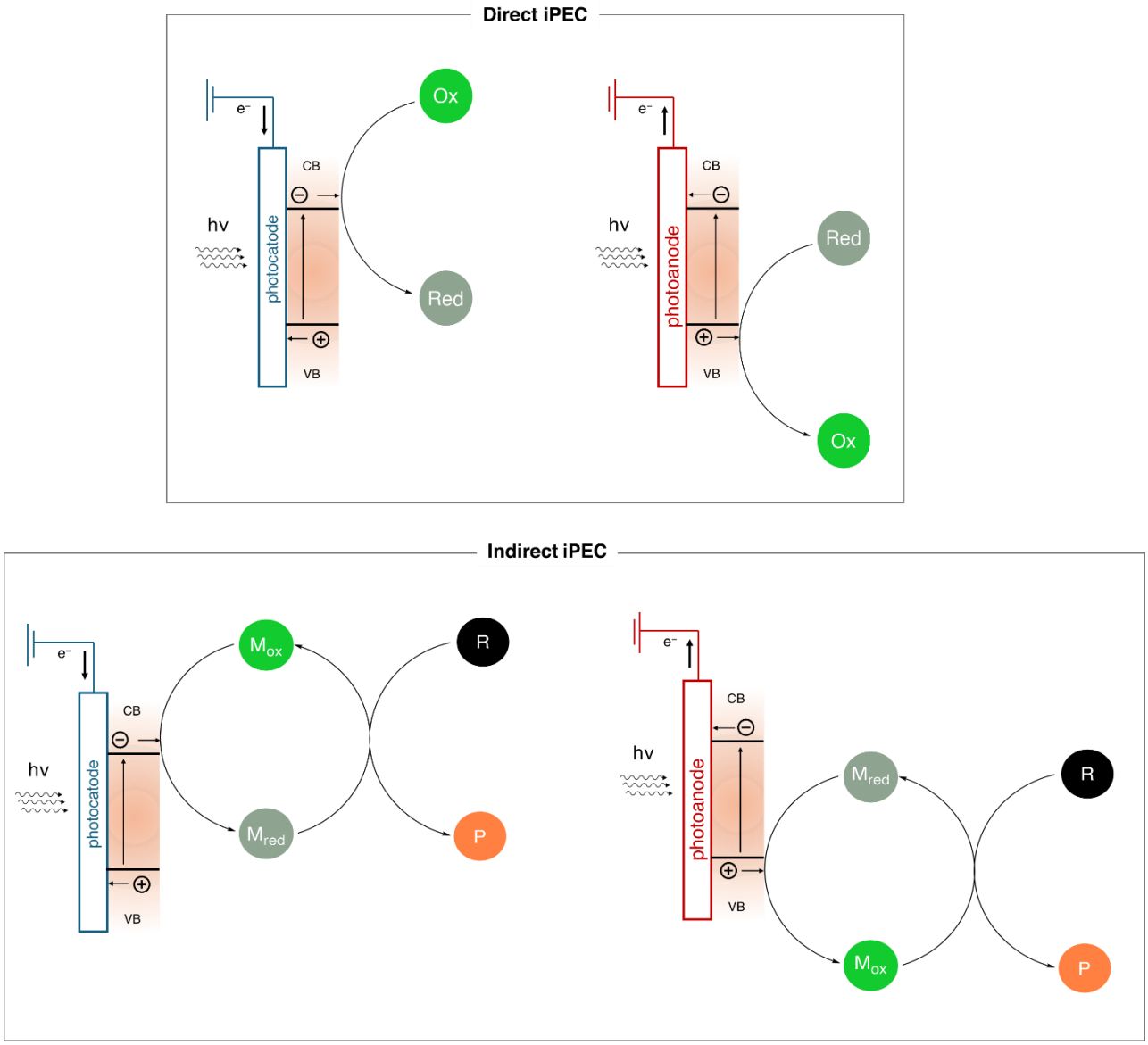

Figure 2. Schematic representation of, both oxidative and reductive, direct (left) and indirect (right) iPEC. CB and VB indicate conduction band and valence band, respectively.

Application of a potential bias allows to control the Fermi's energy level of the semiconductor thus maintaining the e^-/h^+ separation. iPEC is the most widespread application of photoelectrocatalysis so far, fueled by the constant uprise in the interest in photovoltaics.

1.1.2. Electrochemically Activated Photoredox Catalysis (e-PRC)

In e-PRC a photochemical event and an electrochemical step are combined in the same reaction pathway enhancing the energy balance of the catalytic cycle. This allows the injection of energy from one electron (or hole) and one photon into the catalyst, enabling unprecedented redox properties. e-PRC will be the focus of this thesis.

A typical e-PRC cycle is presented in Scheme 3 for net reductive and net oxidative reactions. The open-shell PC generated at the electrode absorbs a photon to access higher oxidative or reductive power. The photoexcited open shell intermediate reacts then with a substrate via SET, regenerating the ground state closed-shell PC which can reinitiate the cycle. e-PRC processes are influenced by several other factors that will be treated more exhaustively in following sections.

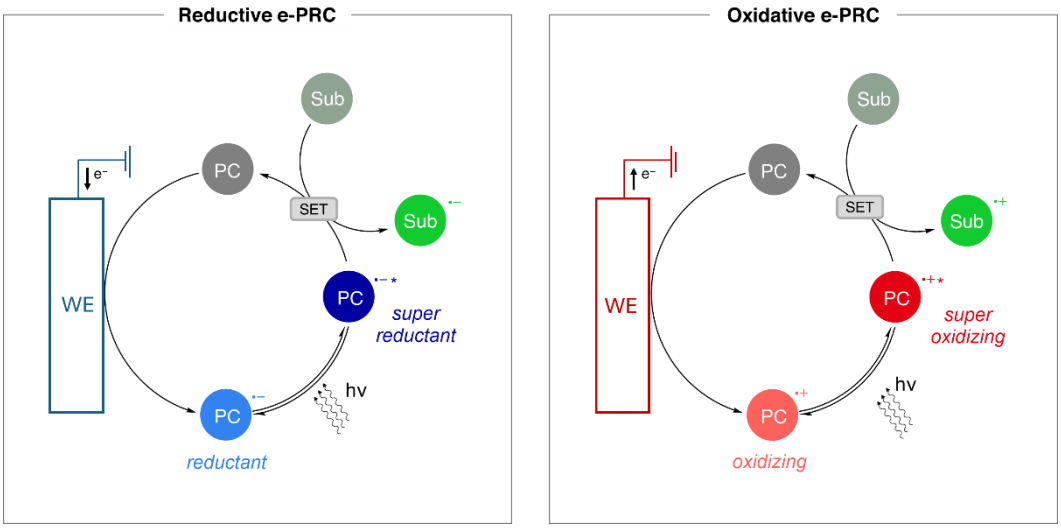

Scheme 3. Simplified schemes for e-PRC reductive (left) and oxidative (right) mechanisms. WE indicate the working electrode at which the ground state open shell catalyst is formed.

The photochemical and electrochemical events have independent roles and should not interfere with each other. In this approach an active open-shell species (radical anion or cation) generated at the electrode absorbs a photon.

The photoexcited open-shell intermediate displays outperforming redox properties thanks to the inversion of its populated SOMO and HOMO orbitals[40] (Figure 3).

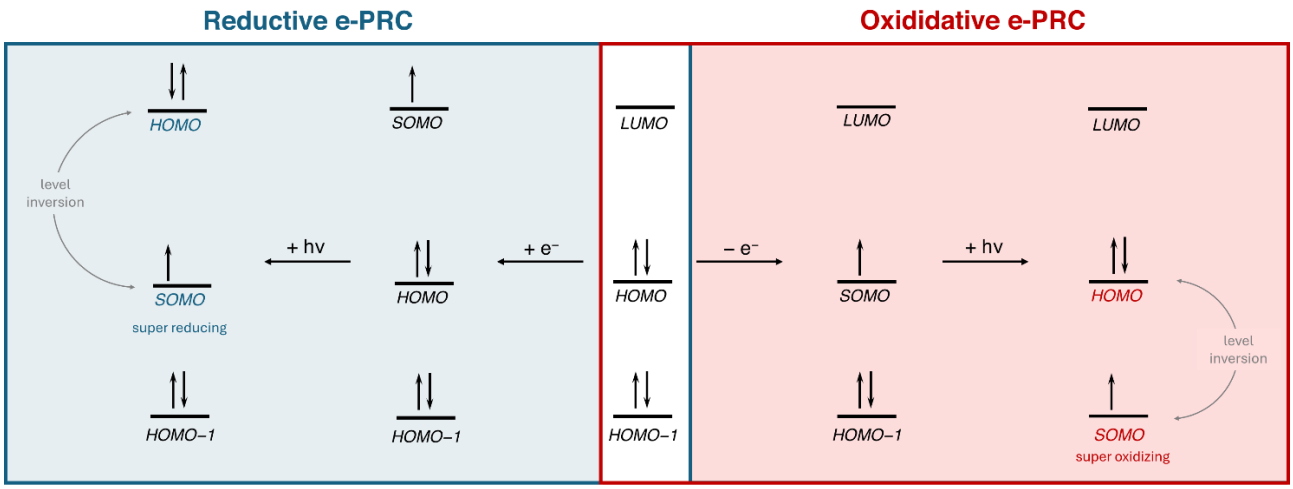

Figure 3. Molecular orbital picture of oxidative and reductive open-shell photocatalysis (elaborated from [41])

The structure of several e-PRC catalysts is displayed in Figure 4. In the case of e-PRC reductions the active form of the photocatalyst is generated at the electrode by injecting an electron. An example of this approach Wickens' group reported reduction of aryl halides using imide catalysts[47]. In this work the authors were able to reduce very inaccessible substrates, exceeding the reductive performance of Li^0 and Na^0 using a N-arylmaleimide (NMI) catalyst. More recently, König and Barham were able to selectively reduce C(sp^3)-O bonds using NMI derivatives and dicyanoantracene (DCA)[48].

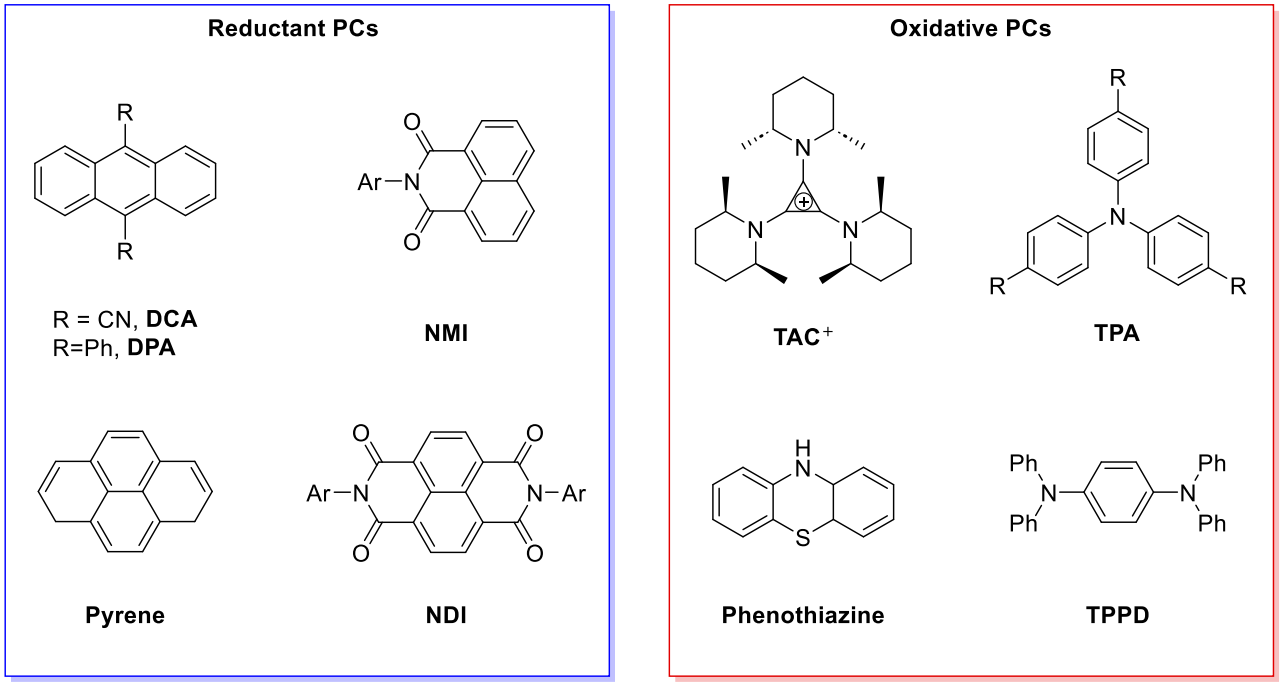

Figure 4. Catalysts used in reductive (left) and oxidative (right) e-PRC.

In addition to the reported examples of reductive reactions, e-PRC is a powerful tool to access oxidative chemistry. An example of this approach is the amination of various C-H bonds with a trisaminocyclopropenium (TAC) salt catalyst[49–51]. The TAC catalyst undergoes a single electron oxidation at the electrode to form an active radical dication $TAC^{\bullet 2+}$ which can absorb a visible light photon and access the excited state ($*TAC^{\bullet 2+}$). The $*TAC^{\bullet 2+}$ has an outstanding reduction potential of +3.33 V vs SCE, strong enough to oxidize challenging substrates such as benzene. Similarly another class of catalysts tris(para-substituted) biarylamines (TPAs) was reportedly used to achieve C−H/N−H coupling of arenes and azoles[52]. When in their oxidized form, TPAs go from colorless to very colored so that they can absorb visible light and thus access extreme potential (~ + 4,0 to + 4,4 V vs SCE).

In the e-PRC field there has been a vast increase in the development of new catalysts and useful synthetic results. However, the mechanistic comprehension of many already tested systems remains object of debate and investigation[53–59].

1.1.3. Electrochemical recycling PRC

When considering recycling e-PRC what we do is shifting the area of operation of the electrochemical component: from having the formation of an active photocatalyst at the electrode we here go to a system in which the electrode regenerates the photocatalyst to close the cycle. In other words, in this type of system, electrochemical activation is not directly required to conduct the reaction; however, it is essential for the turnover of the catalyst. In recycling e-PRC the electrode works as the replacement of sacrificial oxidants or reductants in the photocatalyst turnover as shown in Scheme 4.

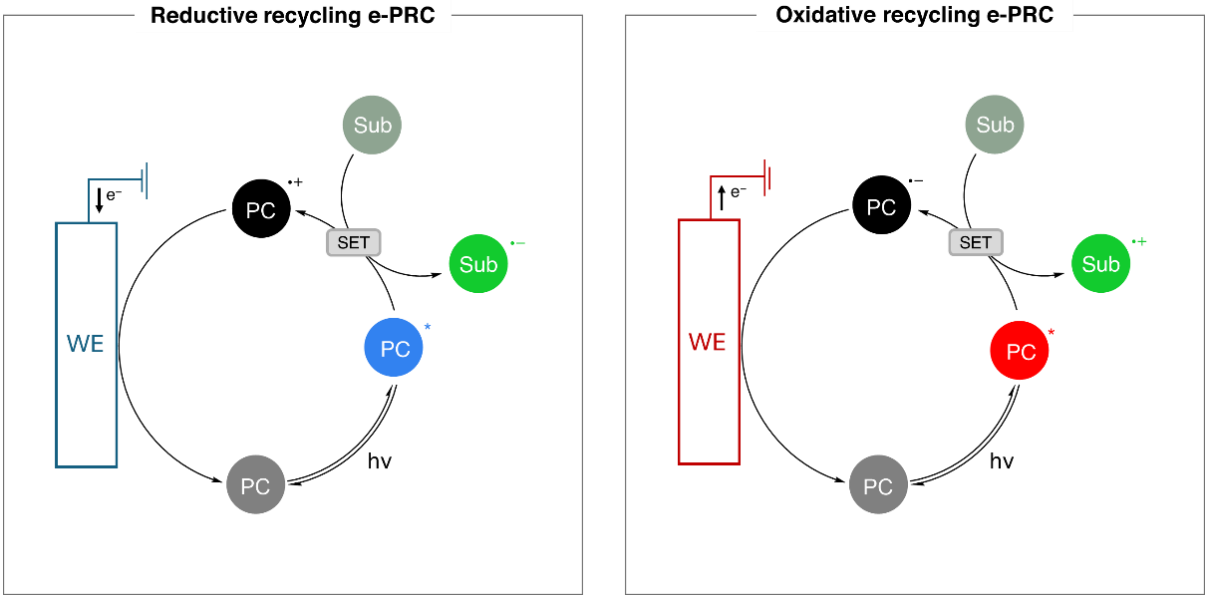

Scheme 4. Simplified schemes for recycling e-PRC reductive (left) and oxidative (right) mechanisms. WE indicate the working electrode at which the ground state PC is regenerated.

Xu et co-workers reported an application of recycling e-PRC in undivided cell using a Fukzumi's catalyst (a Mes-Acr$^+$, Figure 5) for a coupling of alkylfluoroborates with heteroarenes[60]. The group has further investigated the applications of recycling e-PRC to access C(sp^2)-C(sp^3) coupling using various types of catalysts such as Cerium catalyst and 4CzIPN[61]. Lambert group investigated recycling e-PRC as well, specifically addressing the S_NAr-type arene azolations[62] and arene acetoxylation[63] using in both reports DDQ as the catalyst (2,3-Dichloro-5,6-Dicyanobenzoquinone).

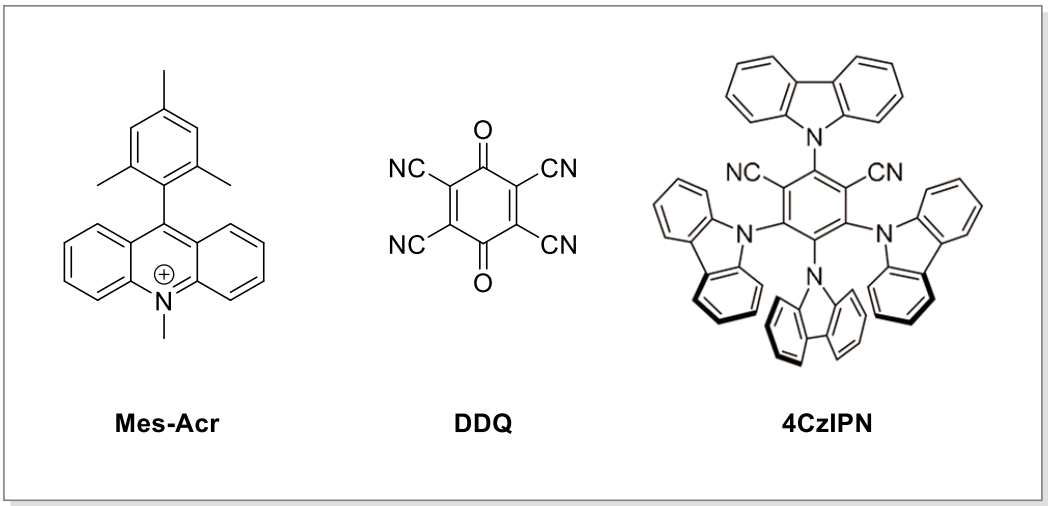

Figure 5. Catalysts used in recycling e-PRC

1.1.4. Perylene diimides

Perylene diimides (PDIs) are a class of fluorescent organic dyes are well known and have been used as pigments[64], colorants, and most prominently organic photovoltaics[65,66] because of their characteristic combination of thermal- and photostability and optical and redox properties[67,68].

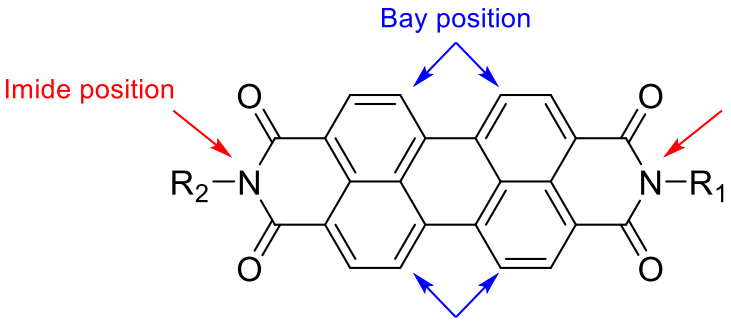

Figure 6. General strucutre of PDIs

Most of the research around applications of perylene diimides focuses on adequate substitution to improve electronic properties, directly or favoring aggregation.[66,69]

In the last decade PDIs have started to be implemented into photocatalytic processes addressing challenging reduction reactions. In the field of photoredox catalysis, PDIs have been used an studied as a reductant in two photon processes[34,70] and chemically mediated e-PRC[71,72].

1.2. Voltammetric study of e-PRC systems

The significant interest behind e-PRC within synthetic chemistry is due to its ability to drive thermodynamically challenging redox reactions by exploiting the highly oxidizing or reducing power of excited electrogenerated open-shell species, enabling to unprecedented reactivity.

Up to now, e-PRC systems has been very rarely studied by electrochemical techniques such as cyclic voltammetry (CV). Early work of Carsson and Hung[73] along with the research of Rusling[74] showed that electrochemical tools and more specifically CV have great potential in studying and understanding e-PRC systems. These early studies highlighted challenges such as thermal convection and back electron transfer but lacked quantitative analysis. To implement CV as an adequate tool of analysis for e-PRC systems a more systematic approach is required, as theoretically proposed by Costentin[75].

A summary of the steps necessary to the treatment of e-PRC systems with CV methods is presented in Section 2.3.1 and comprises the following steps:

1. *Diffusion and reduction*. A molecular photocatalyst (PC) diffuses in solution and is reduced at the electrode surface where the radical anion is generated ($PC^{\bullet-}$).
2. *Excitation.* Under steady irradiation the reduced species absorbs light and accesses an excited state ($*PC^{\bullet-}$). To selectively excite the radical anion and not interfere with the electrochemical process, the neutral species, PC, shouldn't absorb radiation in the same region as $PC^{\bullet-}$. The excitation kinetics can be evaluated knowing the irradiance of the photon flux (I) and the molar absorption coefficient ($k = \varepsilon I$).
3. *Excited state reactivity*. Once the excited state forms, $*PC^{\bullet-}$ can evolve through three possible pathways: nonradiative decay (with a rate constant $k_b = 1/\tau$, where τ is the $*PC^{\bullet-}$ lifetime), reaction with a substrate via single electron transfer (SET), and oxidation at the electrode, which regenerates PC through BET.

BET processes at the electrode can happen since $*PC^{\bullet-}$ is a strong reductant and has competitive drive to transfer an electron to the electrode within the potential range of the CV scan.

Back electron transfer can occur via a homogeneous irreversible reaction as well:

$$*PC^{\bullet-} + PC \rightarrow PC + PC^{\bullet-} \qquad (1.2.1)$$

Equation 1.2.1 describes a bimolecular reaction which generally has a negligible impact over the decay process of $*PC^{\bullet -}$[75]. BET can lead to energy wastage[73].

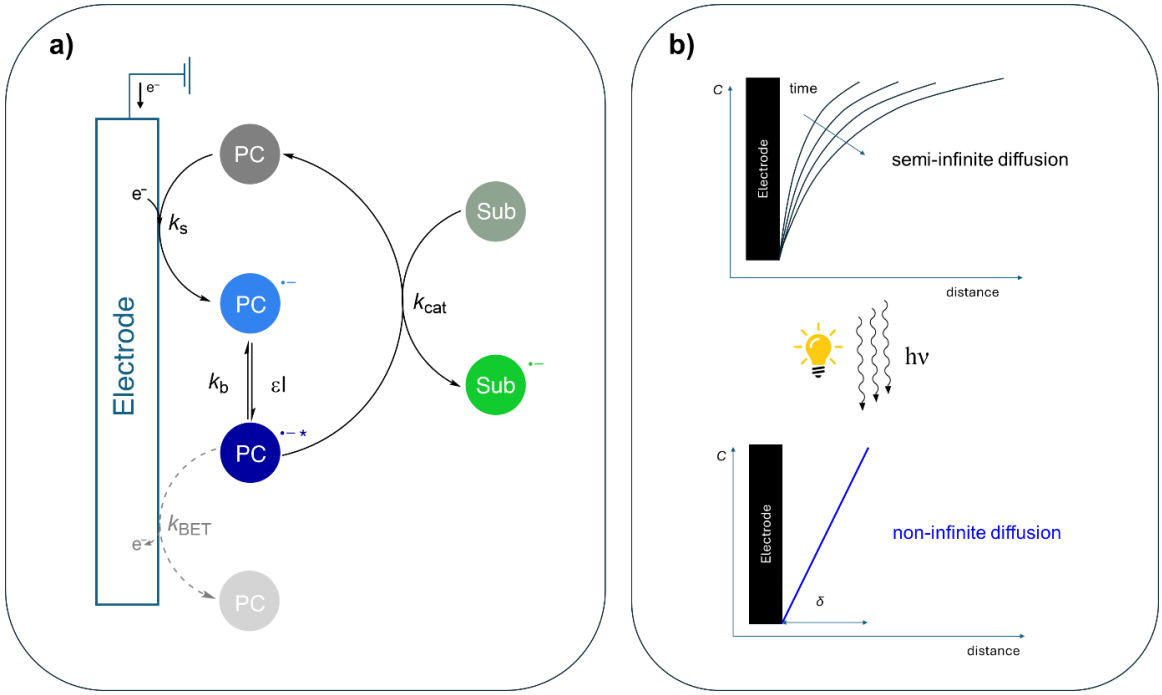

Figure 7. a) Scheme of the reaction mechanism a reductive e-PRC process. b) Variation of the diffusional regime at the electrode with irradiation

In summary, among the various issues present in the voltammetric studies of e-PRC processes what stand out is (i) the inherently heterogeneous nature of the process, involving electrogenerated ion radicals (e.g. $PC^{\bullet -}$) produced at the electrode surface and the coupled mass transfer; (ii) the oxidation of the photoexcited ion radicals ($*PC^{\bullet -}$) at the electrode, namely back electron transfer (BET); (iii) the nonradiative decay of the excited species ($*PC^{\bullet -}$) in the proximity of the electrode that may cause local heating and weak convection near the surface.

These factors necessitate a precise understanding of the interdependent mass transport, chemical reactions, and light absorption in such systems, which will be treated in detail in Chapter 3.

1.3. Reversible-deactivation radical polymerizations (RDRPs)

From the 1950s industry rapidly converged towards the mass production of polymers. Today the plastic industry reaches 400 million tons. Among the available techniques to produce polymers, radical polymerization (RP) is the most used in the industry[76].

Radical polymerization allows to access a wide range of monomers most of which are vinylic derivatives (Figure 8). Typically, vinylic monomers are classified into (i) More Active Monomers (MAMs),

which are readily polymerized thanks to the stability of the radical intermediates, and (ii) Less Active Monomers (LAMs), where the generated radicals are destabilized by electron donating species.

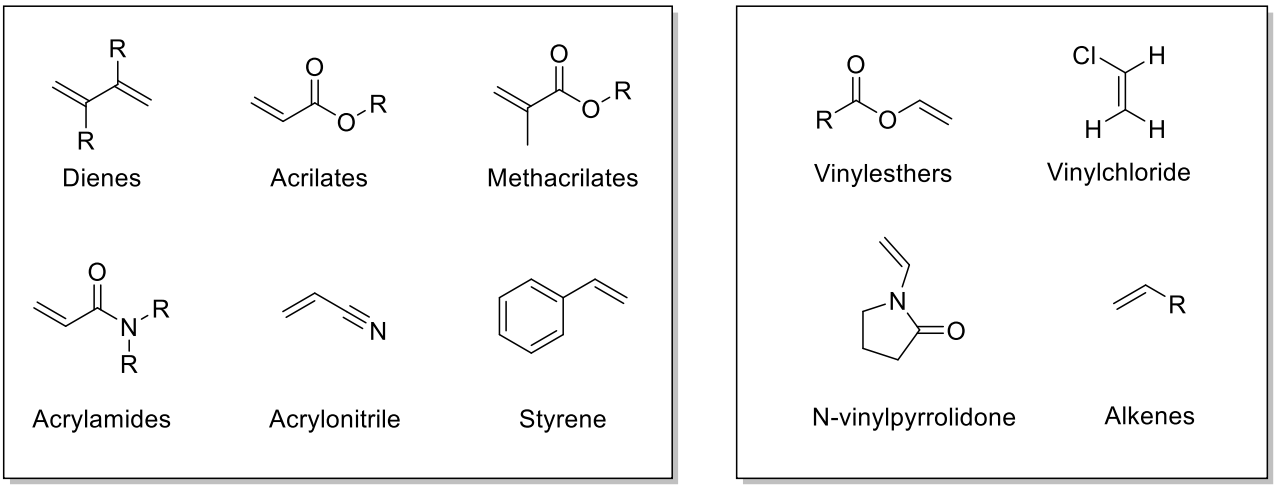

Figure 8. Structures of some representative MAMs (left) and LAMs (right)

In conventional free radical polymerization (FRP) the key steps include chain initiation, chain propagation, chain termination, and occasionally chain transfer. This classical chain reaction is typically treated kinetically assuming a stationary state with respect to the concentration of chain carriers (radicals). The lifetime of an individual radical is extremely short, equivalent to the period of chain growth for that radical, and the termination step involves the mutual annihilation of two chain carriers, resulting in polymers with a broad distribution of molecular weights (molar masses). Having a diffusion-limited termination causes the inactivity of most of the chains during the polymerization.

There are 4 key elementary steps in a FRP process:

i) Initiation: combination of the formation of radical species ($R^{\bullet}$) and its reaction with the monomer. The active radical is formed via homolytic cleavage of an initiator (I)

$$I \rightarrow 2R^{\bullet} \qquad v_d = 2fk_d[I] \qquad (1.3.1)$$

The homolytic rupture of the bond can be promoted by thermal, redox, photochemical or mechanical and ultrasonic activation of *I*. The factor *f* considers the initiation efficiency.

The initiating radical species then react with the monomer (*M*) there's the formation of a propagating macromolecule ($P^{\bullet}$).

$$R^{\bullet} + M \rightarrow P_1^{\bullet} \qquad v_i = k_i[R^{\bullet}][M] \qquad (1.3.2)$$

The initiation rate is much slower than the propagation rate (typically $k_d \approx 10^{-5}$ $M^{-1}s^{-1}$ and $k_i > 10^4$ $M^{-1}s^{-1}$) thus the kinetics of the process is limited by Eq 1.3.1.

Imposing the stationary state, we obtain the equation:

$$\frac{\mathrm{d}[\mathrm{R}^{\bullet}]}{\mathrm{dt}} = 2fk_{\mathrm{d}}[\mathrm{I}] - k_{\mathrm{i}}[\mathrm{R}^{\bullet}][\mathrm{M}] \quad (1.3.3)$$

The homolytic rupture of *I* can be promoted by thermal activation, redox reactions, photochemical processes, peroxide or diazene initiation, mechanical forces or sheer forces such as ultrasounds.

ii) Propagation: reaction between the propagating radical ($P_n^{\bullet}$) with a monomer unit. In this step there's the growth of the macromolecule which retains its radical nature and thus its capability to propagate. The rate of propagation depends on the stability of the radicals formed and the viscosity of the medium.

$$P_n^{\bullet} + M \rightarrow P_{n+1}^{\bullet} \qquad v_p = k_p[P_n^{\bullet}][M] \quad (1.3.4)$$

Propagation rate constants are typically in the range of 10^2-10^4 $M^{-1}s^{-1}$.

iii) Termination: series of reactions that involves the coupling (k_{tc}) and disproportion (k_{td}) of radical species. These reactions cause the loss of propagating macromolecules.

$$P_n^{\bullet} + P_m^{\bullet} \rightarrow P_nP_m \qquad v_{tc} = 2k_{tc}[P_n^{\bullet}][P_m^{\bullet}] \quad (1.3.5)$$

$$P_n^{\bullet} + P_m^{\bullet} \rightarrow P_n(-H) + P_m(+H) \qquad v_{td} = 2k_{td}[P_n^{\bullet}][P_m^{\bullet}] \quad (1.3.6)$$

iv) Chain transfer: transfer of the radical to another carbon, intermolecularly ($k_{tr,P}$), to the monomer ($k_{tr,M}$) or to specific molecules (Transfer Agents, *TA*) appositely introduced ($k_{tr,TA}$).

$$P_n^{\bullet} + M \rightarrow P_n + M^{\bullet} \qquad v_{tr,M} = k_{tr,M}[P^{\bullet}][M] \quad (1.3.7)$$

$$P_n^{\bullet} + P_x \rightarrow P_n + P_x^{\bullet} \qquad v_{tr,M} = k_{tr,P}[P_n^{\bullet}][P_x] \quad (1.3.6)$$

$$P_n^{\bullet} + TA \rightarrow P_n + TA^{\bullet} \qquad v_{tr,TA} = k_{tr,TA}[P_n^{\bullet}][TA] \quad (1.3.8)$$

Chain transfer does not result in a net consumption of propagating species, yet it influences the molecular weight and chain structure. The transfer of radicals between polymeric chains causes branching and cross-linking.

If the chain transfer is fast enough the kinetics will not be affected.

The occurrence of unavoidable and irreversible chain transfer and termination reactions results in broad chain length distributions, leading to "dead" chains that are inactive in further chain growth. This limitation restricts the properties of polymer materials and the controlled introduction of functional building blocks. These limitations confined polymers applications to commodities materials, rubbers and fibers until the end of the XIX century. To address these challenges and expand the field of applications for polymers, new polymerization techniques have been developed to reduce

irreversible termination, enabling more precise control over macromolecular composition, topology, and polymer chain length distributions.

A seminal example lies in the work of Michael Szwarc, in 1956, reporting the first example of 'living' anionic polymerization for polystirene[77,78]. Szwarc described a polymerization process completely devoid of chain breaking reactions and in which further addition of monomers allows the polymerization to continue, in turn leading to the formation of block copolymers.

Unlike anionic processes, radical chain growth is inevitably subject to radical-radical termination. Aiming to reduce the quantity of termination reactions and obtain 'living like' processes within the field of radical polymerizations, several techniques emerged around the 1990s. These methods use a dynamic equilibrium between an inert (dormant) state and an active state, where the radical species can propagate and grow. This reversible equilibrium extends the period of chain growth for individual propagating chains from mere seconds to the duration of the experiment. However, radical concentration is low so that most chains remain in the dormant state and thus unable to participate in chain propagation or termination. If the interconversion between active and dormant forms is rapid compared to propagation, all chains can grow at the same rate. If the initiating species are fully consumed before significant chain growth occurs, all chains grow at the same rate, resulting in a much narrower distribution of molar masses, approaching a Poisson distribution.

These radical polymerization reactions have garnered significant interest, but various authors have developed their own terminology, leading to a confusing array of terms. These include controlled radical polymerization (CRP), living radical polymerization (LRP), and controlled/living polymerization (CLRP). In the years the IUPAC deprecated the use of these terms and recommended the use of reversible-deactivation radical polymerizations (RDRPs) for polymerizations involving a dormant-propagating equilibrium[79]. In Table 1 there's a summary of IUPAC recommendations on the correct terminology for RDRPs which is useful to understand their differences compared to FRP.

Table 1. Updated IUPAC recommendations on terminology to be adopted for RDRPs. Adapted from [80].

Term	**Definition**	**Notes**	**Ref**
Controlled Polymerization	Term indicating control of a certain kinetic feature of a polymerization or structural aspect of the polymer molecules formed, or both.	1) "Controlled polymerization" refers to radical or ionic polymerization where reversible deactivation of chain carriers is key, interrupting propagation to control kinetic features or structural aspects of the resulting macromolecules. 2) "Controlled radical polymerization" is sometimes used to describe radical polymerization with reagents leading to low *Đ*, e.g. ATRP, NMP, or RAFT polymerization. 3) The term "controlled" should specify the particular kinetic or structural feature being controlled.	81,82

Living Polymerization	*Chain polymerization* in which *chain termination* and irreversible *chain transfer* are absent.	1) Often, the rate of chain initiation is faster than chain propagation, keeping the number of kinetic-chain carriers constant throughout the reaction, though this is not required for living polymerization. 2) In living polymerization, reversible (temporary) deactivation of active sites can occur. 3) In living polymerization, all formed macromolecules have the potential for further growth. 4) The terms "pseudo-living," "quasi-living," and "immortal" are discouraged.	[81,82]
Reversible-Deactivation Radical Polymerization	*Chain polymerization*, propagated by radicals that are deactivated reversibly, bringing them into active-dormant equilibria of which there might be more than one	1) The term "controlled radical polymerization" is acceptable if the nature of the control is specified at first mention. 2) Terms including "living" are discouraged since true living polymerization requires the absence of chain termination and irreversible chain transfer. Examples of discouraged terms are "living radical polymerization," "controlled/living polymerization," and "quasi-living polymerization." 3) ATRP, RAFT polymerization, and NMP fall into this category. 4) Rapid equilibrium compared to propagation allows control over chain-length distribution, creating low-dispersity polymers and block copolymers. Despite some termination, the equilibrium between propagating radicals and dormant species is maintained.	[82]

In summary, a RDRP process must satisfy some criteria to be considered such:

i) Limited termination events: active chains ($P_n^{\bullet}$) are much less present than chains (P_nX) (typically $[P_nX]/[P_n^{\bullet}] > 10^5$)[83]. This drastically reduces the probability of encounters between active radical species, thus reducing the frequency of termination events.

ii) Increase in the average chain lifetime: low radical concentration extends the chain's life.

iii) First order rate law with respect to monomer concentration: due to the fast initiation and the absence of termination, the factor $\ln\left(C_M^0/C_M^t\right)$ grows linear in time (C_M^0 and C_M^t indicates respectively the monomer concentration at time zero and at a generic time *t*)

$$\ln\left(\frac{C_M^0}{C_M^t}\right) = k_p[P_n^{\bullet}]t \qquad (1.3.9)$$

iv) Linear growth of Degree of Polymerization (DP) with conversion: since termination reactions are negligible, and initiation should be fast and quantitative, the number of growing equals the number of initiator molecules initially present.

Consequently, the DP varies linearly with monomer conversion. The degree of polymerization is defined as the ratio of the molecular weights of the polymer and the monomer:

$$\mathrm{DP} = \frac{\mathrm{MW_P}}{\mathrm{MW_M}} = \frac{C_M^0}{C_I^0} \cdot \frac{C_M^0 - C_M^t}{C_M^0} = \frac{C_M^0}{C_I^0} \cdot \mathrm{Conversion} \qquad (1.3.10)$$

v) Narrow distribution of molecular weight: fast initiation guarantees that all the chains start growing at the same time; the deactivation pathway allows all the radicals to have the same probability of encounter with the monomer (chain growth) before entering the dormant state. The distribution of molecular weights is measured through dispersity (*Đ*):

$$Đ = \frac{\bar{M}_w}{\bar{M}_n} \tag{1.3.11}$$

Where $\bar{M}_w$ is the weighted average and $\bar{M}_n$ is the number average of molecular weights. They're defined as:

$$\bar{M}_w = \frac{\sum_{i=1}^{\infty} n_i M_i^2}{\sum_{i=1}^{\infty} n_i M_i} \tag{1.3.12}$$

$$\bar{M}_n = \frac{\sum_{i=1}^{\infty} n_i M_i}{\sum_{i=1}^{\infty} n_i} \tag{1.3.13}$$

in which n_i is the number of propagating chains with a M_i molecular weight.

Typically, through FRP methods, dispersity values can reach the lower limit of $Đ = 1.5$, if the termination by combination only but in most systems $Đ > 2$[84]. Through RDRP processes many approaches have been developed to obtain low dispersity values ($Đ \rightarrow 1$). It is generally accepted that landmark after which is possible to consider a polymerization "controlled" is $Đ =$ 1,5. In RDRP processes it is common to observe a decrease in *Đ* values as the conversion increases.

vi) Chain end fidelity: the key distinction between a dormant chain and a terminated one is the presence of an activatable end. In an RDRP, termination events are significantly reduced, allowing for the reactivation of polymerization at any time by adding more monomer and activator. This feature allows precise control over the chemical structure of macromolecules (i.e. building blocks, stars, comb-shape copolymers etc).

Among the methods for reducing termination in radical polymerizations, atom-transfer radical polymerization (ATRP), first reported in 1995 by Matyjaszewski's group [85] and independently by Sawamoto's group[86], nitroxide-mediated polymerization (NMP) or aminoxyl-mediated polymerization (AMP), patented by CSIRO in 1986[87], and reversible addition-fragmentation chain-transfer (RAFT) polymerization, invented by Rizzardo and Moad in 1998[88,89], are the most common and versatile techniques.

RDRPs systems can be broadly classified into three distinct chemical mechanisms as in Figure 9. General mechanisms of reversible-deactivation radical polymerization. ($P_n^{\bullet}$ = propagating radical species; Pn -X = dormant capped polymer chains; M = monomer): i) stable radical-mediated polymerization, ii) atom transfer radical polymerization, and iii) degenerative transfer radical polymerization.

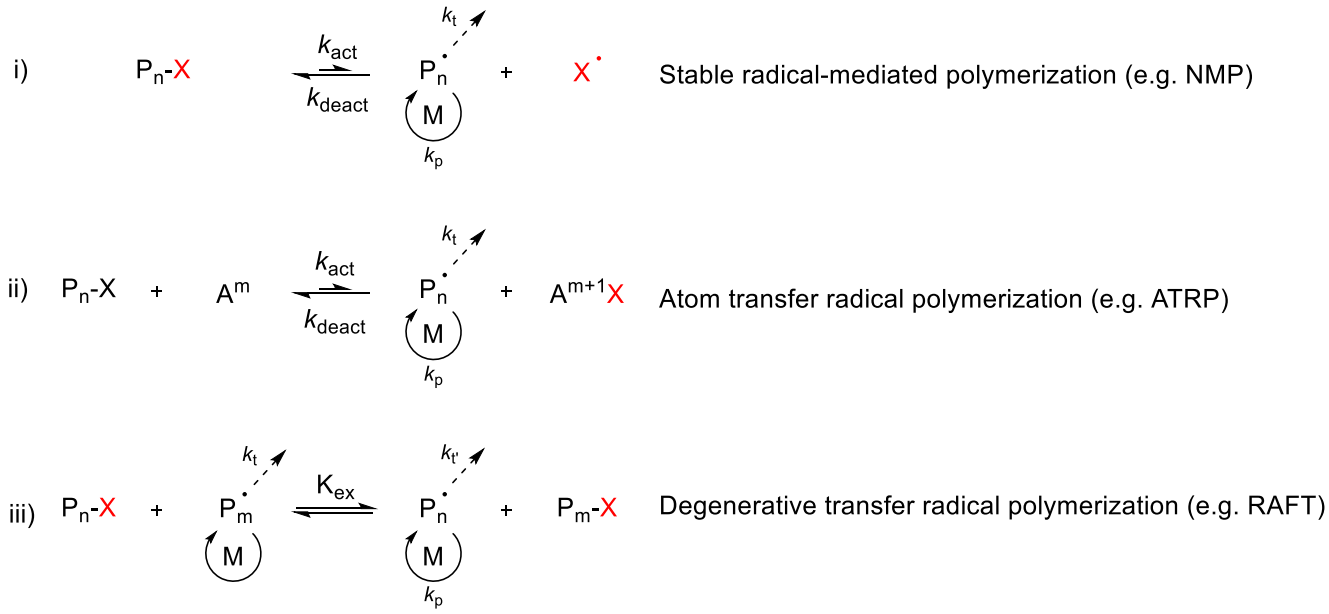

Figure 9. General mechanisms of reversible-deactivation radical polymerization. ($P_n^{\bullet}$ = propagating radical species; P_n -X = dormant capped polymer chains; M = monomer)

Mechanisms i) and ii) rely on the persistent radical effect (PRE). In these approaches, newly generated radicals are quickly trapped in a deactivation process (with a rate constant k_{deact}) by a radical captor X, typically a stable nitroxide radical (such as in NMP) or an organometallic species (such as in ATRP). The dormant species are activated (with a rate constant k_{act}) spontaneously, thermally, under light, or with an appropriate catalyst that regenerates the radical centers[90].

In PRE-regulated systems, while radicals can propagate or participate in bimolecular termination reactions, the trapping molecule X cannot terminate the reaction but can only reversibly couple with the growing polymer chain. Each polymer termination event (with rate constant k_t) is accompanied by an accumulation of dead chains, whose concentration irreversibly increases over time. This leads to a reduced concentration of radicals due to the equilibrium between dormant and active species shifting towards the dormant form. Consequently, there is a lower probability of termination and an establishment of self-regulation of the radical concentration in the solution, which is the essence of the PRE.

In degenerative transfer processes (DT) mechanisms a species X-P_m promotes chain transfer between two radicals via a bimolecular reaction. Chain transfer agents (CTAs) are typically unsaturated

compounds with a C=S bond, which is reactive towards radical addition. Systems based on degenerative exchange processes follow the typical kinetics of radical polymerization, with slow initiation and fast termination; the PRE is not observed. Steady state is achieved through the equilibrium between initiation and termination.

In DT-mediated polymerizations, a faster DT process results in a narrower molecular weight distribution. When the reversible chain-transfer agent is used in large excess over the initiator, the molecular weight is primarily determined by the feed ratio of monomer to the chain-transfer agent. Among the various methods for RDRP, DT-mediated radical polymerization is the simplest, as molecular weight can be controlled by adding an appropriate reversible chain-transfer agent into a conventional radical polymerization. The most used DT-mediated polymerization is the reversible addition–fragmentation chain transfer (RAFT) process, which is described in the next section.

1.3.1. Reversible Addition-Fragmentation Chain Transfer Polymerization (RAFT)

Since its first report in 1998[88], the RAFT process has developed into one of the most versatile and powerful DT polymerization techniques for synthesizing complex polymeric architectures. Over the past 20 years, interest in RAFT polymerization has grown rapidly. Initially, research focused on understanding the mechanism, followed by demonstrating the variety of polymeric architectures and functional materials achievable through this method, and more recently, on application-driven studies. Being a DT-mediated system, there is no variation in the total amount of radicals during the activation-deactivation equilibrium, so there's the necessity for a source of radicals. In traditional RAFT processes a thermal initiator is used as radical source.

In RAFT polymerization a dynamic equilibrium is established using a CTA, also called RAFT agent. The CTAs mediating RAFT processes are characterized by three functional groups: X, A, and Z (Figure 10). The first two groups, X and A (typically both S atoms), can form a double bond with carbon that is reactive towards radical addition. Substituent Z is chosen to modulate reactivity towards propagating radicals and to provide stability to the intermediate. The R group has a labile bond in the intermediate radical, allowing for easy homolytic dissociation and reinitiation of polymerization.

Generally, $R^{\bullet}$ is more stable than $P_n^{\bullet}$. In particular, the reinitiation rate via $R^{\bullet}$ must be greater than its propagation rate.

Most representative CTAs are thiocarbonyl compounds such as dithiobenzoates, trithiocarbonates, dithiocarbamates, and xanthates (Figure 10).

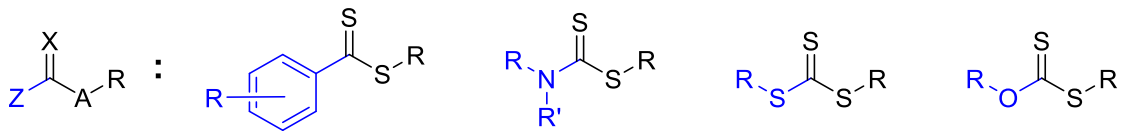

Figure 10. Common CTAs. Left to right: generic CTA's structure, dithiobenzoates, dithiocarbamates, trithiocarbonates, xanthates.

The conventional RAFT mechanism in its entirety is presented in Scheme 5.

Firstly, an external initiator is fragmented, typically by heat or light, to generate initiating radicals ($I^{\bullet}$). After several additions of monomers, the propagating radical adds to the thiocabonylthio (TCT) CTA. The resulting TCT radical intermediate then fragments, releasing the R group as another propagating radical ($R^{\bullet}$). These propagating radicals undergo reversible addition and fragmentation, cycling between dormant and active species in the RAFT main equilibrium. Through this equilibrium, all propagating radicals have equal probabilities for chain growth. Addition and fragmentation occur faster than propagation, preventing bimolecular termination between radicals. Consequently, polymers with TCT end groups exhibit low dispersity and can be reactivated by adding new monomers. Achieving controlled and living radical polymerization through an efficient RAFT process requires selecting a CTA with appropriate R and Z groups for each monomer family, ensuring energetically favorable addition, fragmentation, and propagation.

i) Initiation and Propagation

ii) RAFT pre-equilibrium

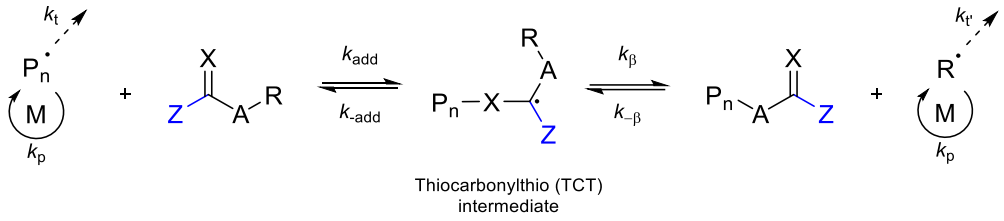

iii) Reinitiation and propagation

iv) RAFT pre-equilibrium

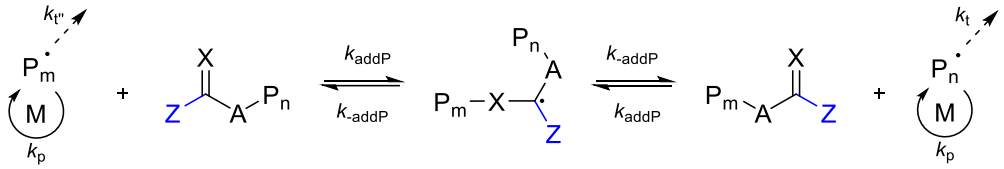

v) Termination

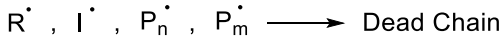

Scheme 5. Conventional RAFT mechanism. Generic termination reactions listed in point v.

In an effective process, the rate of the addition/fragmentation equilibrium is higher than that of propagation, so less than one monomer unit should be added per activation cycle to obtain polymer chains with a similar degree of polymerization[91].

In a RAFT polymerization, at least four equilibrium constants must be taken into consideration:

$$K = \frac{k_{add}}{k_{-add}} \qquad \text{Related to pre-equilibrium} \qquad (1.4.1)$$

$$K_{\beta} = \frac{k_{-\beta}}{k_{\beta}} \qquad \text{Related to pre-equilibrium} \qquad (1.4.2)$$

$$K_{p} = \frac{k_{addP}}{k_{-addP}} \qquad \text{Related to main equilibrium} \qquad (1.4.3)$$

In addition to the mentioned ones there is a degenerate reaction (Scheme 6) that is usually ignored on the presumption that the lifetime of the TCT intermediate is negligible. If fragmentation is slow or if there are side reactions which involve the intermediate, this reaction should not be neglected[92].

vi) Reversible chain transfer

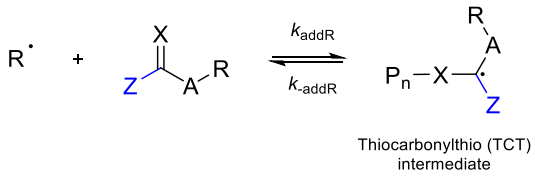

Scheme 6. Reversible chain transfer degenerate reaction

Consumption of the CTA depends on two transfer coefficients:

$$C_{tr} = \frac{k_{tr}}{k_p} \tag{1.4.4}$$

$$C_{-tr} = \frac{k_{-tr}}{k_i} \tag{1.4.5}$$

Equation 1.4.4 describe the reactivity of the propagating radical ($P_n^{\bullet}$) whereas equation 1.4.5 is related to the reactivity of the expelled radical ($R^{\bullet}$).

The rate constant for chain transfer (k_{tr}) can be defined as:

$$k_{tr} = k_{add}\frac{k_\beta}{k_{-add} + k_\beta} = k_{add}\phi \tag{1.4.6}$$

where ϕ is the partition coefficient, which indicates how the adduct is distributed between reactants and products.

And similarly, k_{-tr} is

$$k_{-tr} = k_{-\beta}\frac{k_{-add}}{k_\beta + k_{-add}} = k_{-\beta}(1-\phi) \tag{1.4.7}$$

If the expelled radical is a long, propagating chain $k_{tr} = k_{-tr}$, $k_{-add} = k_{\beta}$ and thus $C_{tr}=C_{-tr}$ and $\phi = 0,5$. Under such conditions the chains will grow at the same rate.

While in the initiation phase the partition coefficient indicates the tendency of intermediate radicals to fragmentate into products or back into reactants.

To have an efficient RAFT polymerization the R group should be a good homolytic leaving group with respect to the propagating radical ($\phi > 0,5$).[92]

Similarly to other RDRPs, in a RAFT process it is possible to estimate the theoretical average molecular weight of the polymer:

$$M_{n,th} = \frac{C_M^0 - C_M^t}{C_{CTA}^0} \cdot MW_M + MW_{CTA} \quad (1.4.8)$$

where C_{CTA}^0 and C_M^0 indicates the initial concentration of CTA and monomer, respectively, while C_M^t is the concentration of monomer at a time *t*. The terms MW_M and MW_{CTA} are the molar weight of monomer and RAFT agent. Equation 4.7 can be simplified in:

$$M_{n,th} = \text{Conversion} \cdot MW_M \cdot DP_0 + MW_{CTA} \quad (1.4.9)$$

$$DP_0 = \frac{C_M^0}{C_{CTA}^0} \quad (1.4.10)$$

DP_0 indicates the theoretical degree of polymerization.

The agreement of experimental MW values with equations 1.4.8 or 1.4.9 indicates controlled polymerization. Positive deviations suggest incomplete consumption of the RAFT agent, while negative deviations imply the presence of unintended polymeric chains.

To evaluate the efficiency of a RAFT polymerization, several parameters must be analyzed, including the characteristics of the final polymeric product (molecular weight, dispersity) and the total final polymerization time. Knowing the efficiency of a particular CTA through transfer coefficients and calculating the theoretical molecular weight are useful tools for modulating the process and studying its correct functioning.

1.3.2. RAFT polymerization initiation

In RAFT polymerizations the source of initiating radicals can be any method of generating free radicals since the control over the chain's growth is given by the DT involving the CTA.

RAFT polymerization can be activated with a wide selection of methods, which affect several aspects of the process[91]: (i) polymerization rate – more radicals generated means faster polymerization; (ii) control over the polymerization – more radicals causes more termination; (iii) reaction conditions.

1.3.2.1. Thermal Initiation

The most conventional method for RAFT polymerizations involves using an external radical initiator, typically thermal initiators like AIBN (Figure 11), benzoyl peroxide, and potassium peroxydisulfate[88].

Thermal self-initiation is feasible for styrene and styrene/acrylonitrile mixtures. Temperature regulation is crucial to control the formation of active radicals and, consequently, the growing polymer chains. Excessive initiation can lead to uncontrolled polymer growth and a decrease in dispersity (*Đ*). For instance AIBN decomposition rate constant, k_d, increases from $9{,}15 \cdot 10^{-6}\ s^{-1}$ to $1{,}52 \cdot 10^{-3}\ s^{-1}$ when going from 60 °C to 100 °C.[93]

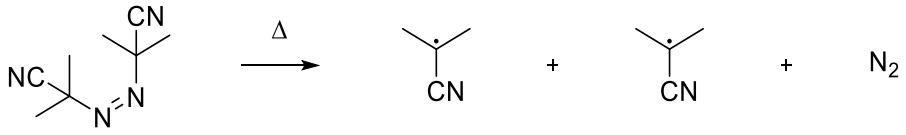

Figure 11. Decomposition of 2,2-azobisisobutyronitrile (AIBN)

1.3.2.2. Redox Activation

Using conventional thermal initiators results in the continuous generation of new chains throughout polymerization. This can lead to polymers with higher dispersity and lower functionality, making it difficult to prepare pure block copolymers. Moreover, heat is the main energy source for polymerization via thermal initiation.

Over the years, novel initiation systems have been developed to minimize the formation of new chains, while working at or around room temperature[88,91,94].

These systems utilize either (i) external molecules and/or stimuli to generate radicals at ambient temperature or (ii) direct activation of the RAFT agent to initiate polymerization.

A method to circumvent the thermal initiation is the employment of redox pairs, able to initiate a RAFT polymerization at room temperature.

Pan and co-workers reported room temperature RAFT polymerization of methyl acrylate (MA), methyl methacrylate (MMA), and styrene (STY) using a redox initiation system consisting of benzoyl peroxide (BPO) and N,N′-dimethylaniline (DMAN).[95]

More recently Qiao and co-workers proposed a RAFT process promoted by a Fenton reaction, in which the redox cycle is completed by Fe^{2+} and H_2O_2.[96] Various works based on Fenton-RAFT processes have been developed.[97,98]

1.3.2.3. Electrochemical Activation

Another explored approach to initiate RAFT process is the use of electrochemical methods.

Electrochemistry offers tunable parameters for creating well-defined polymers under mild, controlled conditions. Electrochemically-triggered RDRPs also benefit from in-situ monitoring and direct control over the stimulus in addition to a 'green' character shared by all the organic synthesis promoted by electricity.[25]

On the wave of successful and comprehensive work on electrochemically activated ATRP (*e*ATRP)[99–101], research on the application of electrochemical methods on RAFT processes have been conducted over the years[102–104].

In electrochemically mediated reversible addition–fragmentation chain-transfer (*e*RAFT) polymerization, the electrochemical stimuli can reduce the RAFT agent directly or with a mediator.

i) Direct *e*RAFT

Here the RAFT agent is directly reduced on the electrode surface (Scheme 7).

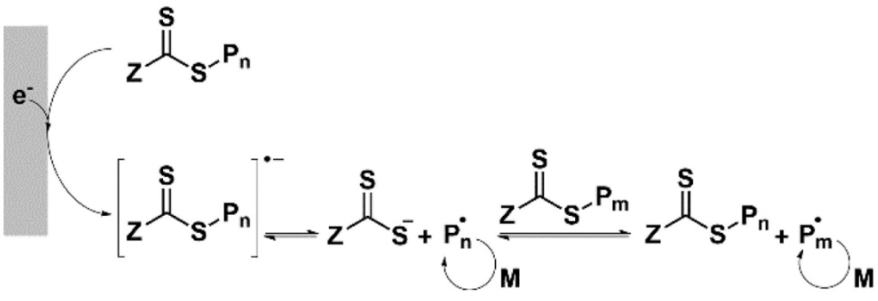

Scheme 7. Mechanism of direct eRAFT with reduction of the CTA at the electrode. Adapted from [103].

The seminal work by Lorandi et al[103] showed that the direct reduction of CTAs to their corresponding radical anions triggers a series of chemical reactions, including "father–son" reactions between the electrogenerated species and the starting CTA. It showed that the presence of more electron-withdrawing groups (EWGs) and a higher radical-stabilizing power of the R group lead to a more positive

cathodic peak potential (E_{pc}). The E_{pc} of CTAs follows the order: dithiobenzoates > trithiocarbonates > dithiocarbamates ≈ xanthate (Figure 12). Electroreduction of various CTAs, however, gave low monomer conversion and broad molecular weight distributions for *e*RAFT of styrene. The lack of control over the polymerization was attributed to the consumption of the RAFT agent, confirmed by CV analysis after several hours of electrolysis.

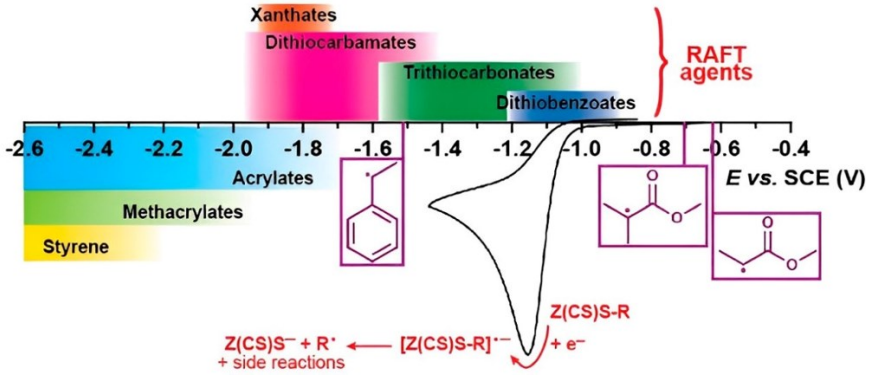

Figure 12. Indicative scale of the Reduction Potentials of CTAs and Monomers paired with a representative CV of a CTA. In purple boxes the potentials of the monomers' propagating radicals

ii) Mediated *e*RAFT

Here the reduction of the CTA is carried out by a mediator species that is regenerated at the electrode (Scheme 8).

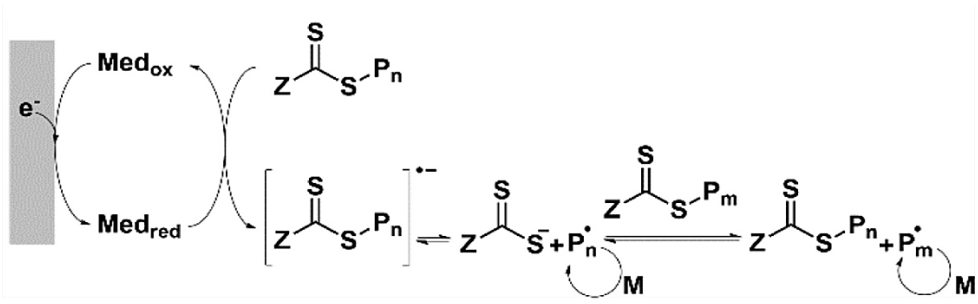

Scheme 8. Mechanism of mediated eRAFT with reduction of the CTA by the electrogenerated mediator. Adapted from 95.

The necessary condition is that the reduction potential of is more positive than the potential of every other species in solution during the polymerization.

Results with mediated *e*RAFT have been much more promising when compared with direct *e*RAFT.

Wang et al. reported[102] that controlled polymerizations at room temperature of methyl methacrylate (MMA), *n*-butyl acrylate (BA), and *tert*-butyl acrylate (*t*BA) were triggered using mediators such as benzoyl peroxide (BPO), or a diazonium salt, 4-bromobenzenediazonium tetrafluoroborate

($BrPhN_2^+$). An increase in control at the cost of reaction rate was observed with the application of more positive potential. Lorandi *et al*[103] tested the efficiency of tetraphenylporphyrin (TPP), 3-nitrobenzonitrile (3-NBN) and 2-nitro-*m*-xylene (2-NX) styrene. They obtained low *Đ* polymers with TPP in the polymerization of BA and MA but encountered CTAs degradation with (3-NBN) and 2-nitro-*m*-xylene (2-NX), probably due to side reactions between mediators and substrates.

More recently Moad and co-workers proved an effective mediated *e*RAFT polymerization using anthraquinone (AQ)[104]. The group successfully polymerized MMA obtaining low dispersity products and confirming the livingness of the reaction by performing chain extension experiments.

To this day, mediated *e*RAFT seems the only pursuable approach to implementing electrochemical techniques into RAFT processes.

1.3.2.4. Photoinduced Activation

Over the years many attempts have been made to introduce light as the triggering energy source, appealed by the potential benefits of light-driven reaction, given its ubiquity, low cost and potential selectivity.[105,106]

In the last two decades many photo-induced RDRPs were developed, both with organo-metallic catalysts[107–109] and organic photocatalysts[110–113] in what are called metal-free photo-RDRPs.

There are several light-driven mechanisms that can trigger RAFT polymerizations:

i) **Photomediated RAFT polymerization**: light (typically UV light) is used to cause the homolytic bond cleavage of initiators, similarly to what happen in photo-induced FRPs, which then proceed to establish the RAFT equilibrium and continuate the polymerization in a controlled fashion[91]. Nevertheless, the high energy of UV light required to cleave the initiator's bonds can cause photodegradation and a decrease in dispersity.[114]

ii) **Photoiniferter RAFT polymerization**: In this method, a TCT-based RAFT agent serves as an initiator, transfer agent, and reversible terminator (ini-fer-ter), eliminating the need for an external initiator. The CTA absorbs light to reach an excited state, leading to homolysis of the C–S bond and generating an active propagating radical and a persistent TCT radical. The propagating radicals engage in degenerative chain transfer entering the RAFT equilibrium, while the TCT radical can reversibly deactivate active radical species (Scheme 9). This technique was first introduced by Otsu and co-workers[115,116] who introduced it as a type of RDRP and coined the term photoiniferter. This method has recently gained renewed attention and

interest through the works of Qiao[117] and Boyer[118] that introduced visible light as energy source.

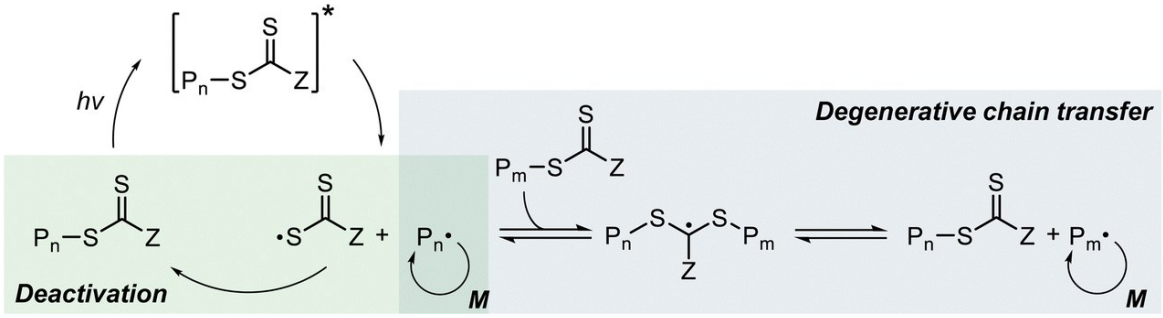

Scheme 9. Reaction scheme for a photoiniferter mechanism. Adapted from [119].

iii) **Photoinduced electron/energy transfer-RAFT (PET-RAFT)**: The main difference between classic photo-mediated RAFT processes (i and ii above) and PET-RAFT polymerization stands in the fact that the latter employs photocatalysts (PCs) to promote the initiation. This enables the use of visible light to activate PCs and subsequentially trigger the RAFT process. PET-RAFT, pioneered by Boyer and co-workers in 2014,[120] and since became the standard photo-mediated RAFT process.[121,122] It is notable for its simplicity and tolerance to various functional groups[123]. Typically, used PCs are transition metal catalysts or an organic dye. Despite its popularity, there is ongoing debate about the exact mechanistic details, particularly whether initiation occurs through electron or energy transfer. Various potential pathways are illustrated in Scheme 10[124].

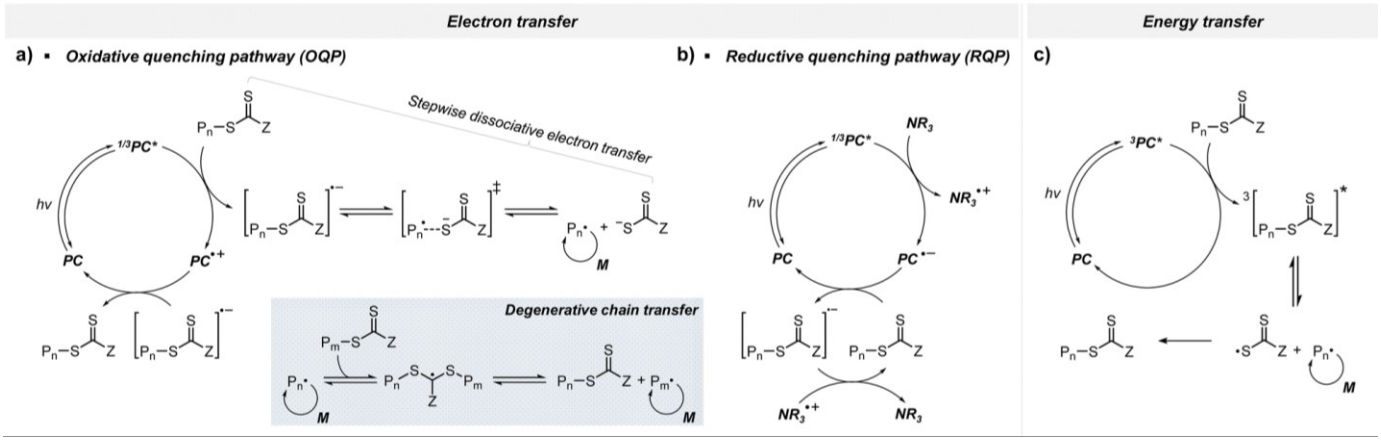

Scheme 10. Mechanism of PET-RAFT polymerization. Electron transfer via (a) oxidative quenching pathway (OQP) and (b) reductive quenching pathway (RQP) in the presence of a reducing agent (e.g., tertiary amine). (c) Energy transfer. Adapted from [119].

In PET-RAFT polymerizations the mechanism can follow an oxidative quenching pathway (OQP) or a reductive quenching pathway (RQP).

The OQP in PET-RAFT polymerization involves the oxidation of an excited-state photocatalyst (PC*). Electron transfer from the excited-state PC to a ground-state chain transfer agent (CTA) creates a one-electron-oxidized PC ($PC^{\cdot+}$) and an anionic intermediate of the CTA. This intermediate undergoes fragmentation, producing a propagating radical and a TCT anion, likely via a stepwise dissociative electron transfer (DET) mechanism[125].

In photoinduced Energy Transfer-RAFT polymerization the excited state PC* transfer energy to the CTA. The CTA is promoted to an excited state from which occurs homolytic C–S cleavage. The transfer is most likely to take place from the triplet state T_1 of the catalyst to the triplet state of the CTA. The most prominent and relevant process in a PET-RAFT polymerization is the Dexter energy transfer.[126] Energy transfer requires overlap between the emission spectrum of the donor and absorption spectrum of the acceptor, otherwise a DET is more likely.

1.4. Dissociative Electron Transfer (DET)

In this work, we have conducted a detailed analysis of DET reactions catalyzed by excited-state photocatalysts. One promising application of DETs, both theoretically and practically, is the cleavage of carbon–halogen (C–X) bonds in alkyl halides. Specifically, the focus on alkyl halides stems from the interest in breaking the C–X σ-bond after the injection of a single electron, whether achieved chemically or electrochemically. Furthermore, DET reactions are advantageous because they offer a clean method for generating reactive species such as radicals. Depending on whether the process is reductive or oxidative, they can also produce bases or acids, as well as nucleophiles or electrophiles.

The DET reactions investigated in this thesis followed outer-sphere electron transfer (OSET) mechanisms, which can be modeled using Marcus-Hush theory and its subsequent modifications by Savéant. In more detail, DET can occur via two main mechanisms (Figure 13a) characterized by different reaction energy profiles (Figure 13b): stepwise DET (SDET) and concerted DET (CDET). In SDET, an anion radical intermediate $RX^{\bullet-}$ forms first, followed by cleavage of the C−X bond. This mechanism is common in *aryl halides* due to resonance stabilization of the radical anion. In CDET, bond dissociation occurs simultaneously with electron transfer, typical of *alkyl halides* where electron delocalization is not possible. For CDET processes, Savéant proposed an additional variation termed the sticky model, where after cleavage of the C−X bond, the $R^{\bullet}$ and X^{-} fragments interact via ion-dipole interaction in the solvent cage, reducing the activation energy (

Figure 13c). Note that this "sticky" interaction has no effect and does not apply to the barrier of SDET processes.

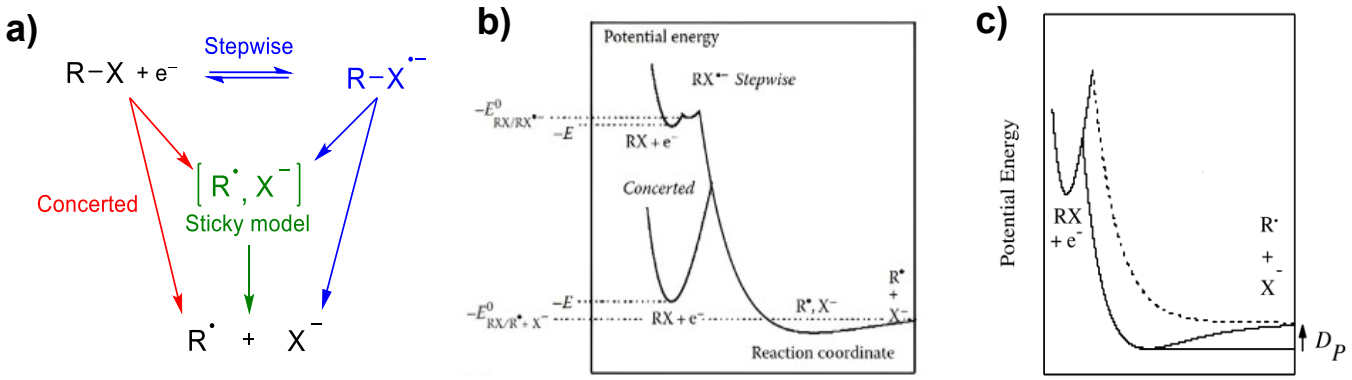

Figure 13. a) Mechanisms for reductive DET processes. b) Energy profiles for the reductive cleavage of RX bonds. c) Elucidation of the difference in the energy profile for CDET and sticky DET. Adapted with permission from Mazzucato et al.[127]

The DET model is based on a Morse curve approximation for the description of the bond cleavage coupled with a Marcus-Hush estimation of the solvent reorganization. The activation energy $\Delta G^{\ddagger}$ for a reaction between a catalyst and an alkyl halide

$$\mathrm{Cat_{Red}} + \mathrm{RX} \xrightarrow{k_{DET}} \mathrm{Cat_{Ox}} + \mathrm{R^{\bullet}} + \mathrm{X^{-}}$$

can be formally described with the Marcus model[128]:

$$\Delta G^{\ddagger} = \Delta G_0^{\ddagger}\left(1 + \frac{\Delta G^0}{4\Delta G_0^{\ddagger}}\right)^2 \qquad (1.5.1)$$

$$\Delta G_0^{\ddagger} = \frac{\lambda_i + \lambda_o}{4} \qquad (1.5.2)$$

where ΔG^0 is the reaction Gibbs free energy, $\Delta G_0^{\ddagger}$ is the intrinsic barrier of the process (activation free energy at $\Delta G^0 = 0$) , λ_o is the Marcus-Hush solvent reorganization free energy[129,130], and λ_i is the inner reorganization energy[131]. Both equations 1.5.1 and 1.5.2 coherently apply to homogeneous DET processes.

The reaction rate constant for the process is described by the Arrhenius equation:

$$k_{\mathrm{DET}} = Ze^{-\frac{\Delta G^{\ddagger}}{RT}} \qquad (1.5.3)$$

where Z is the nuclear frequency factor.

For a SDET process, λ_i is very small because after electron transfer the electron is highly delocalized in the aromatic ring of aryl halides.[131] On the contrary the CDET is kinetically disfavored by a significant activation barrier resulting from bond cleavage, thus having to pay the "cost" of bond dissociation energy ($\lambda_i \cong D_{RX}$).

In the case of the sticky CDET pathway, the activation barrier is better described by equation 1.5.3 and 1.5.4.[127]

$$\Delta G^{\ddagger} = \Delta G_0^{\ddagger}\left(1 + \frac{\Delta G^0 - D_p}{4\Delta G_0^{\ddagger}}\right)^2 \tag{1.5.4}$$

$$\Delta G_0^{\ddagger} = \frac{\left(\sqrt{D_{RX}} - \sqrt{D_p}\right)^2 + \lambda_o}{4} \tag{1.5.5}$$

in which the term D_p accounts for the energy of the charge-dipole interaction between $R^{\bullet}$ and X^- (see Figure 13c).

1.5. Aim of the Thesis

The aim of this thesis is to investigate the photo-electrochemical control of an RDRP "controlled" polymerization using an e-PRC system, with a specific focus on the catalyst *N*,*N*'-Bis(2,6-diisopropylphenyl)-3,4,9,10-perylenetetracarboxylic Diimide (PDI). PDI is a commercially available organic dye that exhibits poor redox and photoredox properties in its ground state. However, its reduced forms ($PDI^{\bullet-}$ and PDI^{2-}) exhibit significantly enhanced reduction potentials upon photoexcitation, potentially making them effective initiators for polymerizations.

Key objectives include:

(i) **Examining PDI's Capability as electrophotocatalyst**: Chapter 3.1 investigates PDI's ability to generate radicals under mild conditions via e-PRC reduction, focusing on its interactions with alkyl halides (RX) as polymerization initiators under light irradiation. A novel technique involving cyclic voltammetry (CV) under light irradiation was developed to evaluate PDI's electrophotocatalytic performance. This provided insights into the kinetics and mechanisms of the e-PRC process, enabling to measure the kinetics of excited state quenching for the reaction between

*$PDI^{\bullet-}$ and several RX substrates. Under the same framework, the excited state dianion *PDI^{2-} was quantitatively investigated as well.

(ii) **Quantitative Assessment of the novel voltammetric technique**: In Chapter 3.2, the developed CV technique was benchmarked against established transition absorption techniques, to prove its validity to investigate the dynamics of excited state quenching. CV emerged as a rapid technique to probe ultrafast reactions from excited states.

(iii)**Applying e-PRC to RDRP Polymerization**: In Chapter 3.3, after evaluating PDI's ability to generate radicals under e-PRC conditions, the PDI catalyst is applied to RDRP polymerizations, including ATRP and RAFT. The RAFT polymerization method was the most successful, enabling us to establish a novel polymerization pathway termed PET-*e*RAFT, which combines light and electrochemical potential for precise control of polymerization. The PET-*e*RAFT process operated under mild electrochemical potentials (down to –0,43 V vs SCE) and low-energy light (630 nm), providing dual control through electricity and light.

2. Experimental Section

Here are reported the chemicals and the instruments used in this work. Brief elucidations on specific techniques are reported as well.

2.1. Chemicals

Solvents

N,*N*-Dimethylformamide (DMF, Carlo Erba, HPLC isocratic grade 99,9%). Dimethyl sulfoxide (DMSO, Sigma-Aldrich, ≥ 99,9%). Chloroform-d ($CDCl_3$, Sigma-Aldrich, 99,8% atom % D).

All the solvents were used as received.

Photocatalyst

N,*N*'-Bis(2,6-diisopropylphenyl)-3,4,9,10-perylenetetracarboxylic diimide (PDI, TCI America, > 98,0%).

Supporting Electrolytes

Tetrabutylammonium tetrafluoroborate (*n*-Bu_4NBF_4, Sigma-Aldrich, > 99%), recrystallized in ethanol and dried under vacuum at 70 °C for 48 h. Tetrabutylammonium iodide (*n*-Bu_4NI, Sigma-Aldrich, >99%).

Substrates

Methyl 2-bromopropionate (MBP, Sigma-Aldrich, 98%). Ethyl 2-bromopropionate (EBP, Sigma-Aldrich, 98%). Methyl α-bromoisobutyrate (MBiB, Sigma-Aldrich, ≥ 99.0%). Ethyl α-bromoisobutyrate (EBiB, Sigma-Aldrich, 98%). Bromoacetonitrile (BrACN, Sigma-Aldrich, 97%), Methyl 4-chlorobenzoate (MCB, Sigma-Aldrich, 99%).

Monomers

Methyl methacrylate (MMA, Sigma-Aldrich, 99%).

Chain Transfer Agent

4-cyano-4-[(dodecylsulfanylthiocarbonyl)sulfanyl]pentanoic acid (CDTPA, Boron Molecular, 97%).

Other chemicals

Methanol (MeOH, Sigma-Aldrich, ACS reagent, ≥ 99.8%), used to precipitate obtained polymers.

Ferrocene (Fc, Acros Organics, 98%), used as internal reference in all CV experiments.

2.2. Instrumentation

2.2.1. Electrodes

Working Electrode (WE): Three WEs were used depending on the specific procedure.

(i) Rotating disk electrode (RDE) with a glassy carbon tip (GC, diameter 0,075 mm, homemade). The RDE is connected to an engine which controls the stirring. Apart from the GC tip all the equipment was bought from Metrohm AG.
(ii) Small GC electrode (homemade)
(iii) Platinum gauze (homemade).

Before each electrochemical measurement, the GC electrode surface is polished with a 0,25 µm diamond paste and rinsed in absolute ethanol while sonicating for 10 minutes. Before inserting the electrode in the cell, it is carefully washed with acetone.

Platinum electrode cleaning requires electrochemical activation. The Pt gauze is burned using a blow torch and then activated via CV scans between – 0,67 V and 0,91 V vs $Hg/HgSO_4$ in a 0,5 M H_2SO_4 solution.

Reference Electrode (RE): Silver (Ag) wire, covered in AgI and immersed in a solution of tetrabutylammonium iodide (*n*-Bu_4NI) 0,1 M in DMF. AgI is electrodeposited in galvanostatic mode (0,4 mA/cm^2, KI 0,1 M + HNO_3 0,1 M). The electrode was made in the laboratory using a glass tube with a porous frit (G3) partially filled with Agar gel, to keep RE and solution separate. RE is not stable in organic solvents and its potential can vary over time. The ferrocene|ferrocenium ($Fc|Fc^+$) couple is used as internal reference. At the end of each electrochemical experiment, a small amount of Fc is added to the reaction mixture and a its oxidation potential is measured via CV.

The measured potentials (V vs Ag/AgI) must be converted to a stable scale. Potentials are scaled versus $Fc|Fc^+$ according to equation (2.2.1), and versus the saturated calomel electrode (SCE) according to equation (2.2.2).

$$E_{\mathrm{Ox/Red}}(\mathrm{vs\ Fc^{+}/Fc}) = E_{\mathrm{Ox/Red}}(\mathrm{vs\ Ag/AgI}) - E_{\mathrm{Fc^{+}/Fc}}(\mathrm{vs\ Ag/AgI}) \quad (2.2.1)$$

$$E^{\ominus}_{\mathrm{Fc^{+}/Fc}} = 0.436\ V \text{ vs SCE in DMF + 0,1 M } n\text{-Bu}_4\text{NBF}_4{}^{132} \quad (2.2.2)$$

Counter Electrode (CE): Two types of counter electrodes were used

(i) Platinum wire fused in a glass tube.

(ii) Graphite rod inserted in a glass tube with a porous tip (G2). The glass tube is partially stuffed with Agar gel and then filled with a 0,1 M solution of *n*-Bu_4NBF_4 in DMF. Such setup allows to keep the anodic compartment (graphite electrode) separated from the reaction mixture, cutting off possible interferences caused by the reaction at the CE.

2.2.2. Potentiostat

Two sets of potentiostat/software were used: (i) Autolab PGSTAT204 potentiostat/galvanostat (Eco-Chemie, Utrecht, Netherlands), connected to a computer with the Nova 2.1 software; (ii) Autolab PGSTAT30 (Eco-Chemie, Utrecht, Netherlands), connected to a computer with the software GPES.

2.2.3. Light Sources

The light sources used in electrophotochemical experiments are: Kessil P160L of 440 nm and 456 nm; homemade 30 W LED systems of 595 nm, 630 nm, 660 nm, 730 nm, 850 nm, 950 nm (CHANZON).

Lamps emission spectra and absolute irradiances were measured with the AvaSpec-Mini2048CL (Avantes) spectrometer, coupled with the software AvaSoft (Appendix D).

GC reflectivity was measured using an 8.7mW commercial Class IIIa red laser and a Glassy Carbon Sheet (Tokai Carbon), polished in the same way as GC electrodes. A Thorlabs PM100USB Power and Energy Meter, with a S120VC sensor was used to measure the power reflected by the GC sheet surface.

2.2.4. Spectroelectrochemistry equipment

Spectroelectrochemistry experiments were carried out with a kit by BAS Inc, comprised of a thin layer quartz glass cell (0,5 mm light pathlength), a Pt gauze WE (80 mesh), a Pt CE, and a non-aqueous Ag^0/Ag^+ RE.

2.2.5. UV-Vis spectrophotometer

UV-vis measurements were registered on an Agilent Cary 60 UV-vis spectrophotometer (Xenon flash lamp, 80 Hz), connected with a computer with Cary WinUV software.

2.2.6. Fluorimeter

A FLS1000 fluorimeter by Edinburgh Instruments was used to record emission spectra, determine excited state lifetimes and measure excited state quenching rate constants. Excitation sources: 450 W Xenon Arc lamp; microsecond flashlamp; pulsed LED (at 280 and 340 nm); pulsed diode lasers (at 405, 635 and 785 nm). Detectors: PMT-980 (range from 185 nm - 980 nm) with instrument response of 600 ps; high speed PMT (200 nm - 850 nm) with instrument response <200 ps; NIR-PMT, in liquid nitrogen cooled housing, (500 to 1700 nm) with photon counting sensitivity and speed. A Peltier controlled holder allows measurement under controlled temperature in the range -40 ÷ 105 °C.

2.2.7. Gel Permeation Chromatography (GPC) equipment

GPC indicates a chromatographic technique that relies on the hydrodynamic radius-based separation of. Analytes are eluted through an immobilized phase within the columns. The used machinery is a chromatograph (Agilent Infinity 1260) equipped with two columns (Agilent PLgel 5 μm MIXED-C 300 x 7.5 mm) connected in series and heated at 60°C was used. The solid phase consists of polystyrene cross-linked with divinylbenzene. The mobile phase is DMF + 10 mM LiBr. Operative flow rate: 1 mL/min. A refractive index detector (RID) is set at 50°C. The calibration curve was constructed based on the elution times of PMMA standards (Agilent EasiVial) fitted with a third-degree polynomial.

2.2.8. Nuclear Magnetic Resonance (NMR) spectrometer

To perform ^{1}HNMR analysis a Bruker 400 Avance III HD spectrometer was used. The spectrometer is coupled with Topspin 3.5 software and equipped with a ^{1}H-^{13}C ATM-*z grad* probehead.

NMR analysis was used to check the purity of used reactants and products, but mostly to determine the conversion percentage from monomer to polymer.

2.3. Setup and procedures

2.3.1. (Photo)electrochemical analysis

To study e-PRC systems a jacketed electrochemical cell with 5 necks was used. The electrochemical setup is made of 3 electrodes (working electrode, reference electrode, counter electrode), connected to a potentiostat and controlled by specific software.

One of the five necks is occupied by the RDE with a GC tip (WE), and which was used for mixing in between CVs. RE and CE (platinum wire) are placed in two other necks. The remaining necks are used as inlet/outlet for degassing the system with an inert (Ar) gas, and to add reagents during the experiments. The temperature of the cell was maintained constat with a Thermo Scientific SC100 thermostat. Before each experiment, the cell was carefully washed with absolute ethanol and acetone and dried in an oven at 60 °C.

The cell was placed inside a plastic box, with a dark curtain to avoid unwanted irradiation.

When irradiation was needed, the cell was placed over the lamp with the targeted wavelength (Figure 14).

The experiments were carried out under inert atmosphere by first degassing the starting solution of solvent and 0,1 M electrolyte. CVs of the blank starting solutions were registered at the operative scan rates. PDI was then added in a 1 mM or 0,5 mM concentration. CVs under dark and under irradiation were then registered at the same rates.

A substrate was then added to the mixture, and the CVs under irradiation were then registered. The concentration of substrates was subsequently increased according to necessities.

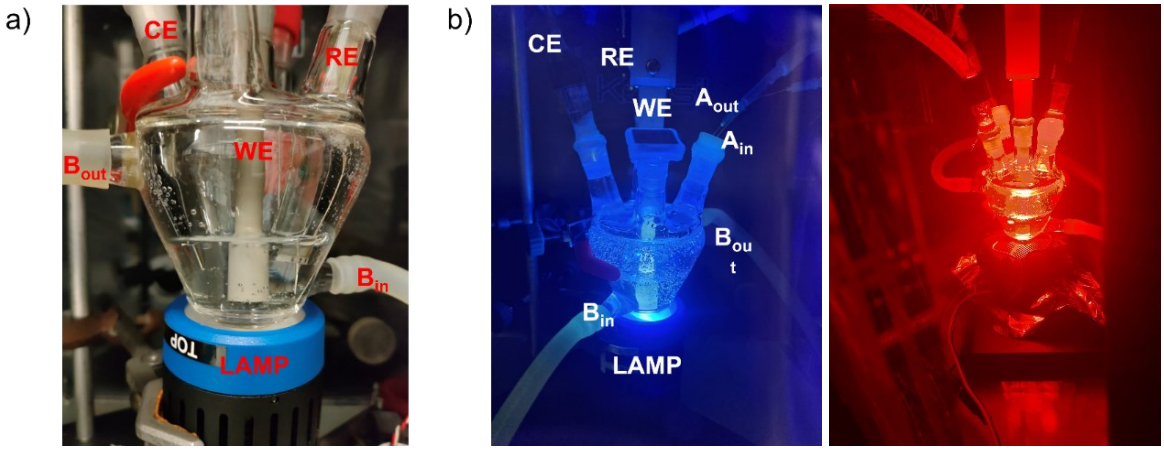

Figure 14. a) Cell setup in with no irradiation. b) Setup with active irradiation (with a 440 nm Kessil lamp and a 630 nm homemade LED). B = thermostat water inlet (in) and outlet (out). A = Argon inlet (in) and outlet (out).

For e-PRC analysis via CV both available potentiostats were used.

2.3.2. Spectroelectrochemical analysis

Spectroelectrochemistry experiments were carried out with a specific kit by BAS Inc.

Electrodes and degassing system were placed as in Figure 15. The Ag wire was immersed in a 0,1 M *n*-Bu_4NBF_4 in DMF solution. The source to degas the solution consists in a 2 L gas balloon previously filled Argon.

The Pt gauze (WE) was activated after every electrolysis.

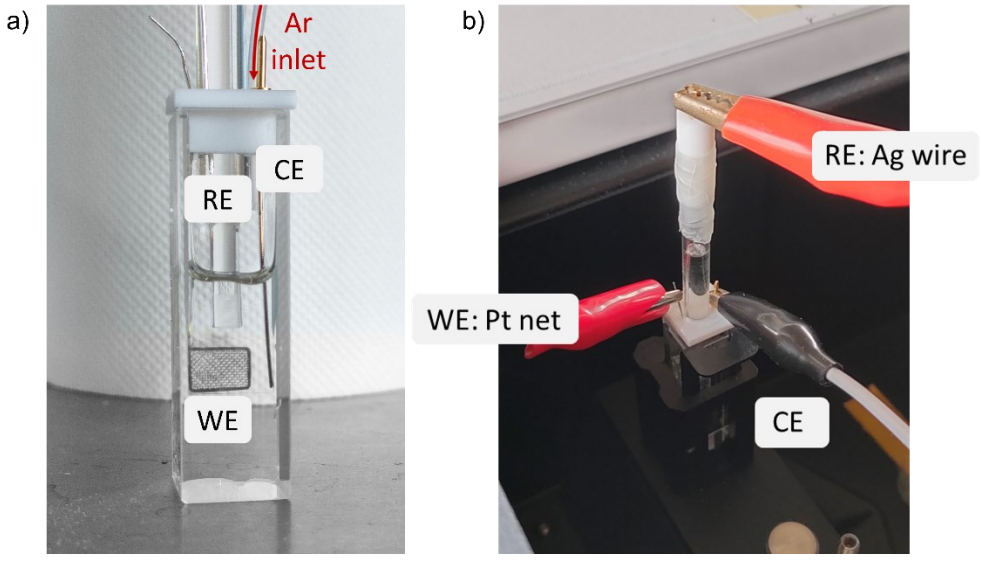

Figure 15. Spectroelectrochemical setup a) from the side and b) from above, when inserted in the spectrophotometer

For spectroelectrochemistry experiments the Autolab PGSTAT204 potentiostat was used.

For each experiment the baseline was registered (solution of DMF + 0,1 M electrolyte). Measurements were carried out under a constant light flow of Ar. UV-Vis spectra were obtained with the Cary 60 spectrophotometer.

2.3.3. PET-eRAFT polymerization experiments

PET-*e*RAFT polymerizations were performed combining electrolysis and constant irradiation.

The experiments were conducted in a 5-neck jacketed electrochemical cell.

The electrochemical setup is made of 3 electrodes (working electrode, reference electrode, counter electrode).

One of the five necks is occupied by a Pt gauze (WE) used to perform electrolysis. RE and CE (graphite electrode in separated cell) are placed in two other necks. A neck accommodates a GC electrode (WE) used to record CVs of the mixture and select the working potential. The remaining neck is used as inlet/outlet for degassing the system with an inert (Ar) gas. The temperature of the cell was maintained constant at 35 °C with a Thermo Scientific SC100 thermostat. Before each experiment, the cell was carefully washed with absolute ethanol and acetone and dried in an oven at 60 °C.

The cell was placed inside a plastic box, with a dark curtain to avoid unwanted irradiation.

The irradiation source is placed beside the cell. The cell is placed under a magnetic stirrer and covered in tin foil. The setup is shown in Figure 16.

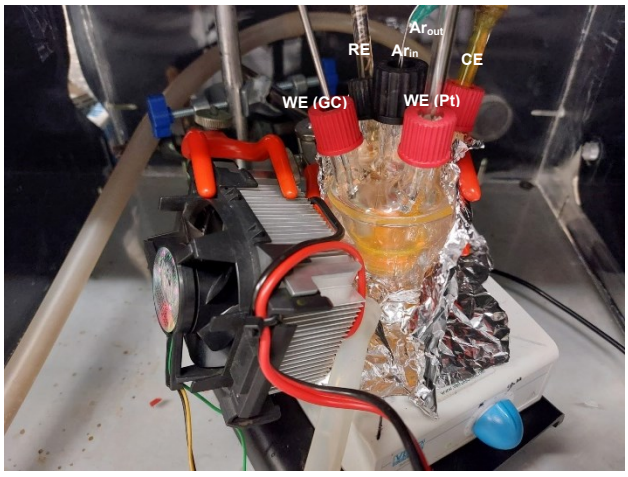

Figure 16. PET-eRAFT polymerization setup

The experiments were carried out under inert atmosphere by first degassing the starting 10 mL solution of DMF + 0,1 M electrolyte + PDI + CDTPA + Monomer. Before adding the monomer, it was passed through basic alumina to remove the inhibiter.

A 1:3 monomer solvent ration was used. Using the GC WE, CVs of the solution were registered to determine working potential to set.at the operative scan rates. Once established the working potential, the Pt WE was connected and a chronoamperometry was set to start (electrolysis process). Light was turned on simultaneously with application of the potential.

Before the beginning of the polymerization a sample is taken (with a degassed needle) from the mixture to have a “zero time” reference.

Periodically (typically every 1h) a sample was taken from the mixture (with a degassed needle). An aliquot was put in an NMR tube (to determine the monomer conversion) and the remaining part was used to prepare a GPC sample.

2.3.4. GPC analysis

To analyze reaction samples with GPC, the aliquot taken from the reaction mixture is first diluted with DMF (to a theoretical concentration of 1-2 mg/mL of polymer); then it’s filtrated with neutral alumina and only after is injected in the instrument (60-100 μL injection).

The eluted chromatograms are integrated with an integrated software to obtain information on the polymer.

NMR analysis and determination of monomer conversion

The samples destined for NMR analysis were prepared in NMR tubes. Each tube is filled to have 1-2 mg/mL concentration. All the analyses were performed with $CDCl_3$ as solvent.

To determine the conversion of methyl methacrylate (MMA) into poly-methyl methacrylate (PMMA) the ratio between the signal at 3,78 ppm (relative to MMA) and the one at 3,58 ppm (relative to PMMA) is evaluated.

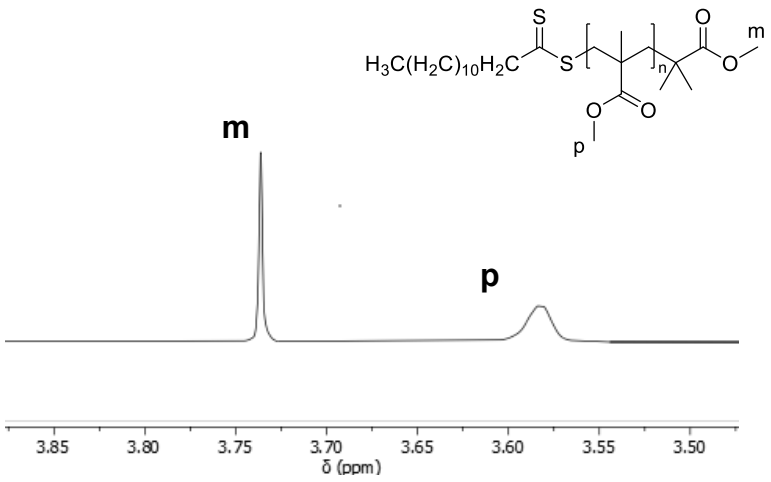

Figure 17. NMR spectrum of PPMA in $CDCl_3$, resulting from the RAFT polymerization with CDTPA.

Conversion is calculated as:

$$\text{Conversion } \% = \frac{A_p}{A_m + A_m} \cdot 100 \tag{2.3.1}$$

Where A_m is the area of the signal relative to the monomer and A_p to the one relative to the polymer.

3. Results and Discussion

3.1. Determination of rate constants in electro-photocatalytic processes via CV analysis

To investigate the electro-photocatalytic behavior of *N,N'*-Bis(2,6-diisopropylphenyl)-3,4,9,10-perylenetetracarboxylic diimide – here referred to as PDI – the cyclic voltammetry (CV) technique was utilized.

Catalytic activity of PDI was tested on various substrates bearing a cleavable carbon-halogen bond (Figure 18).

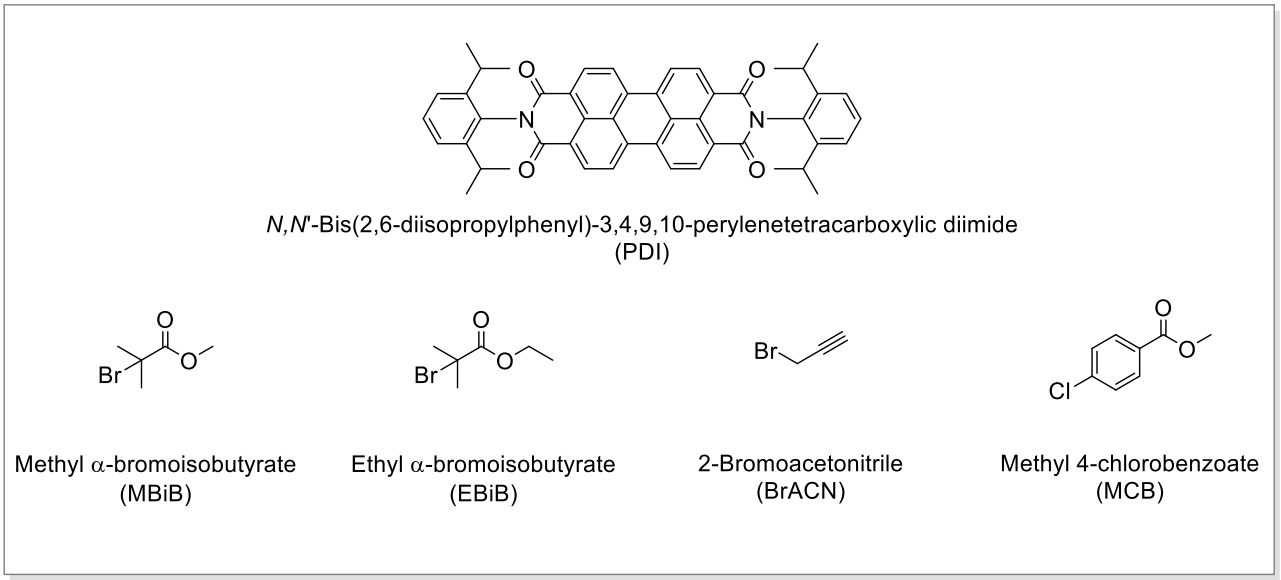

Figure 18. Structures of PDI and alkyl halide and aryl halide substrates.

As shown in the dashed line in Figure 19a the cyclic voltammetry (CV) of PDI shows two consecutive and reversible peak couples, associated to the formation of the reduced states $PDI^{\bullet-}$ and PDI^{2-}, according to the following reversible electron transfers (ETs):

$$PDI + e^- \rightleftarrows PDI^{\bullet-} \quad (3.1.1)$$

$$PDI^{\bullet-} + e^- \rightleftarrows PDI^{2-} \quad (3.1.2)$$

Both reduced forms of PDI can be prepared via electrolytic reduction. They absorb radiation in the visible region (Figure 19b), thus becoming competent photocatalysts for reduction reactions. PDI^{2-} is expected to be more reactive given its more negative reduction potential and higher-energy absorption spectrum.

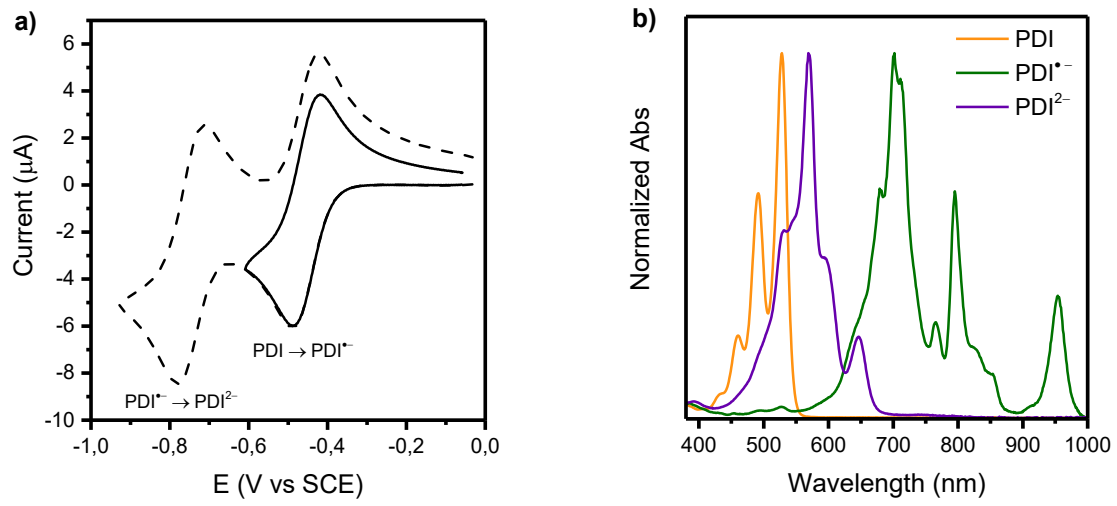

Figure 19. a) CV of 1,0 mM PDI in DMF + 0,1 M n-Bu_4NBF_4 on a GC electrode (A = 7,07 mm^2) at T = 25 °C. Scan rate = 0,03 V s^{-1}. CV in the dashed line was recorded with a more negative inversion potential. b) Spectra of PDI and its reduced species; data obtained via spectroelectrochemistry. UV-Vis spectra recorded after reduction of 0,25 mM PDI in DMF + 0,1 M n-Bu_4NBF_4 on a platinum electrode at –0,55 V to obtain $PDI^{\bullet-}$ and at –1,2 V to obtain PDI^{2-}.

The following treatment will focus first on the catalytic behavior of $PDI^{\bullet-}$. The selective investigation of the properties of $PDI^{\bullet-}$ was possible by utilizing CV with a limited potential range: the inversion potential (E_λ) was selected to prevent formation of PDI^{2-} (solid line in Figure 1a). The photocatalytic properties of the doubly reduced species, PDI^{2-}, will be treated later in the text.

3.1.1. Reactivity of the excited state of the anion radical catalyst, $*PDI^{\bullet-}$

The targeted reaction for $PDI^{\bullet-}$ as photocatalyst is the reduction of organic halides (RX) frequently used as ATRP initiators, with the proposed catalytic cycle shown in Scheme 11. First PDI is electrochemically reduced to $PDI^{\bullet-}$. Second, this radical anion is photoexcited to form $*PDI^{\bullet-}$. To close the cycle, this excited state catalyst can reduce the RX substrate, with irreversible cleavage of the carbon-halogen bond forming the $R^\bullet$ radical and the halide anion X^-.

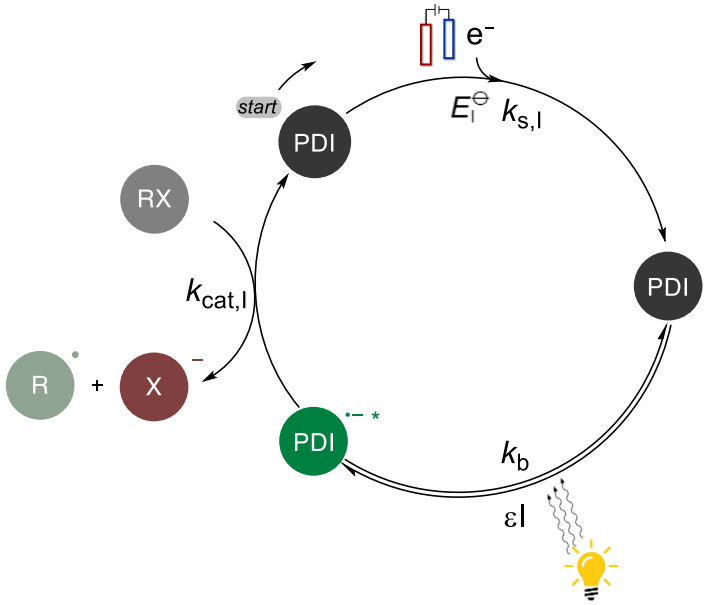

*Scheme 11. Mechanism of electro-photocatalytic reduction of RX involving *PDI $^{\bullet-}$.*

Electrochemical experiments have been carried out to determine the reactivity of this photocatalytic cycle, in particular to determine the rate constant of the photocleavage of the C−X bond, $k_{cat,I}$. Using CV to study excited-state redox processes is a novel concept emerging from the recent resurgence in electrophotocatalysis. Costentin et al. developed a rigorous theoretical CV method for studying these cycles,[75] which has yet to be experimentally applied—our goal in this work.

Photocatalytic cycles with fleeting intermediates like *PDI$^{\bullet-}$, which have picosecond lifetimes, typically require ultrafast spectroscopic techniques (e.g., pump-probe methods) for quantitative study such as determination of electron transfer rate constants. Pump-probe methods, however, demand specialized equipment and training. Instead, we propose to study ultrafast reactions in a quantitative way using more accessible CV methods, which can be carried out with common potentiostats found in most laboratories.

CV is a strong electroanalytical tool that has been vastly implemented to study catalytic processes. It allows to study the reversibility of an electron transfer (ET) and for reversible waves it readily gives access to the standard redox potential $E^{\ominus}$, which can be directly estimated from the half-wave potential, $E_{1/2}$. While providing qualitative and quantitative information about the system, CV is also particularly useful to study and determine reaction mechanisms. In summary CV's strength stands in its experimental simplicity and its ability to easily probe the effect of time (t) and potential (E) on the current (i).[133]

As previously mentioned, introducing a photochemical event into an electrochemical process generates complications in the CV pattern, mostly related to a change in mass transfer. To implement an

electrocatalytic cycle and determine the kinetic rate constant of the reaction between an excited state catalyst and a substrate (k_{cat}), the following step-by-step protocol has been designed and carried out, as described in this chapter[75]:

(i) **CV analysis of the photocatalyst in the dark**: This step evaluates the interfacial parameters of the photocatalyst in its ground state, such as the reduction potential $E^{\ominus}(PC/PC^{\bullet-})$, the rate constant of heterogeneous electron transfer (k_s), and the diffusion coefficient (D).

(ii) **Preparation by bulk electrolysis in the dark of the ion radical of the photocatalyst:** This step allows determination of the photophysical properties of the ion radical, including the extinction coefficient (ε) and excited state lifetime ($1/\tau = k_b$). It also helps identify the suitable excitation wavelength where $PC^{\bullet-}$ absorbs light while PC does not.

(iii) **CV analysis of the photocatalyst under irradiation and in the absence of substrate**: This step assesses the effect of local heating due to light irradiation (I), determining the maximal diffusion layer thickness $\delta(I)$ caused by convection, as well as any potential change in the diffusion coefficient.

(iv) **CV analysis under irradiation and in the presence of the substrate**: This step evaluates the catalytic rate constant (k_{cat}).

Note that the experimental setups are more extensively described in Chapter 2 (Experimental section).

i) Study of the electrochemical system in the dark

As a first step, the PDI catalyst was studied leaving out the photochemical events to understand and quantify its electrochemical properties.

Firstly, CV of PDI in the dark allows us to evaluate the reversibility of the system and to define the standard redox potential of $PDI^{\bullet-}$ (and PDI^{2-}) as its halfwave potentials ($E_{1/2} \approx E^{\ominus}$). Results obtained from such analysis are reported in Figure 20a and

Table 2.

From CV data at different scan rates, it is also possible to calculate two important parameters associated to the dynamics of electron transfer to PDI: the heterogeneous rate constant for the electron transfer (k_s) and the diffusion coefficient (D). These parameters will be used later to obtain kinetic information on the electrophotocatalytic cycle.

A value of $k_s = 0{,}0108 \pm 0{,}0003$ cm s^{-1} was determined via the Nicholson method (see Appendix B). This value indicates a quasi-reversible electron transfer, and it is typical for large organic molecules.

Additionally, it is possible to determine the diffusion coefficient (D) of PDI from the cathodic peak current (i_{pc}) at different scan rates (Figure 20a) with the Randles-Sevcik equation:

$$i_{pc} = 0{,}4463\mathrm{n}FAC\sqrt{\frac{\mathrm{n}F\nu D}{RT}} \tag{3.1.3}$$

From which the value of D can be calculated from the slope of the i_{pc} vs $\nu^{1/2}$ plot:

$$D = -\frac{RT\left(\partial i_{p,c}/\partial \nu^{1/2}\right)^2}{\mathrm{n}F\,(0{,}4663\mathrm{n}FC)^2} \tag{3.1.4}$$

where n is the number of exchanged electrons (1 in our case one), F is the Faraday constant (96485 C mol^{-1}), A is the working electrode surface, C is the concentration of the species, ν is the scan rate, R is the gas constant (8,314 J K^{-1} mol^{-1}) and T is the working temperature.

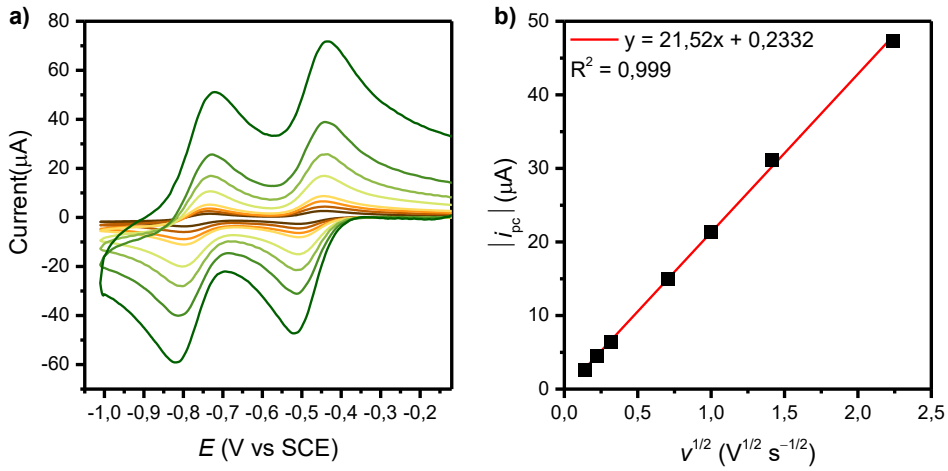

Figure 20. a) CV of 0,5 mM PDI in DMF + 0,1 M n-Bu$_4$NBF$_4$ on a GC electrode (A = 7,07 mm^2) at T = 26 °C. Scan rates = 0,02 V s^{-1} - 5 V s^{-1}. b) Linear fit of i_{pc} vs $\nu^{1/2}$ for the first peak.

Figure 20b shows a linear trend for the i_{pc} vs $\nu^{1/2}$ values, as expected from (3.1.3). From the slope of the regression line, it is possible to determine the diffusion coefficient, since all the other variables of the Randles-Sevcik equation are known.

Table 2. Electrochemically determined quantities relative to PDI$^{\bullet-}$ and PDI^{2-}.

Entry	Redox couple	$E^{\ominus}$ [a] (V vs SCE)	k_s [b] (cm^{-1}s^{-1})	δ (cm)	D [c] (cm^2 s^{-1})
1	PDI/PDI$^{\bullet-}$	−0,45	0,0108	/	3,1 × 10^{-6}
2	PDI$^{\bullet-}$/PDI^{2-}	−0,74	0,0108	/	/

[a] The standard redox potential value is determined as the half-wave potential measured by cyclic voltammetry. [b] Measured using the Nicholson method (see Experimental section). [c] Determined by using Randles-Sevcik equation.

When both PDI catalyst and an RX substrate are present in solution in the dark, traditional electrocatalysis (no light) may ensue. The mechanism of traditional electrocatalysis is shown in Scheme 12.

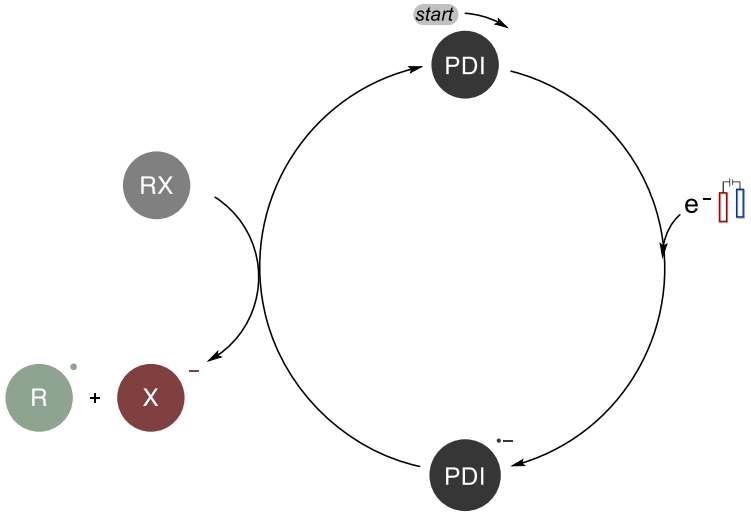

Scheme 12. Electrochemical reduction of RX mediated by PDI in the absence of irradiation sources.

Testing all the substrates in Figure 18 it emerged that without irradiation in the presence of the alkyl halide methyl α-bromoisobutyrare (MBiB), no electrocatalytic effect was detectable via CV investigation (Figure 21). If presente, a catalytic effect can be determined by an increase of $i_{p,c}$ for a reduction process. Quantitatively, to evaluate the catalytic effect one should consider the ratio between current in presence of substrate (i_{pc}) and in absence of substrate ($i_{pc,0}$). If there is a catalytic effect, the catalyst regenerates during the CV scan, according to the cycle in Scheme 12, leading to an apparent increase in its concentration and consequently an increase in the measured current. When studying the reduction by $PDI^{\bullet-}$ with no irradiation in the presence of MBiB, the lack of catalytic current was evident. Even when increasing the value of γ (the ratio between substrate and catalyst concentration, $\gamma = C_{RX}/C_{PDI}$) no catalytic current was observed, $i_{pc}/i_{pc,0}$ remained constant, indicating the absence of any electrocatalysis in the dark. This is a particularly important result because it implies that any catalytic effect described next is solely due to the role of light any electrocatalysis in the dark.

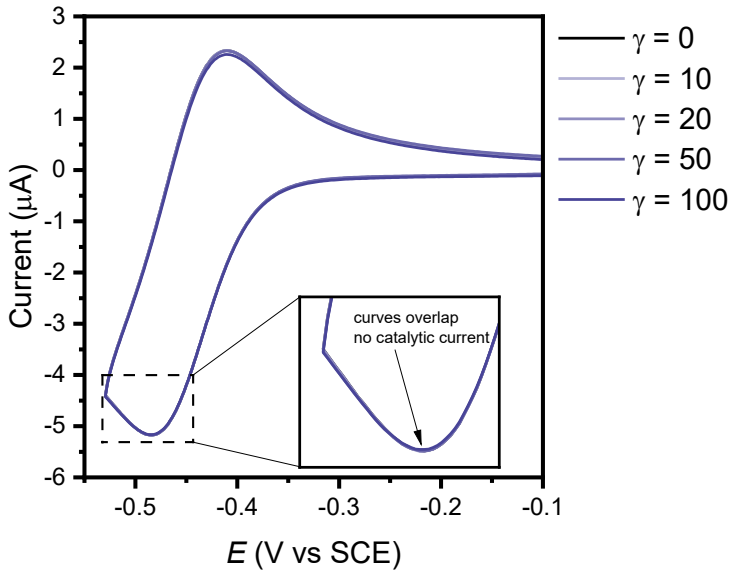

Figure 21. CVs of 1,0 mM PDI in the absence and in the presence of MBiB. The factor γ represents the concentration ratio between substrate (MBiB) and catalyst (PDI). The value γ = 0 indicates that only PDI is present in the reaction mixture. CV performed in DMF + n-Bu$_4$NBF$_4$ (0,1 M) on a GC electrode (A = 7,07 mm^2) at T = 25 °C. Scan rate = 0,02 V s^{-1}.

ii) Preparation by bulk electrolysis in dark of the ion radical of the photocatalyst

The radical anion PDI$^{\bullet-}$ was generated by spectroelectrochemistry (see setup in Experimental part), and its spectrum measured (continuous line in Figure 22a). The spectrum of PDI$^{\bullet-}$ was considerably red-shifted compared to that of the parent molecule PDI (dashed line in Figure 22a). This clean shift enabled the selection of the irradiation source as a 30 W 630 nm LED (also shown in Figure 22a). The use of a red light allows to selectively excite the PDI$^{\bullet-}$, without interference from the neutral PDI. With such a system it is possible to decouple the electrochemical and photochemical event and avoid unwanted reactions prior to the formation of the reduced species.

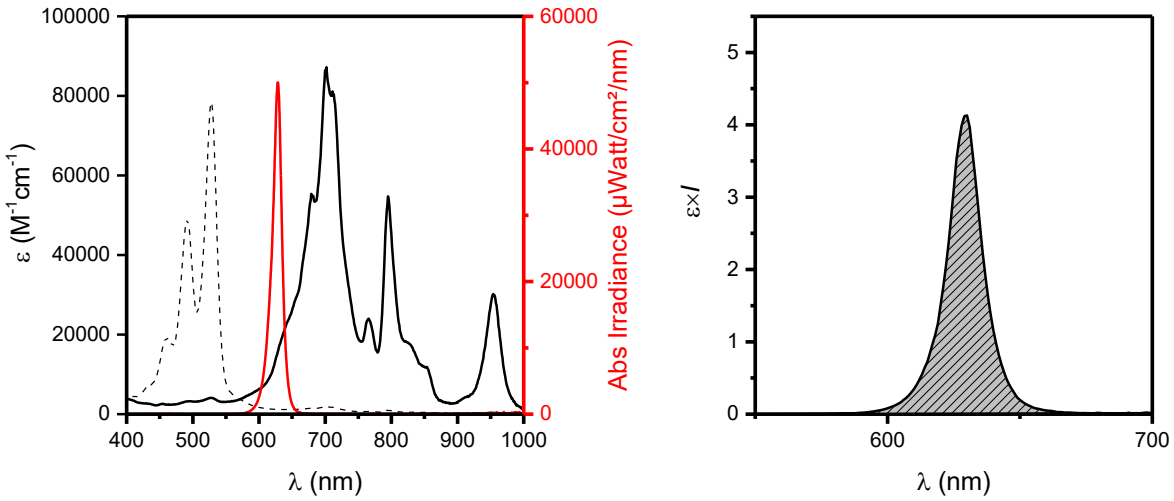

Figure 22. a) Spectra of PDI (ashed line) and $PDI^{\bullet-}$ (green line) with absolute irradiance of the 630 nm LED. Absorption spectrum of $PDI^{\bullet-}$ acquired with spectroelectrochemical experiment: reduction in a 0,5 mm cuvette (inert atmosphere) of 0,3 mM PDI in DMF + + n-Bu_4NBF_4 (0,1 M) on a Pt WE at a potential of −0,55 V vs SCE. Absolute irradiance measured with an Avantes AvaSpec spectrophotometer. b) Probability of excited state formation calculated as the integral under the εI vs λ curve.

Electrochemically, $PDI^{\bullet-}$ is generated in a thin layer close to the electrode surface (see Experimental Setup Figure 14). Under irradiation, the rate of formation of the excited state can be calculated as the product between the molar absorption coefficient of the active species and the LED irradiance, $\varepsilon \times I$.

$$PDI^{\bullet-} \xrightarrow{\varepsilon I} {}^{*}PDI^{\bullet-} \tag{3.1.5}$$

For greater accuracy, εI was calculated as a function of wavelength and then integrated (Figure 22b). To refine the estimate of εI, we considered for two additional effects:

(i) Light reflection from the GC electrode surface increases the effective irradiance. Reflection from the GC surface was estimated at 16% by measuring the intensity of red laser light reflected using an Avaspec spectrometer.

(ii) Radiation absorbed by PDI in the thin diffusion layer (δ), which reduces the effective irradiance. Radiation absorbed can be determined from the transmittance value (3.1.6). In our system, ca. 12% of light was absorbed in the maximal diffusion layer.

$$A = \varepsilon_{635} \times \delta \times C_{\mathrm{PDI}} \tag{3.1.6}$$

$$1 - T = 1 - 10^{(2-A)} \tag{3.1.7}$$

In our system two effects were relatively small and they tended to cancel each other out. Therefore, they were neglected in our calculation of the rate of formation of the excited state.

The lifetime of the generated $^{*}PDI^{\bullet-}$ is also an important parameter. This was measured in the literature at 160 ps[134].

iii) CV analysis of the photocatalyst under irradiation and in the absence of substrate

After assessing the nature of the electrochemical system in the dark, and selecting the appropriate wavelength for the catalyst photoexcitation, our analysis shifted towards understanding the effect of 630 nm irradiation on the CV.

Irradiating the electrode surface altered the CV trace (Figure 23a), increasing cathodic and decreasing anodic currents. With no substrate present, this shift indicates a change in mass transport under irradiation. To model this, a brief description of mass transport at the electrode is necessary.

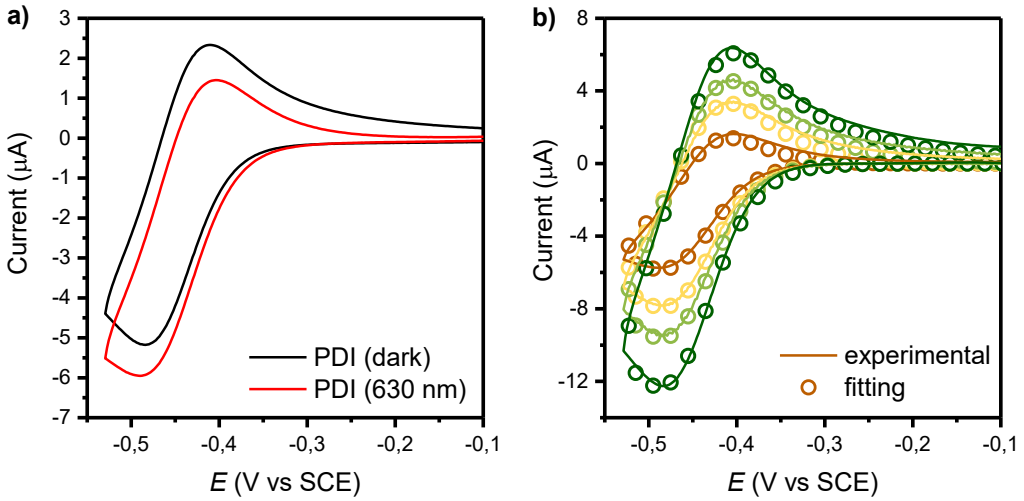

Figure 23. a) Effect of irradiation with a 630 nm LED on a solution of 1,0 mM PDI. Scan rate = 0,02 V s^{-1} b) experimentally obtained CVs of 1.0 mM PDI under irradiation at different scan rates (full lines) with respective simulated data (circles). All the CVs are performed in DMF + n-Bu_4NBF_4 (0,1 M) on a GC electrode (A = 7,07 mm^2) at T = 25 °C.

CV is a transient technique performed at a stationary electrode where molecular diffusion regulates mass transfer. In a traditional CV the dynamic treatment of species concentrations is simplified by considering the presence of a diffusion layer of thickness δ at the electrode surface, which is time-dependent for transient measurements and can be approximated as[133]:

$$\delta(t) = 2\sqrt{(Dt)} \tag{3.1.8}$$

where *D* is the diffusion coefficient and *t* is time. Therefore, in traditional CV (in the dark) diffusion is semi-infinite and δ continuously increases over time. Time-dependent diffusion profiles are schematically represented in Figure 24 (left).

During an e-PRC reaction the temperature in the immediate vicinity of the electrode increases due to continuous light absorption and consequent non-radiative decay of the excited state reduced photocatalyst ($*PC^{\bullet-}$). The local heating alters mass transport conditions and creates convective thermal gradients. This enhanced mass transport upon irradiation has the effect of changing the diffusion mode from semi-infinite to non-infinite (Figure 24 right). In turn, this influences diffusion layer thickness δ, which quickly approaches a stationary value under light irradiation. Therefore, the system approaches steady state conditions and a Nernst diffusion layer of fixed thickness δ can be assumed. The δ defines the space in which the photocatalytic process can occur, as the concentration of $PC^{\bullet-}$ is negligible beyond this layer.

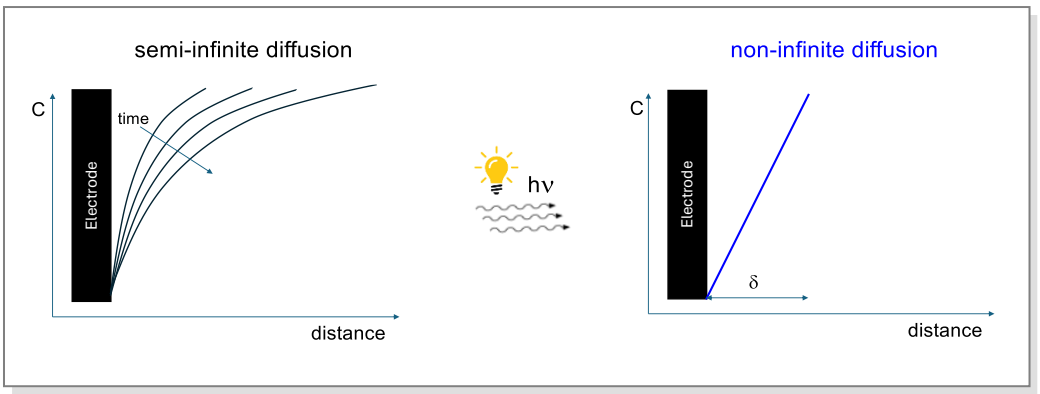

Figure 24. Change in mass transport regime and diffusion layer. The system transitions from semi-infinite diffusion to non-infinite diffusion when irradiated.

Given the mathematical complexity of treating the unconventional non-infinite diffusion mode in cyclic voltammetry, we used DigiElch simulation software to analyze the experimental CV data and obtain quantitative results on the mass transport under irradiation. The software, given the specifics about the system and all the significant reactions, can fit the experiment CV traces returning kinetic and thermodynamic data, including the thickness of the Nernst diffusion layer (δ) and the diffusion coefficients.

The CV fitting procedure proceeded as follows. First, a series of CVs under irradiation at different scan rates was collected (solid lines in Figure 23b). Second, the experimental CV traces were fitted via the simulation software by setting a non-infinite diffusion mode with an arbitrary value for the Nernst diffusion layer δ = 50 µm. This fitting procedure was repeated with different δ values, adjusted in 5 µm increments, until the best match between experimental and simulated CVs was achieved. The match quality was tracked using the standard deviation between the experimental and simulated CVs, as provided by the software. For PDI under 30 W 630 nm irradiation, the best fit, obtained with δ = 75 µm, is shown in Figure 23b and demonstrates very good congruence with the experimental data. In addition, the software returned the diffusion coefficient under irradiation, $D = (5{,}1 \pm 0{,}1) \times 10^{-6}$ $cm^2\ s^{-1}$, which is ca. 50% higher than the value measured in the dark. This is in line with an increased temperature at the electrode surface.

To calculate the effective temperature at the electrode, we built a calibration curve by determining the diffusion coefficient of PDI as a function of temperature (in the dark).The diffusion coefficients were measured by CV using the Randles-Sevcik equation, and plotted in an Arrhenius plot (Figure 25). The experimental data of the diffusion coefficient under irradiation was then interpolated in the calibration line to extract the effective temperature, which resulted 51 ± 1 °C.

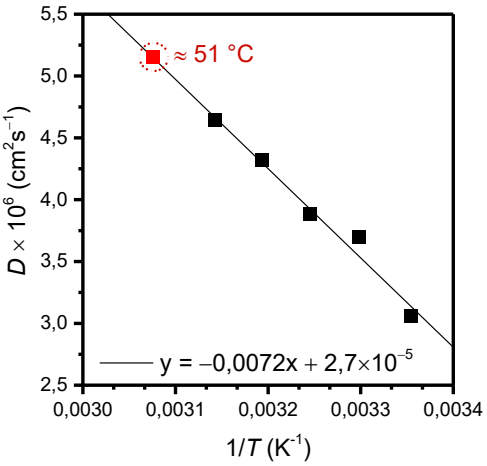

Figure 25. Estimation of the temperature at the electrode by evaluation of the PDI's diffusion coefficient. The experimental value for CV under irradiation (red dot) is interpolated in a calibration line (dashed line) built on a set of D values obtained at set temperatures. The D values were obtained using the Randles-Sevcik equation. The CV scans are performed on a mixture of 1,0 mM PDI in DMF + 0,1 M n-Bu$_4$NBF$_4$ on a GC electrode (A = 7,07 mm^2) at T ranging from 25 °C to 45 °C; scan rate = 0,02 – 10 V s^{-1}.

iv) CV analysis under irradiation and in the presence of the substrate

After studying the effect of light alone on CV, we moved to the final step of studying the full electro-photocatalytic cycle in the presence of both light irradiation and RX substrate (Scheme 11). In the dark, the radical anion of PDI has poor reducing abilities with $E^{\ominus}$ = –0,45 V vs SCE. Instead, when irradiated its reducing ability is boosted by the energy of the absorbed photons and its excited state reaches $E^{\ominus}$ = –1,87 V vs SCE[72].

Addition of a substrate in the presence of light provoked an increase in cathodic current and a decrease in the anodic one (Figure 26), indicating the occurrence of electrophotocatalysis in agreement with the mechanism in Scheme 11. The catalytic current is generated by the reduction of MBiB by the excited state open shell catalyst (*PDI$^{\bullet-}$), which regenerates the neutral form of the catalyst (PDI) that is reduced again at the electrode. From a qualitative perspective, the catalytic reduction of the substrate was not too fast, as it caused only a relatively slight change in the CV pattern. This is evident from the slight increase in cathodic current at high γ (high substrate concentration) with a slow scan rate of 0,02 V s^{-1} (slower scan rates enhance the relatively slow electrophotocatalytic cycle). Inefficient catalysis is consistent with the short lifetime of *PDI$^{\bullet-}$ and its relatively mild excited state potential.

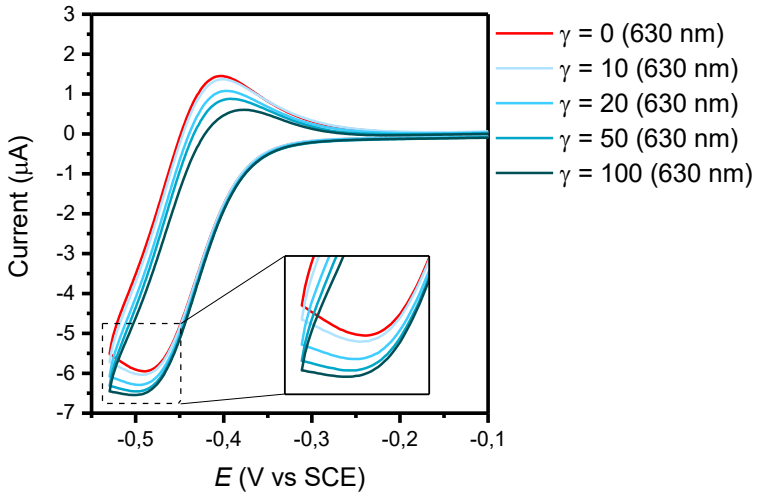

Figure 26. CV under irradiation (630 nm) of 1,0 mM PDI with increasing concentration of MBiB. CVs are performed in DMF + 0,1 M n-Bu$_4$NBF$_4$ on a GC electrode (A = 7,07 mm^2) at v = 0.02 V s^{-1} and T = 25 °C.

Our aim is now to use the CV simulation software to extract quantitative kinetic information from the CVs under electrophotocatalytic conditions. This method proceeds via three steps: i) first, a large series of experimental CVs (ca. 25 individual traces) was recorded for different values of substrate concentrations and at different scan rates; ii) second, an accurate reaction mechanism was defined to use as input for the CV simulation software; iii) finally, fitting of experimental CVs enabled the determination of the RX activation rate constant $k_{cat,I}$ (here the subscript "I" indicates that we are investigating PDI$^{\bullet-}$, the first reduced state of PDI).

To define a complete electrophotocatalytic mechanism, all possible reactions occurring close to the electrode must be considered, most of which have already been described in Scheme 11. In addition to the main electrophotocatalytic cycle, however, the following reactions must be considered:

(i) Back electron transfers (BET)

The excited state catalyst *PDI$^{\bullet-}$ can undergo heterogenous BET at the electrode ($k_{BET,het}$) and homogenous BET with its ground state PDI ($k_{BET,hom}$) according to the following reactions.

$$*PDI^{\bullet-} \rightarrow PDI + e^- \qquad k_{BET,het}\,(cm\ s^{-1}) \qquad / \qquad (3.1.9)$$

$$*PDI^{\bullet-} + PDI \rightarrow PDI + PDI^{\bullet-} \qquad k_{BET,hom}\,(M^{-1}\ s^{-1}) \qquad 1{,}62 \times 10^{-5} \qquad (3.1.10)$$

Heterogeneous BET is highly favored since *PDI$^{\bullet-}$ is oxidized at the electrode surface at a very high rate because the corresponding $E^{\ominus}$(PDI/*PDI$^{\bullet-}$) is much more negative than $E^{\ominus}$(PDI/PDI$^{\bullet-}$). However, the concentration of *PDI$^{\bullet-}$ at the electrode surface is basically null[75], which makes heterogenous BET negligible. To exclude the reaction with absolute certainty it was tested in simulation, setting a

value of $k_{BET,het}$ = 0,01 cm s^{-1} (similar to the value determined for the ground state molecule). The reaction was confirmed to be irrelevant.

Homogenous BET, instead, was considered in our CV fitting procedure, which requires estimation of its rate constant $k_{BET,hom}$. The driving force for reaction (3.1.8) is huge, given the big difference (1,12 V) between the standard potentials of the two redox couples. Therefore, the reaction was supposed to ΔG^0 of the reaction becomes so negative with respect to the reorganization energy λ ($\Delta G^0 << -\lambda$) that the reaction enters the Marcus inverted region and, hence, becomes kinetically hampered[135]. The reaction rate is so low that the homogeneous BET can be considered negligible with respect to other reactions of the excited radical anion, $*PDI^{\bullet-}$.

Additionally, sensitivity analysis performed on the simulated CVs with this reaction set to the maximum possible rate (i.e. diffusion limited), showed that it had small to negligible effect on the simulated voltammograms.

The diffusion-controlled rate reaction was calculated as:

$$k_{\mathrm{d}} = \frac{8RT}{3\eta} \tag{3.1.11}$$

where η is the medium dynamic viscosity, which corresponds to 0,672 mPa·s for DMF at 51 °C [136].

(ii) Reactions of the radical anion catalyst $PDI^{\bullet-}$

According to well-known electrocatalytic cycles involving the reductive cleavage of R–X bonds, organic radical anions such as $PDI^{\bullet-}$ can react with radicals $R^{\bullet}$ via coupling or reduction, according to the following reactions[137]:

$$PDI^{\bullet-} + R^{\bullet} \rightarrow PDI - R^{-} \qquad k_c\,(M^{-1}\,s^{-1}) \qquad 10^9 \tag{3.1.12}$$

$$PDI^{\bullet-} + R^{\bullet} \rightarrow PDI + R^{-} \qquad k_{ET}\,(M^{-1}\,s^{-1}) \qquad \text{see Table 3} \tag{3.1.13}$$

Values of k_c of the order of 10^9 M^{-1} s^{-1} have been reported for the coupling between alkyl radicals and aromatic radical anions[138,139].

Reaction (3.1.13) is an outer sphere electron transfer between two organic molecules, therefore k_{ET} could be estimated by applying standard kinetic theories such as those of Arrhenius and Marcus's theory for electron transfer.

$$k_{\mathrm{ET}} = Z\mathrm{e}^{-\frac{\Delta G^{\ddagger}}{RT}} \tag{3.1.14}$$

where Z is the collision frequency and $\Delta G^{\ddagger}$ is the activation free energy of the reaction.

The details of the calculation are reported in the following section, where Marcus's theory is treated in detail, but a brief description is also provided here. $\Delta G^{\ddagger}$ depends on the standard reduction potential of the radical species R$^{\bullet}$ ($E^{\ominus}_{R^{\bullet}}$) that was taken from the literature[137]. The quantities related to the radical derived from EBiB were approximated as equal to those of the corresponding radical from MBiB. This approximation is justified because the presence of a methyl group instead of an ethyl group in the side chain of an alkyl compound has minimal, if any, impact on $E^{\ominus}_{R^{\bullet}}$ and λ[140]. The obtained values of k_{ET}, together with the necessary parameters for the estimation using Marcus's theory, are summarized in Table 3.

Table 3. Values of k_{ET} between PDI$^{\bullet-}$ and various substrate calculated via Marcus's theory.

R$^{\bullet}$ precursor	k_{ET} (M^{-1} s^{-1})	$E^{\ominus}_{R^{\bullet}}$ (V vs SCE)	ΔG^0 (kJ mol^{-1})	Z (M^{-1} s^{-1})	λ (kJ mol^{-1})
MBiB	$3{,}96 \times 10^3$	−0,66	20,26	$5{,}799 \times 10^{11}$	160
EBiB	$3{,}88 \times 10^3$	−0,66	20,26	$5{,}688 \times 10^{11}$	160
BrACN	$4{,}40 \times 10^4$	−0,72	26,05	$7{,}572 \times 10^{11}$	122

The obtained values for k_{ET} are low with respect to other reactions at play. Therefore, they have no effect on the overall mechanism.

With the same method, we estimated the rate constant for the reduction of radicals by *PDI$^{\bullet-}$ ($k_{ET*,I}$).

$$*PDI^{\bullet-} + R^{\bullet} \rightarrow PDI + R^{-} \qquad k_{ET*,I}\,(M^{-1}\,s^{-1}) \qquad 9{,}8 \times 10^{10} \qquad (3.1.15)$$

The calculated value exceeds the diffusion-controlled rate constant (k_d). However, since the concentration of both *PDI$^{\bullet-}$ and R$^{\bullet}$ are very small, this reaction when tested in the simulation software is confirmed to be negligible.

The full e-PRC mechanism and the utilized simulation parameters are summarized below. It must be noted that all parameters excluding $k_{cat,I}$ can be independently measured or estimated with sufficient accuracy. Therefore, only the unknown parameter $k_{cat,I}$ is left to refine by the CV fitting software.

$^*PDI^{\bullet-} + RX \rightarrow PDI + R^{\bullet} + X^-$	$k_{cat,I}$ (M^{-1} s^{-1})	*fitted*	(3.1.16)
$PDI + e^- \rightleftarrows PDI^{\bullet-}$	$k_{s,I}$ (cm s^{-1})	0,0108	(3.1.1)
$PDI^{\bullet-} + h\nu \rightarrow {}^*PDI^{\bullet-}$	$k_{\varepsilon I}$ (s^{-1})	73,57	(3.1.5)
$^*PDI^{\bullet-} \rightarrow PDI^{\bullet-}$	k_b (s^{-1})	$6{,}25\times10^9$	(3.1.17)
$PDI^{\bullet-} + R^{\bullet} \rightarrow PDI - R^-$	k_c (M^{-1} s^{-1})	10^9	(3.1.12)
$R^{\bullet} + R^{\bullet} \rightarrow RR$	$k_{c'}$ (M^{-1} s^{-1})	10^9	(3.1.18)
$^*PDI^{\bullet-} + PDI \rightleftarrows PDI + PDI^{\bullet-}$	$k_{BET,hom}$ (M^{-1} s^{-1})	$1{,}62 \times 10^{-5}$	(3.1.10)
$PDI^{\bullet-} + R^{\bullet} \rightleftarrows PDI + R^-$	k_{ET} (M^{-1} s^{-1})	see Table 3	(3.1.13)

The decay rate constant of the excited state, k_b, was calculated as the reciprocal of the excited state species lifetime (τ_0). For the anion radical $\tau_0(^*PDI^{\bullet-})$ = 160 ps,[134] and thus $k_b = 6{,}25\times10^9$ s^{-1}.

To determine $k_{cat,I}$ of the dissociative electron transfer to RX, all the other parameters are fixed including δ = 75 μm and $D = 5{,}1\times10^{-6}$ cm^2 s^{-1} for PDI, and the software iteratively adjusts the fitting varialble $k_{cat,I}$ until it finds the best match between experimental and simulated CVs. To improve the quality of the fitting, a series of experimental voltammograms is recorded at different values of γ and scan rates. In Figure 27a is reported the superimposition of simulated data on the set of experimental CVs with increasing γ at one scan rate. Simulations are also shown at various scan rates (Figure 27b). It is evident that with the increase of the scan rate the catalytic effect decreases, becoming undetectable in the faster range of scan rates, i.e., shorter time of CV scan.

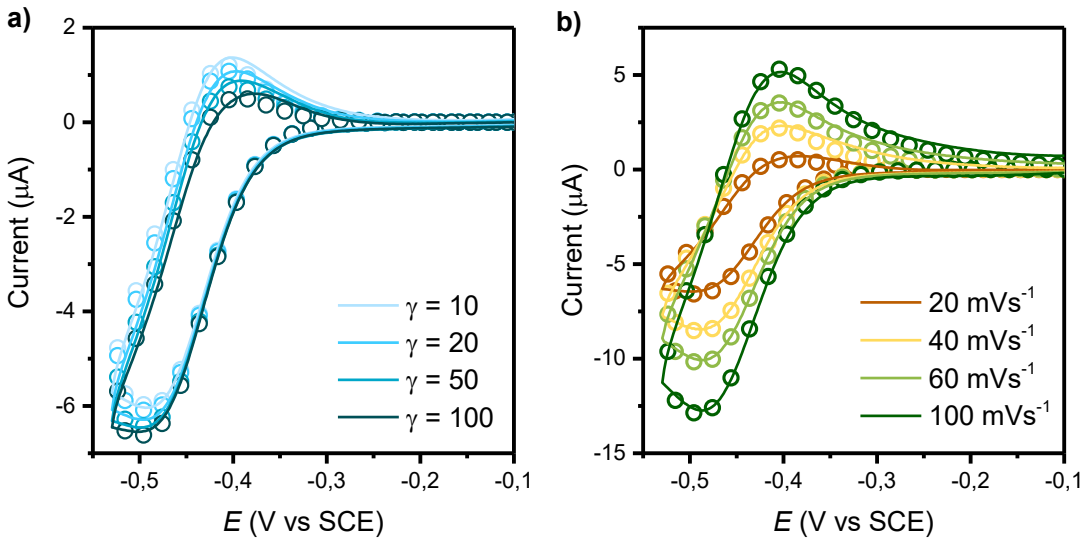

Figure 27. Experimental (full line) and simulated (circles) CVs of a) the PDI + MBiB system under irradiation with the 630 nm LED with increasing substrate concentration; scan rate fixed at 0,02 Vs^{-1}. Concentration of MBiB ranging from 10 mM (γ = 10) to 100 mM (γ = 100). b) CVs of the PDI + MBiB system under irradiation with the 630 nm LED, with γ = 100, and increasing scan rate. Both sets of experimental CVs performed for 1 mM PDI in DMF + 0,1 M n-Bu_4NBF_4 on a GC electrode (A=7,07 mm^2). T = 25 °C.

For each substrate the procedure was repeated identically as described before. Experimental and simulated CVs for all the tested substrates are available Appendix A. The results obtained from the fitting of the experimental data are reported in Table 4. All measured rate constants are very high, almost reaching 10^8 M^{-1} s^{-1}. Despite being very high, these rate constants efficiently compete with the fast decay of *$PDI^{\bullet-}$, which proceeds with rate constant approaching 10^{10} s^{-1}. This is in line with the relatively small current increase observed. We can conclude that *$PDI^{\bullet-}$ can react with RX substrate to generate radical, albeit with relatively low efficiency. This makes it potentially suitable as polymerization initiatioar, since polymerization requires a small but steady supply of radicals.

Table 4. Values of the experimental $k_{cat,I}$ and conditions for various tested substrates.

Entry	Active Catalyst	RX	log($k_{cat,I}$)[a]	D_{RX} (cm^2 s^{-1})[b]	γ[c]
1	*$PDI^{\bullet-}$	MBiB	7,91	1,08 × 10^{-5}	10, 20, 50, 100
2	*$PDI^{\bullet-}$	EBiB	7,78	1,04 × 10^{-5}	10, 20, 50, 100
3	*$PDI^{\bullet-}$	BrACN	7,97	1,24 × 10^{-5}	10, 20, 50, 100

[a] Obtained from data fitting using the software DigiElch. [b] Calculated with the empirical method reported by Valencia and González[141]. [c] γ defined as the ratio of substrate concentration and PDI concentration (C_{RX}/C_{PDI}); all the experiments were performed with C_{PDI} = 1 mM.

3.1.2. Reactivity of excited state dianion catalyst *PDI^{2-}.

The catalytic behavior of the second reduced form of PDI (*PDI^{2-}) has been studied with the substrate methyl 4-chlorobenzoate (MCB). MCB is an aromatic chloride, much less reactive than RX considered up to now. Indeed, as will be discussed below, MCB cannot be reduced at the potential accessible by *PDI$^{\bullet-}$, but only by the excited state dianion *PDI^{2-}, with $E^{\ominus}$ = –2,7 V vs SCE.[134]

The proposed RX reduction mechanism catalyzed by *PDI^{2-} is presented in Scheme 13. Two consecutive reductions of PDI form PDI^{2-}, which is excited under 30 W 630 nm irradiation to form *PDI^{2-}. The cycle is closed by the reaction between the excited state dianion and aryl halide MCB, with stepwise reductive cleavage (SDET) of the carbon chlorine bond. Given the similarity between reactivity of *PDI$^{\bullet-}$ (Scheme 11) and that of *PDI^{2-} (Scheme 13), the same experimental approach was used as the one described above.

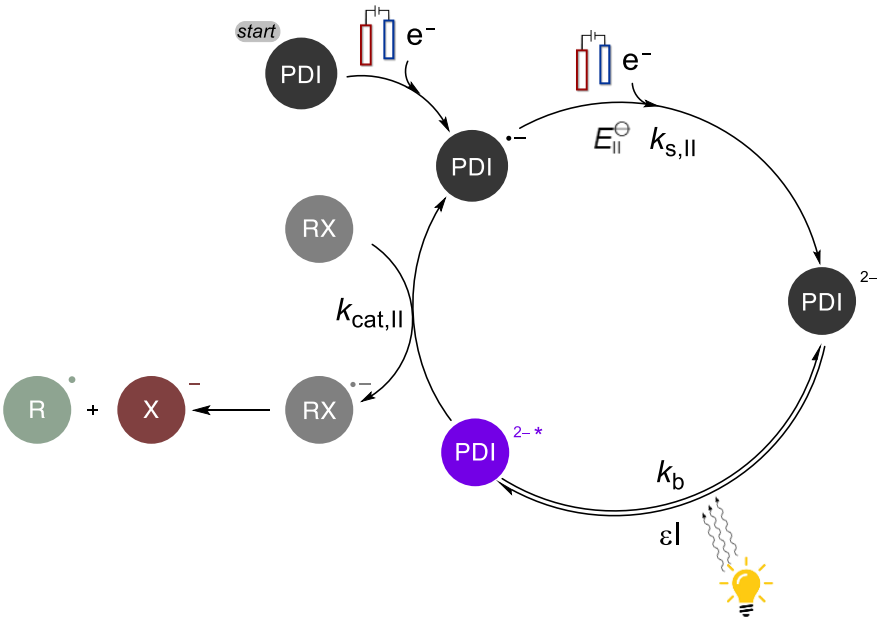

*Scheme 13. Mechanism of electro-photocatalytic reduction of RX involving *PDI^{2-}.*

i) **Study of the electrochemical system in the dark**

The determination of physical quantities for the second reduction of PDI, related to the PDI$^{\bullet-}$/PDI^{2-} couple related to the non-irradiated system are illustrated in the previous section (

Table 2), including $E^{\ominus}$ = −0,75 V vs SCE with k_s = 0,0108 cm s^{-1}.

To be certain that no electrochemical reduction occurred in the absence of light, a series of CVs with increasing γ (C_{MCB}/C_{PDI}) value were performed (Figure 28). Similarly to the case of $PDI^{\bullet-}$, no catalytic current was observed as the ratio $i_{pc}/i_{pc,0}$ remained constant, indicating the absence of any electrocatalysis in the dark.

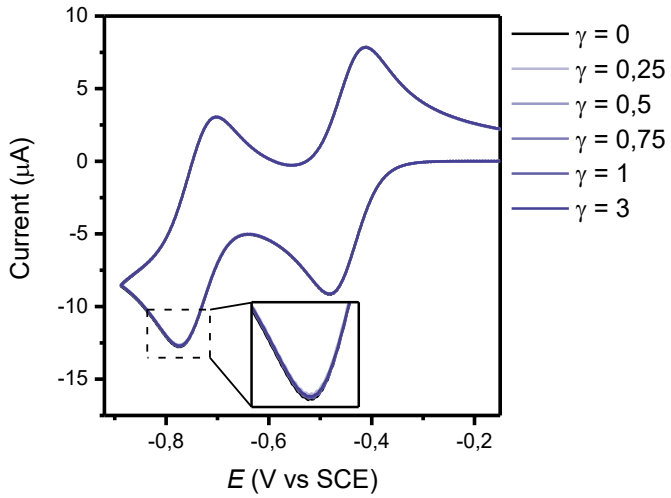

Figure 28. CVs of a PDI (1,0 mM) and MCB. The factor γ represents the concentration ratio between substrate (MCB) and catalyst (PDI). CV performed in DMF + n-Bu_4NBF_4 (0,1 M) on a GC electrode (A = 7,07 mm^2) at T = 25 °C. Scan rate = 0,06 V s^{-1}.

ii) Preparation by bulk electrolysis in dark of the ion radical of the photocatalyst

With a procedure analogous to the one used for $PDI^{\bullet-}$ the absorption spectra (Figure 29a) and molar absorption coefficient of PDI^{2-} were measured.

Excitation rate constant ($k_{\varepsilon I}$) is calculated by the product of ε and I (Figure 29b). The decay rate constant ($k_{b,II}$) of the excited state is calculated as the reciprocal of the lifetime $\tau_0(*PDI^{2-})$ = 6,4 ns[134], $k_{b,II} = 1{,}56\times10^8$ s^{-1}.

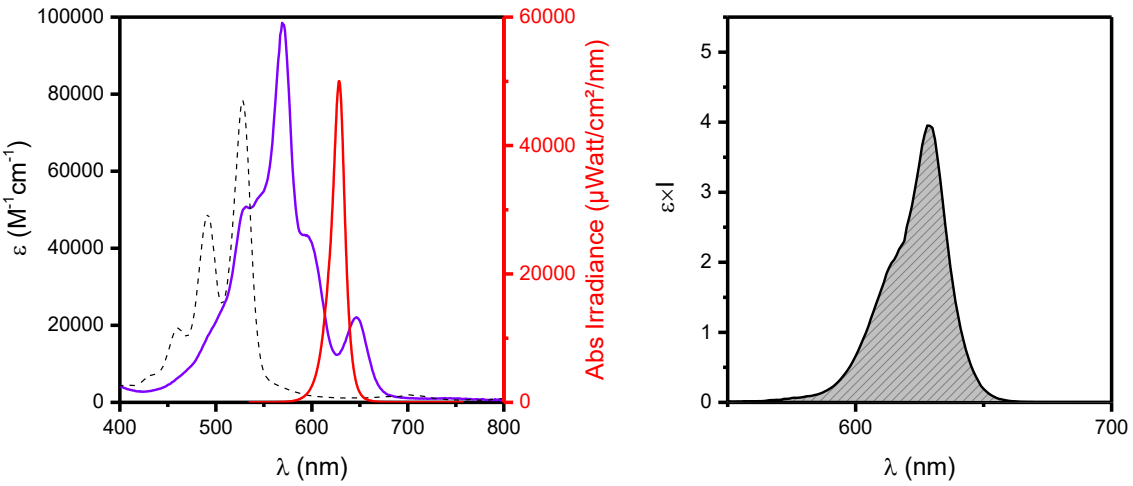

Figure 29. a) Spectra of PDI (dashed line) and PDI^{2-} (purple line) with absolute irradiance of the 630 nm LED. Absorption spectrum of $PDI^{\bullet-}$ acquired via spectroelectrochemistry: reduction in a 0,5 mm cuvette (inert atmosphere) of 0,3 mM PDI in DMF + n-Bu_4NBF_4 (0,1 M) on a Pt WE at a potential of -1,2 V vs SCE. Absolute irradiance measured with an Avantes AvaSpec spectrophotometer. b) Probability of excited state formation calculated as the integral under the εI vs λ curve.

iii) CV analysis of the photocatalyst under irradiation and in the absence of substrate

To evaluate the diffusion coefficient (*D*) and the Nernst diffusion layer thickness (δ), the method presented earlier for $*PDI^{\bullet-}$ was applied. First, CVs of PDI and in the dark under irradiation were recorded (Figure 30a), this time analyzing both volammetric peaks. The results again indicate an increased cathodic current due to enhanced mass transfer under irradiation. Digital simulation of the voltammetric data was used to obtain the values of *D* and δ (Figure 30b).

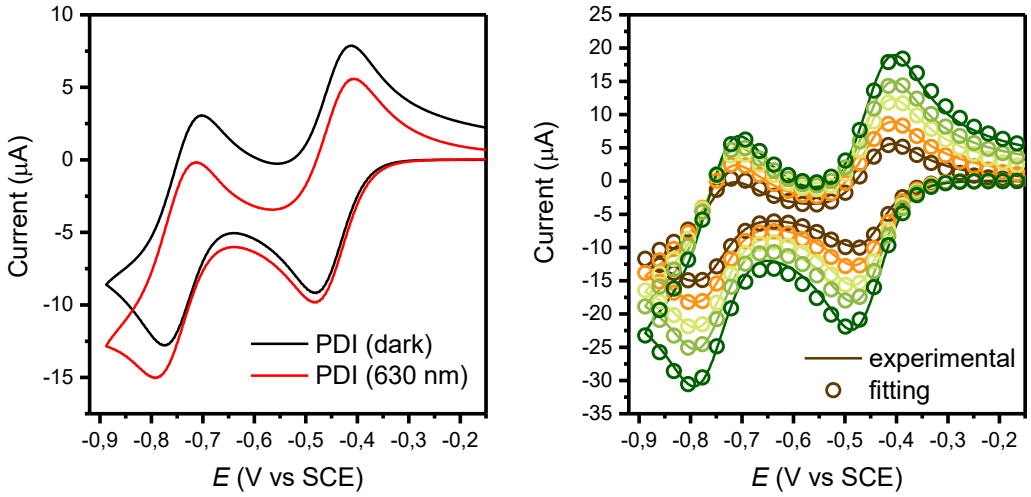

Figure 30. a) Effect of irradiation with a 630 nm LED on a solution of 1,0 mM PDI. Scan rate = 0,06 V s^{-1} b) experimentally obtained CVs of 1,0 mM PDI under irradiation at different scan rates (full lines) with respective simulated data (circles). All the CVs are performed in DMF + n-Bu_4NBF_4 (0,1 M) on a GC electrode (A = 7,07 mm^2) at T = 25 °C.

The diffusion coefficient obtained from simulated data was the same as the one recorded for $PDI^{\bullet-}$. The Nernst diffusion layer (δ) under irradiation was found to be 82 µm, slightly larger than the one observed for the smaller voltametric window of $PDI^{\bullet-}$ (75 µm).

iv) CV analysis under irradiation and in the presence of the substrate

CV analysis of PDI under irradiation showed a marked difference in the absence and in the presence of MCB. No sign of catalysis was observed in correspondence to the first peak, indicating that $*PDI^{\bullet-}$ was not an effective catalyst for MCB reduction. Instead, a massive increase in cathodic current was observed in correspondence with the second reduction peak, indicating that $*PDI^{2-}$ was an extremely effective catalyst for the reduction of MCB. Correspondingly, a substantial drop in anodic currents was observed. As expected, the current enhancement increased with MCB concentration (γ from 0,25 to 3).

The large increase in catalytic activity of $*PDI^{2-}$ compared to that of $*PDI^{\bullet-}$ can be ascribed to its longer lifetime and more negative reduction potential. The light absorption of PDI^{2-} and $PDI^{\bullet-}$ was comparable instead. The much higher reactivity of $*PDI^{2-}$ was also observed in the literature[134].

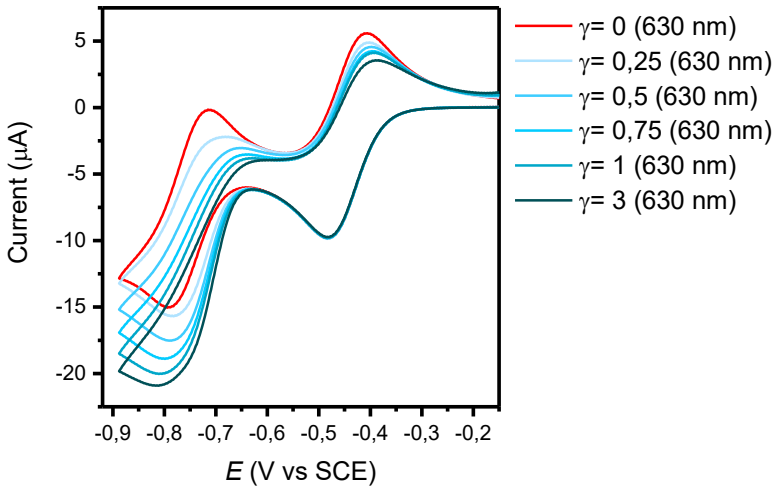

Figure 31. CV under irradiation (630 nm) of 1,0 mM PDI with increasing concentration of MCB. CVs are performed in DMF + 0,1 M n-Bu$_4$NBF$_4$ on a GC electrode (A = 7,07 mm^2) at T = 25 °C. Scan rate = 0,06 V s^{-1}.

For the evaluation of $k_{cat,II}$ in the case of $*PDI^{2-}$ a similar approach to the one used for the $*PDI^{\bullet-}$ catalyzed reduction mechanism was used. The main difference is the inclusion of two subsequent electron transfer events in the mechanism (equations 3.1.1 and 3.1.2), as indicated in Scheme 13.

In addition to that, given the stepwise nature of the bond cleavage mechanism for aryl halides, we considered the competition between back electron transfer from $RX^{\bullet-}$ (k_{-ET}) and intramolecular

cleavage of the carbon halogen bond (k_{intra}). In this context, the considered mechanism for the homogeneous dissociative electron transfer is reported in Scheme 14.

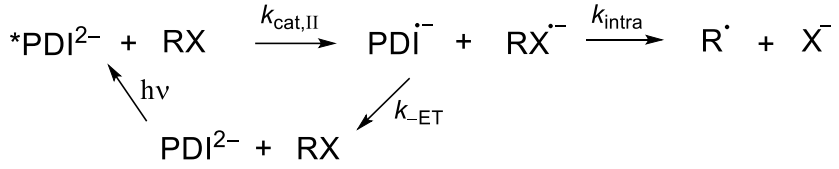

*Scheme 14. Complete description of the stepwise bond cleavage for the aryl halide catalyzed by *PDI²⁻.*

The value of k_{-ET} was set equal to the diffusion-controlled rate constant[142]. The value of k_{intra} was taken from the literature[142].

All the considered reactions and their respective rate coefficients are listed as follows:

$^*PDI^{2-} + RX \rightarrow PDI + R^\bullet + X^-$	$k_{cat,II}$ (M^{-1} s^{-1})	*fitted*	(3.1.19)
$PDI + e^- \rightarrow PDI^{\bullet-}$	$k_{s,I}$ (cm s^{-1})	0,0108	(3.1.1)
$PDI^{\bullet-} + e^- \rightarrow PDI^{2-}$	$k_{s,II}$ (cm s^{-1})	0,0108	(3.1.2)
$PDI^{\bullet-} + h\nu \rightarrow {}^*PDI^{\bullet-}$	$k_{\varepsilon I,I}$ (s^{-1})	73,57	(3.1.5)
$PDI^{2-} + h\nu \rightarrow {}^*PDI^{2-}$	$k_{\varepsilon I,II}$ (s^{-1})	86,48	(3.1.20)
$^*PDI^{\bullet-} \rightarrow PDI^{\bullet-}$	$k_{b,I}$ (s^{-1})	$6{,}25 \times 10^9$	(3.1.17)
$^*PDI^{2-} \rightarrow PDI^{2-}$	$k_{b,II}$ (s^{-1})	$1{,}56 \times 10^8$	(3.1.21)
$PDI^{\bullet-} + R^\bullet \rightarrow PDI - R^-$	k_c (M^{-1} s^{-1})	10^9	(3.1.12)
$R^\bullet + R^\bullet \rightarrow RR$	$k_{c'}$ (M^{-1} s^{-1})	10^9	(3.1.18)
$RX^{\bullet-} + PDI^{\bullet-} \rightarrow PDI^{2-} + RX$	k_{-ET} (M^{-1} s^{-1})	$1{,}07 \times 10^{10}$	(3.1.22)
$RX^{\bullet-} \rightarrow R^\bullet + X^-$	k_{intra} (s^{-1})	$1{,}3 \times 10^7$	(3.1.23)
$PDI^{\bullet-} + R^\bullet \rightarrow PDI + R^-$	$k_{ET,I}$ (M^{-1} s^{-1})	$4{,}4 \times 10^7$	(3.1.13)
$PDI^{2-} + R^\bullet \rightarrow PDI^{\bullet-} + R^-$	$k_{ET,II}$ (M^{-1} s^{-1})	$8{,}5 \times 10^8$	(3.1.24)
$^*PDI^{\bullet-} + R^\bullet \rightarrow PDI + R^-$	$k_{ET^*,I}$ (M^{-1} s^{-1})	$>k_d$	(3.1.25)
$^*PDI^{2-} + R^\bullet \rightarrow PDI^{\bullet-} + R^-$	$k_{ET^*,II}$ (M^{-1} s^{-1})	$1{,}8 \times 10^4$	(3.1.26)

In this case the $k_{ET,II}$ was determined by fitting of the experimental CVs (Figure 32). A good match between experimental and simulated CVs was obtained, with a very high value $\log(k_{cat,II}) = 9{,}80$. The

value is reported in Table 4 together with other details, and is fully consistent with the high reactivity of this catalyst. Comparison with theoretical and independently measured values of $\log(k_{cat,II})$ is presented in the next section.

Table 5. Value of $k_{cat,II}$ obtained from simulation

Entry	Active Catalyst	RX	$\log(k_{cat,II})$[a]	D_{RX} ($cm^2\ s^{-1}$)[b]	γ[c]
1	$*PDI^{2-}$	MCB	9,80	$1{,}10 \times 10^{-5}$	0,25, 0,5, 1, 2, 3, 4

[a] Obtained from data fitting using the software DigiElch. The reported value is the result of an average between two separate experiments, one consisting in the evaluation of 15 CVs and the other where over 25 CVs were analyzed; the standard error associated with the collected data is ± 0,73. [b] Calculated with the empirical method reported by Valencia and González[141]. [c] γ defined as the ratio of substrate concentration and PDI concentration (C_{RX}/C_{PDI}); all the experiments were performed with C_{PDI} = 1 mM.

Some reactions included in the overall mechanism are commented here. As observed previously, the reduction of the radical species $R^{\bullet}$ by the excited-state catalysts ($*PDI^{\bullet-}$ and $*PDI^{2-}$) does not significantly impact the system. The reduction by $*PDI^{\bullet-}$ proceeds at the diffusion-limited rate constant (k_d) once again. Conversely, the reduction by $*PDI^{2-}$ proceeds at a low rate, likely due to the high driving force ($\Delta G^0 = -184$ kJ mol^{-1}), placing it in the inverted region.

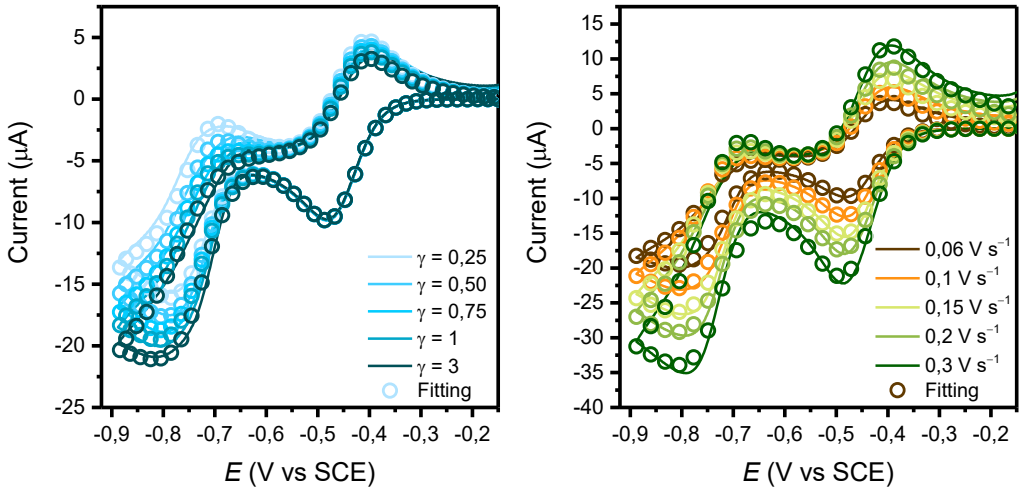

Figure 32. Experimental (full line) and simulated (circles) CVs of a) the PDI + MCB system under irradiation with the 630 nm LED with increasing substrate concentration; scan rate fixed at 0,06 V s^{-1}. Concentration of MCB ranging from 0,25 mM (γ = 0,25) to 3 mM (γ = 3). b) CVs of the PDI + MCB system under irradiation with the 630 nm LED, with γ = 1, and increasing scan rate. Both sets of experimental CVs performed on a solution of 1,0 mM PDI in DMF + 0,1 M n-Bu_4NBF_4 on a GC electrode (A=7,07 mm^2). T = 25 °C.

3.2. Comparison of the CV method with theoretical and experimental k_{cat} data

To validate and cross-check the experimental data obtained via the CV method, they were compared with theoretical predictions from Marcus-Savéant OSET theory and with values derived from time-correlated single-photon counting (TCSPC), an established photochemical method.

3.2.1. Comparison with theoretical values from Marcus-Savéant OSET theory

Marcus-Hush electron transfer (ET) theory is a powerful tool that allowed us to effectively predict the kinetics of ET processes (k_{ET}). The model approaches the ET issue considering the interaction between an electron donor (D) and an electron acceptor (A). The two species can react in two different ways, following a so-called outer sphere electron transfer (OSET) process or an inner sphere electron transfer (ISET) process. The first hypothesizes that ET occurs with little to no overlap between the wavefunctions of D and A, while the latter considers the formation of a strong link between donor and acceptor (*e.g.* covalent or metal-ligand bonding) after which the ET can happen. In other words, the ET can be intermolecular or intramolecular.

J.M. Savéant extended the Marcus model to the field of dissociative electron transfer (DET). Carbon halogen bonds are subjected to bond rupture when injected with an electron, fitting under the vast umbrella of DET reactions.

Savéant defined a spectrum of reactivity in which the defining mechanisms are (i) Concerted DET (CDET), (ii) Stepwise DET (SDET) and (iii) "Sticky" DET.

The competition between CDET and SDET pathways depends upon intramolecular (structural and electronic) and environmental (solvent and energy of the incoming electron) factors. The mechanism is influenced the most by: (i) the bond dissociation energy of the substrate (D_{RX}), (ii) its standard reduction potential ($E^{\ominus}_{RX/RX^{\bullet -}}$ or $E^{\ominus}_{RX/R^{\bullet}+X^{-}}$) (iii) and the standard oxidation potential of the leaving group X^- ($E^{\ominus}_{X^{\bullet}/X^{-}}$).[127]

A general distinction can be made between aryl and alkyl halides. In aryl halides, the halogen is directly attached to the aromatic system, allowing the incoming electron to be accommodated on a low energy π* orbital. As a result, aryl halides typically follow a SDET mechanism. The incoming electron can resonate for a few bond vibrations withing the π* orbital before bond breaking occurs. Conversely, in alkyl halides, the first available orbital is σ*, making the cleavage of the C–X bond more energetically favorable than the formation of a species with one electron in a σ* orbital, thus following a CDET mechanism: the bond cleavage is concerted with the electron transfer.

The reduction of substrates tested in this work should all follow an OSET mechanism, being unable to form a strong linkage with the reducing agent (large aromatic molecules such as $*PDI^{\bullet-}$ or $*PDI^{2-}$).

The general workflow adapted in a typical analysis via Marcus theory can be schematized in the following diagram.

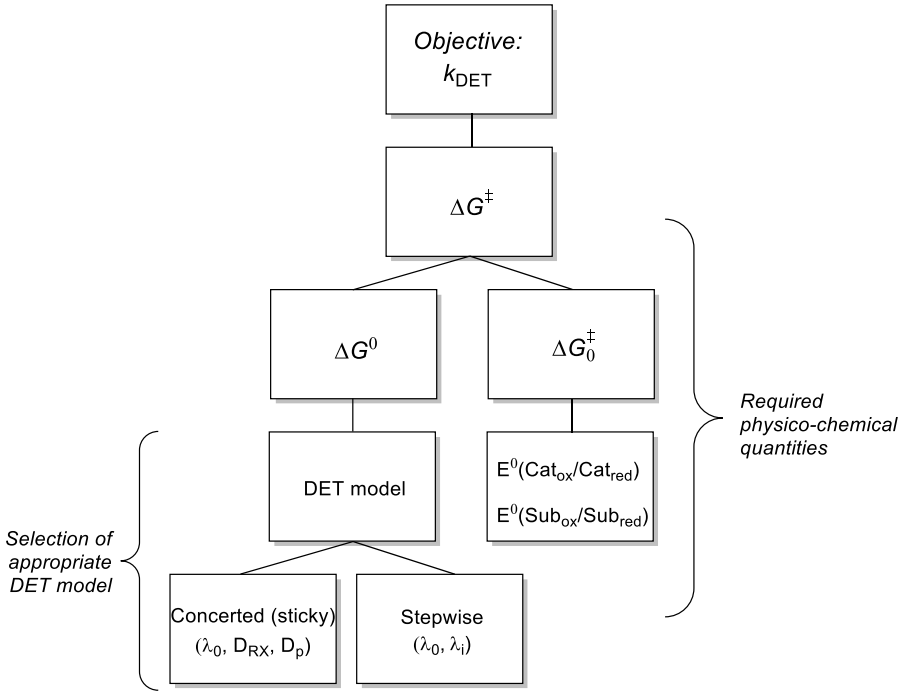

The generic overall reaction can be described as:

$$\mathrm{Cat_{Red}} + \mathrm{RX} \xrightarrow{k_{\mathrm{DET}}} \mathrm{Cat_{Ox}} + \mathrm{R^{\bullet}} + \mathrm{X^{-}} \tag{3.2.1}$$

The k_{DET} for the catalytic reduction of substrate is described by equation (3.2.3).

$$k_{\mathrm{DET}} = Z\mathrm{e}^{-\frac{\Delta G^{\ddagger}}{RT}} \tag{3.2.2}$$

where Z is the preexponential factor and $\Delta G^{\ddagger}$ is the activation free energy.

Z is obtained by the collision theory and is defined in equation (3.2.3) while $\Delta G^{\ddagger}$ is calculated as in equation (3.2.4) for both CDET and SDET and in equation (3.2.5) for the sticky CDET mechanism. In the sticky CDET pathway, the interaction between the two fragments $R^{\bullet}$ and X^{-} in the solvent cage has been considered. The interaction between the fragments induces a modification in the Morse curve model which describes the process, so that the curve potential considers the charge-(induced)dipole interaction between $R^{\bullet}$ and X^{-}. The validity of the DET model remains intact with the introduction of the quantity D_p, describing the energy of the interaction between the caged fragments. For the studied halides, the D_p was considered even if it is generally small in polar solvents (such as DMF).

$$Z = N_A \sqrt{\frac{8\pi RT}{\mu}} (r_{Cat} + r_{RX})^2 \quad (3.2.3)$$

$$\Delta G^{\ddagger} = \Delta G_0^{\ddagger} \left(1 + \frac{\Delta G^0}{4\Delta G_0^{\ddagger}}\right)^2 \quad (3.2.4)$$

$$\Delta G^{\ddagger} = \Delta G_0^{\ddagger} \left(1 + \frac{\Delta G^0 - D_p}{4\Delta G_0^{\ddagger}}\right)^2 \quad (3.2.5)$$

In our specific case, the sticky CDET model has been applied to approach the concerted cleavage of C−X bonds in alkyl halides and calculated its k_{ET}. Instead, for MCB being an aryl halide, the SDET mechanism was applied.

The main factors at play in the calculations of k_{ET} are the reaction free energy constant ΔG^0, the intrinsic barrier of the process $\Delta G_0^{\ddagger}$ and the reorganization energy λ. Formally, $\Delta G_0^{\ddagger}$ is the activation free energy when $\Delta G^0 = 0$.

The intrinsic barrier $\Delta G_0^{\ddagger}$ is defined in equation (3.2.6) for sticky CDET pathways and in (3.2.7) for SDET mechanisms:

$$\Delta G_0^{\ddagger} = \frac{\left(\sqrt{D_{RX}} - \sqrt{D_p}\right)^2 + \lambda_o}{4} \quad (3.2.6)$$

$$\Delta G_0^{\ddagger} = \frac{\lambda_i + \lambda_o}{4} \quad (3.2.7)$$

The bond dissociation energy can be calculated using thermodynamic cycles and DFT calculations[143]. The solvent reorganization energy λ_0 is obtained with the empirical equation (3.2.8)[144,145]:

$$\lambda_0 (\text{kJ mol}^{-1}) = 99 \left(\frac{1}{2r_{Cat}} + \frac{1}{2r} - \frac{1}{r_{cat} + r}\right) \quad (3.2.8)$$

In which r_{Cat} is calculated using the Stokes-Einstein equation and r is defined as $r=(2r_{RX} - r_X)r_X/r_{RX}$.[146,147] using r_{Br} = 1.96 Å, r_{Cl} = 1.81 Å[148] together with r_{RX} defined as spherical radius, as in equation (3.2.9).

$$r_{RX} = \frac{3}{4}\left(\frac{MW_{RX}}{N_A\, \rho\pi}\right)^{\frac{1}{3}} \quad (3.2.9)$$

With the formalism since now described a series of rate constants for the e-PRC reduction of the substrates (Table 6).

Table 6. Comparison between experimental k_{cat} values and rate constant values calculated with the Marcus-Savéant OSET theory.

Entry	Active Catalyst	RX	Model used	$\Delta G^{0\,a}$ (kJ mol^{-1})	$\Delta G_0^{\ddagger\,a}$ (kJ mol^{-1})	$D_p{}^b$ (kJ mol^{-1})	log($k_{cat,th}$)	log($k_{cat,exp}$)
1	*PDI$^{\bullet-}$	MBiB	CDET	−118,7	68,3	2,22	8,26	7,99
2	*PDI$^{\bullet-}$	EBiB	CDET	−118,7	67,9	2,22	8,29	7,75
3	*PDI$^{\bullet-}$	BrACN	CDET	−133,1	71,4	0,675	8,44	8,05
4	*PDI^{2-}	MCB	SDET	−65,6	15,8	/	10,99 [c]	9,80

[a] Values predicted according to DET theory [b] Taken from [149] (Entry 1 and 2) and from [150](Entry 3) [c] The value exceeds the diffusion-limited rate constant (k_d = 1,07 × 10^{10} M^{-1} s^{-1}, logk_d = 10,03)

The experimental values for the *PDI$^{\bullet-}$ catalyzed reactions are close to the theoretical one, deviating by a maximum of 0,6 logarithmic points. Considering the approximations made for the theoretical calculations the results are in satisfactory accordance with the experimental values.

Next, we compared the log($k_{cat,exp}$) values obtained by CV simulation with independently measured experimental values. Since the lifetime of *PDI$^{\bullet-}$ was too short, only the *PDI^{2-} system was further considered.

3.2.2. Comparison with TCSPC measurements

To obtain an additional experimental value to test the validity of our CV method, the value of $k_{cat,II}$ for the reaction between *PDI^{2-} and MCB was directly measured using a well-established optical method, time-correlated single-photon counting (TCSPC).

Photochemical systems are widely studied using optical methods. To study excited state reactivity transient absorption spectroscopy (TAS) and time-correlated single-photon counting (TCSPC) are used. TAS uses high speed laser pulses to excite samples and record a variation in optical density, which can correlate with reactivity information. TCSPC is the method of choice for quantifying the fluorescence lifetimes; it records the time between an excitation pulse and a single emitted photon.

The main difference between the two methods is that the latter has restrictions in the lower limit of the time domain. It is not possible to measure lifetimes of species that go below nanoseconds. Therefore, TCSPC cannot by applied to study the reactivity of *PDI^{-}, which has a lifetime of only 160 ps and does not exhibit florescence. Instead, it is possible to perform TCSPC measures on *PDI^{2-} since

it exhibits fluorescence and has a lifetime of 6,4 ns. A comparison between absorption and emission spectra of PDI^{2-} is reported in Figure 33.

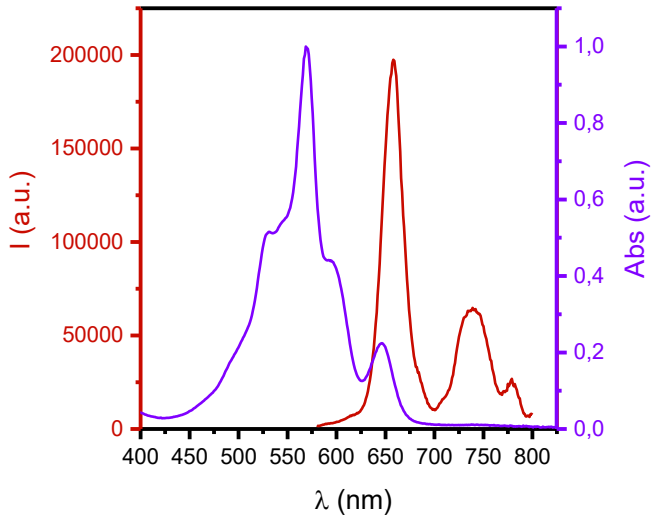

Figure 33. Emission (red) and absorption (purple) spectra of PDI^{2-}.

The steady-state emission measurements were conducted using a 450 W Xenon Arc lamp. To perform TCPSC measurements pulsed diode laser at 635 nm as excitation source and the emission was recorded at 657 nm; we used a 20MHz sampling frequency.

Using techniques that quantify the fluorescence opens to the possibility of measuring reaction rate constants. This is possible by exponential fitting the variation of the fluorescence decay in presence of a quencher (a substrate that can react with the molecule of interest, in our case MCB).

A series of fluorescence decay measurements of $*PDI^{2-}$ in the presence of increasing amounts of MCB were carried out (Figure 34a) and fitted to obtain the lifetime of the excited state, according to a single exponential equation (3.2.10).

$$I(t) = Be^{-\frac{t}{\tau}} \qquad (3.2.10)$$

Where I is the fluorescence intensity.

For $*PDI^{2-}$ alone, a lifetime of 5,88 ns was measured, which is consistent the value reported in the literature[134], considering the non-exhaustive degassing of the cuvette. The lifetime sharply decreased in the presence of increasing amounts of MCB, indicating that the two were reacting.

From the Stern-Volmer diagram (Figure 34b) it is possible to obtain the reaction rate constant relative to the excited state quenching by the substrate (k_q). The measures were performed on

electrochemically generated PDI^{2-} (carefully kept away from oxygen and from irradiation sources) to which aliquots of MCB were added before transferring it into a 1 mm fluorescence cuvette for the analysis.

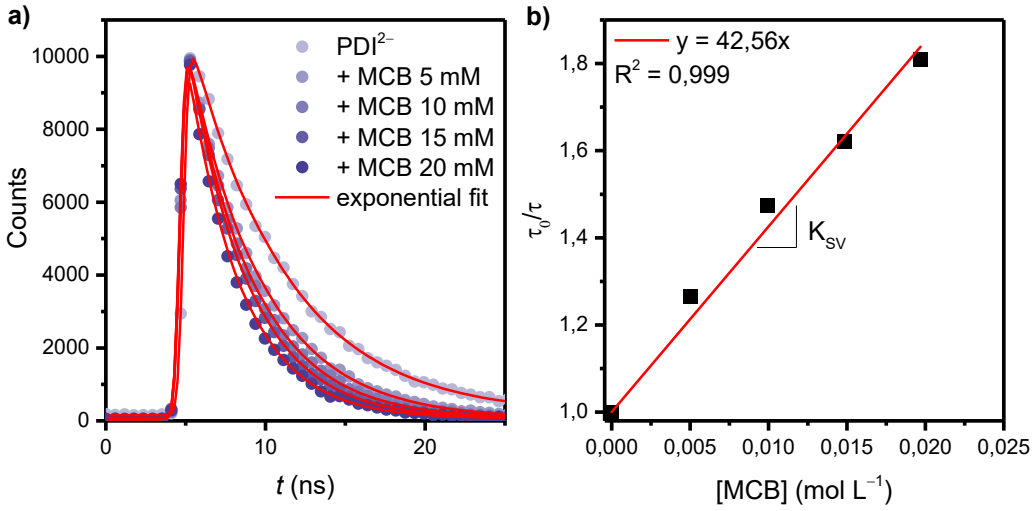

*Figure 34. a) Fluorescence decay of *PDI^{2-} in the absence and in the presence of MCB (purple) with exponential fitting (red line). b) Stern-Volmer diagram. Linear fitting in red.*

The data were then elaborated to obtain the quenching rate constant (k_q) from the Stern-Volmer constant (K_{SV}), using the relationship:

$$\frac{\tau_0}{\tau} = 1 + K_{SV}[Q] = 1 + k_q\tau_0[Q] \qquad (3.2.11)$$

where τ_0 and τ are the excited state lifetimes measured in absence and in presence of a quencher (Q), respectively. K_{SV} is obtained experimentally from the Stern-Volmer plot. [Q] indicates the concentration of quencher in mol L^{-1}. In this specific case the quencher, Q, is MCB.

The k_q from fluorescence decay experiments is compared with rate constants from CV simulation and theoretical analysis (Table 7). The TCSPC data aligns closely with CV analysis, showing strong agreement despite methodological differences. Specifically, the simulated $k_{cat,II}$ and quenching rate constants differ by only 0.04 logarithmically, validating the CV method and establishing a precedent for direct comparison with TCSPC analysis.

Table 7. The value of k_q and and comparison with other rate constant values obtained with other methods.

Entry	Active Catalyst	RX	$\log(k_q)^a$	$\log(k_{cat,II})^b$	$\log(k_{cat,th})^c$
1	*PDI^{2-}	MCB	9,84	9,80	10,99 ($\log k_d$ = 10,03)

[a] Obtained from fluorescence decay experiment performed on electrochemically generated PDI^{2-}. [b] Obtained from experimental data fitting using the software DigiElch. [c] Calculated using the Marcus OSET theory.

3.3. Applications of e-PRC in RDRP polymerizations

In the previous sections, the catalytic activity of $PDI^{\bullet-}$ and PDI^{2-} towards reductive cleavage of C–X bonds was tested and quantified. As discussed in Chapter 1, the ability to generate radicals via DET opens numerous possibilities for subsequent reactivity. Radical chemistry involving RX is particularly significant in polymer science. Our focus is on applying an activated photocatalyst in an RDRP process, with the goal of efficiently integrating PDI into RDRP catalytic cycles. To achieve this, two main pathways have been investigated, two-photon ATRP and electrophotocatalyzed RAFT polymerization.

3.3.1. Two-Photon ATRP

The first approach explores implementing a two-photon process in an ATRP-like polymerization using PDI reactivity. Our studies on RX activators indicated that a catalytic effect is possible and reproducible to generate radicals through DET. To achieve this type of reactivity, a process was hypothesized based on recent literature, as described in Figure 35.

First PDI photoexcited to *PDI under irradiation with a 456 nm Kessil Lamp. Second, the photoexcited species reacts with an electron donating amine (triethylamine, TEA) to form $PDI^{\bullet-}$ and the amine radical cation ($TEA^{\bullet+}$). The anion radical is then excited to its doublet state ($*PDI^{\bullet-}$) under the 456 nm light. To close the cycle, $*PDI^{\bullet-}$ can reduce the initiator (RX), with irreversible cleavage of the carbon-halogen bond forming the $R^{\bullet}$ propagating radical which is the relevant species in the polymerization process; this is the activation step ruled by its specific rate law (k_{act}). The propagating radicals should enter a dynamic activation-deactivation equilibrium where the active species return to a dormant state upon reaction with $TEA^{\bullet+}$; this corresponds to the deactivation step, ruled by its rate constant (k_{deact}).

For successful ATRP polymerization and control over the polymer's molecular weight distribution, it is essential that the deactivation rate (k_{deact}) is high and faster than the activation rate (k_{act}). The activation process was studied and deemed effective in the previous section, and the deactivation process will be investigated via polymerization experiments as discussed below.

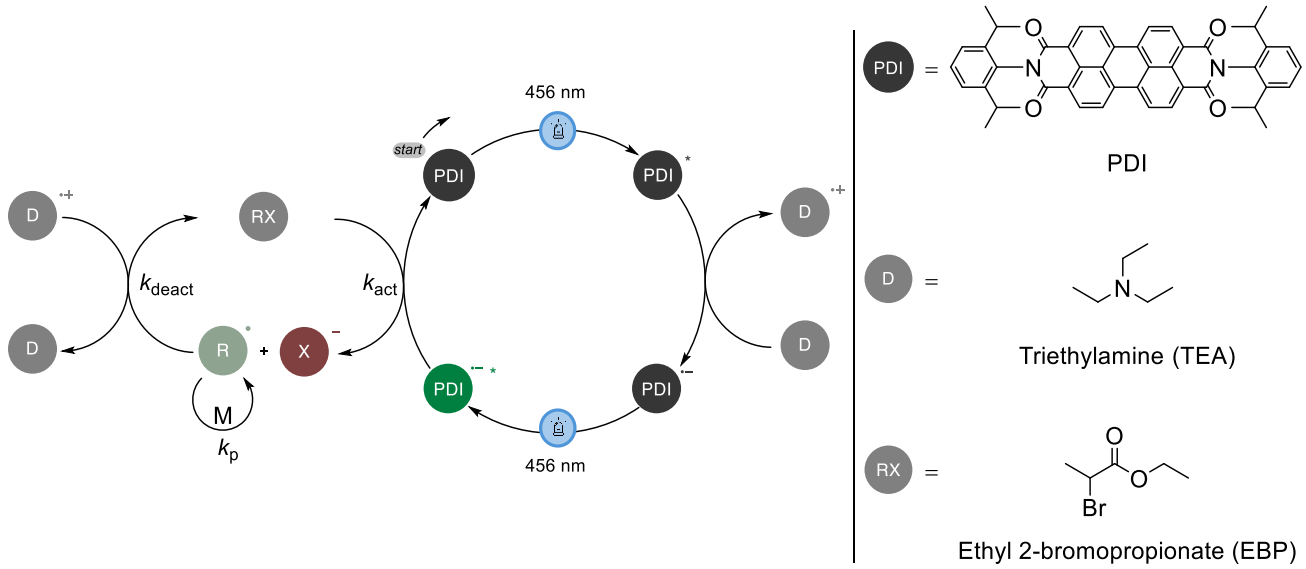

Figure 35. Mechanism of the two photon ATRP process (left) and structures of PDI, electron donating species D, used ATRP activator RX (right).

A standardized procedure was followed to carry out the polymerization: a vial equipped with a magnetic stir bar and capped with a greased glass cap was charged with methyl methacrylate (1,07 mL, 100 equiv.), initiator (1 equiv.), triethylamine (5 equiv.), PDI (0,01 equiv.) in DMF (2 mL); the reaction mixture was degassed with four freeze pump-thaw cycles after which the vial was backfilled with argon; the reaction was irradiated for 6h in front of a 456 nm Kessil Lamp under vigorous stirring. Despite effective radical generation and activation, evidenced by the calculated conversion, the polymerization exhibited no control over the molecular weight distribution, indicating that the deactivation step was inefficient.

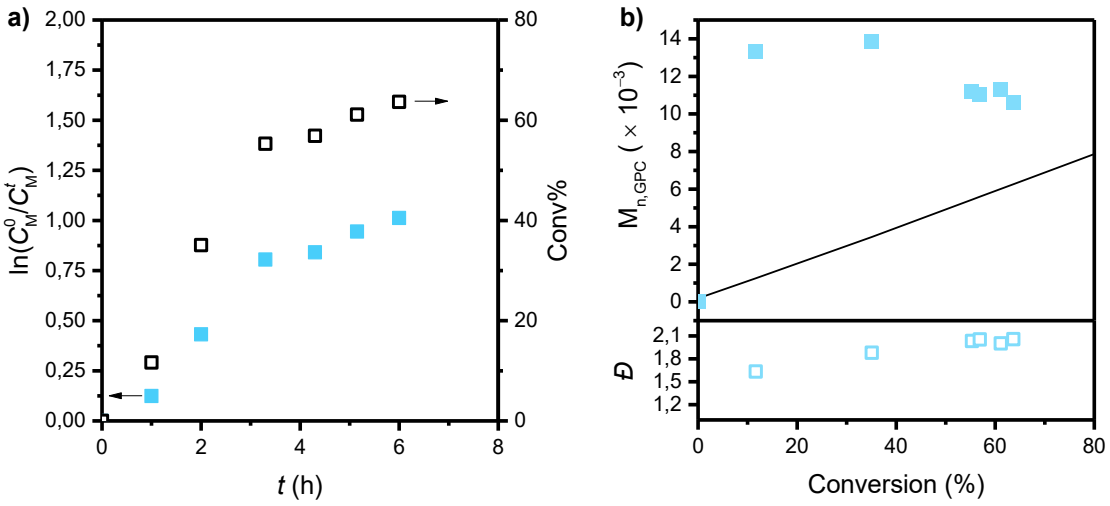

Figure 36. a) Kinetics of the two-photo ATRP process. The kinetics exhibit an initial rapid increase during the first 3 hours, followed by a deceleration. However, this pattern remains generally consistent with RDRP behavior and does not deviate significantly from the expected characteristics. b) The graphs show both experimental and theoretical (solid line) average molar weights and dispersity. The

experimental molar weight's non-linear behavior, along with the high dispersity values (>1.8), indicates poor control over the polymerization. This behavior is more consistent with a free radical mechanism than with a controlled one.

Reaction conditions are shown in Table 1. Other conditions and initiators were tested (Appendix C), obtaining in each case similar results and never observing controlled polymerization.

Table 8. Two photon ATRP [a]

Entry	[MMA]:[RX]:[PDI]	RX	Conv [b] (%)	$M_{n,th}$ [c]	$M_{n,GPC}$ [d]	$M_{w,GPC}$ [d]	$Đ$ [d]	I* [e] (%)
1	100:1:0,01	EBP	63,7	6440	10500	21800	2,06	59,1

[a] Conditions: 2,5 mL of solvent (DMF) + 2,5 mL of MMA; degassing by FPT cycles; irradiation with a Kessil 456 nm LED at 5 cm distance and 100% intensity; room temperature. [b] Calculated after 6h via ^{1}H NMR (400 Mhz). [c] Calculated as Conv×MW_{MMA}× $[MMA]_0/[RX]$ + MW_{RX} Determined after 7h by Gel Permeation Chromatography in DMF (PMMA standard, 60°C). [e] $I^*=(M_{n,th}/M_{n,GPC})$ ×100.

A plausible hypothesis for the ineffective deactivation is that the extreme acidity of $TEA^{\bullet+}$ causes it to engage in side reactions (e.g., hydrogen atom transfer, β-scission) rather than deactivating the propagating radical[151].

Overall, this experiment proved the reactivity of $*PDI^{\bullet-}$ in generating radicals, in agreement with our proposed catalytic schemes (Scheme 11 and Scheme 15) and the observed reactivity in CV experiments. However, the poor polymerization control indicated the absence of an efficient radical deactivation pathway.

3.3.2. PET-eRAFT polymerizations

PDI reactivity was successfully integrated to initiate polymerization in an ATRP system, nevertheless, an effective deactivation pathway was lacking. To overcome this limitation, we utilized PDI in a different system in which a reliable deactivation pathway was present. To achieve this, PDI was integrated into a RAFT polymerization process. In this way the control over the polymerization process is guaranteed by the chain transfer agent (CTA).

To test the mechanism and the reactivity of the system, the selected reactants are 4-Cyano-4-[(dodecylsulfanylthiocarbonyl)sulfanyl]pentanoic acid (CDTPA) as the chain transfer agent and methyl methacrylate (MMA) as the monomer (Figure 37).

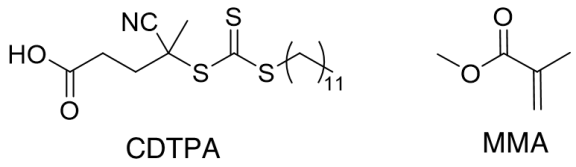

Figure 37. Structures of CDTPA and MMA.

CV was utilized to probe whether a CTA could be activated by the PDI system. Similarly to what was observed with the CV analysis of catalytic cleavage of RX, there's a significant increase in the peak current in presence of CDTPA. Both $*PDI^{\bullet-}$ (Figure 38a) and $*PDI^{2-}$ (Figure 38b) show reducing ability towards CDTPA and in similar fashion to what already observed the dianion exhibits a greater catalytic effect. Therefore, the PDI system showed promising reactivity to mediate a RAFT polymerization via e-PRC mechanism.

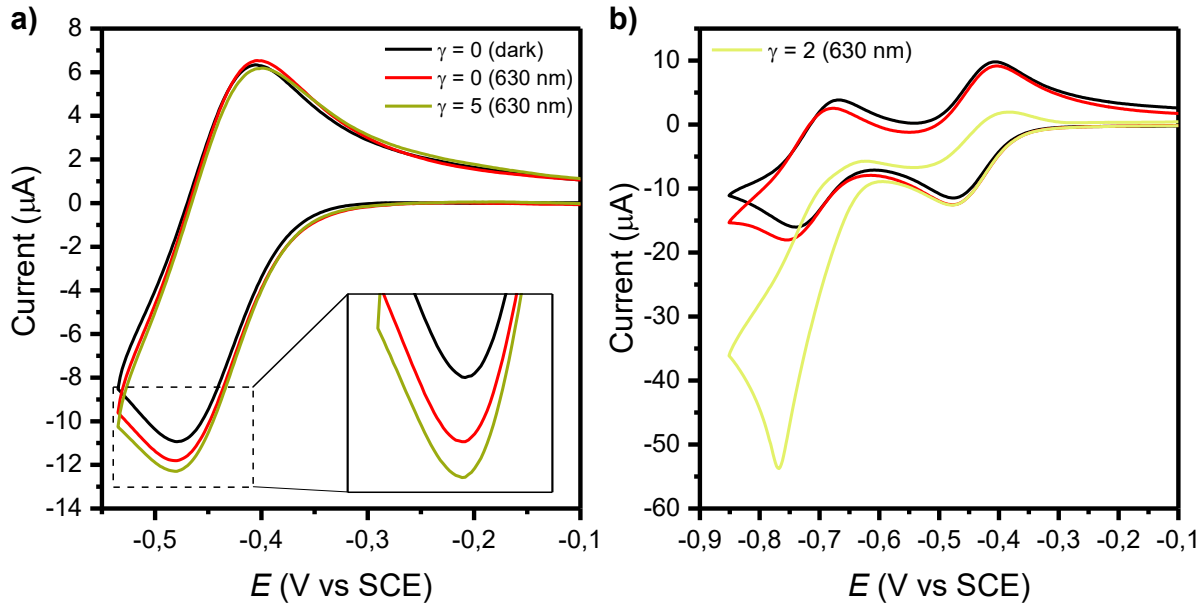

Figure 38. a) CV of PDI (1 mM) in dark, under irradiation with a 630 nm LED, and in presence of CDTPA (5 mM). In the inlet an enlargement of the cathodic peaks to highlight the catalytic current generated in presence of CDTPA. b) CV of PDI (1 mM) in dark, under irradiation with a 630 nm LED, and in presence of CDTPA (2 mM), with a lower inversion potential with respect to a. Both performed in DMF + 0.1 M n-Bu_4NBF_4 on a GC electrode (A = 7,07 mm^2) at T = 35 °C. Scan rate = 0,1 V^{-1}.

In such a system, PDI in its excited state reduced form ($*PDI^{\bullet-}$) should cleave the C–S bond of the RAFT agent to initiate the polymerization. It should be noted that in this case, using blue visible light would have interfered with the reaction process, since it is known that CTAs can absorb radiation in that portion of the spectrum to give photo-iniferter RAFT polymerization[116]. Therefore, light with longer wavelengths (lower energy) was used for all our experiments.

Given the impossibility to use a two-photon process to generate the anion radical, we implemented an electrochemical step, introducing a mechanism like the one implemented to perform cyclic voltammetry analysis, as described earlier (section 3.3.1).

Going back to the reaction mechanism, the electrochemical step followed by a photochemical reaction result in what substantially is an e-PRC polymerization. In RAFT polymerization terms, what follows is the merger of PET-RAFT, in which the catalytic effect is achieved through excitation of a photocatalyst, and mediated *e*RAFT, where the active species to initiate the reaction are produced and regenerated at the electrode. The proposed technique was hence named PET-*e*RAFT, and it is schematized below (Scheme 15).

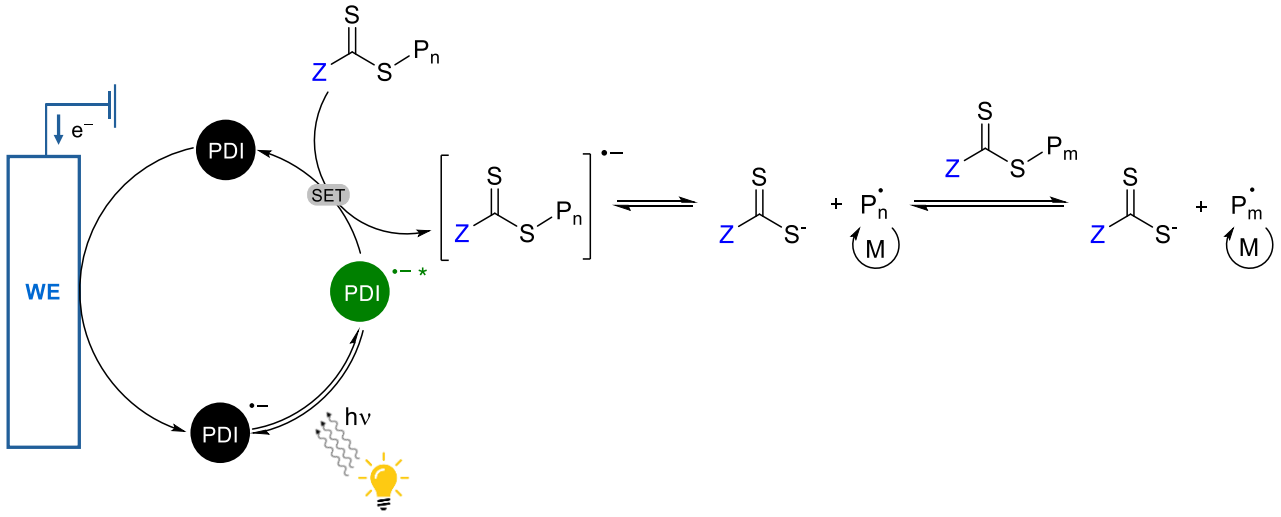

Scheme 15. PET-eRAFT reaction mechanism catalyzed by PDI •−.

The proposed pathway for the activation of the RAFT agent is an electron transfer (ET) reaction. In the PET-*e*RAFT process PDI$^{\bullet-}$ acts as a "mediator" that shuttles the electron from the electrode to the chain transfer agent in solution when photoexcited, thus realizing a homogenous ET. The anion radical with a standard reduction potential $E^{\ominus}$ = −0,45 V vs SCE is inert towards the activation of the chain transfer agent (E_{pc}(CDTPA) = −1,05 V vs SCE). On the contrary, *PDI$^{\bullet-}$ with a potential of −1,87 V vs SCE can reduce the chain transfer agent, while leaving the monomer (methyl methacrylate) intact (onset potential for monomer reduction E_{onset} = −1,97 V vs SCE)[103].

Because of the presence of two switches to trigger and control the reaction (one in the applied potential and the other in the excitation wavelength), various polymerization conditions were investigated, varying both the stimuli separately.

i) Effect of excitation wavelength

To test the effect of the excitation wavelength a series of different LEDs were tested, maintaining the applied potential constant at $E^{I}_{1/2}$ −60 mV (−0,51 V vs SCE). The half-wave potentials of the first and second reduced species are denoted by $E^{I}_{1/2}$ and $E^{II}_{1/2}$ respectively. The applied potentials were tested ranging from a more positive potential with respect to $E_{1/2}$. A more negative potential in the reaction mixture results in faster formation and increased production of the reduced species.

The potential was selected in order to rapidly produce the anion radical ($PDI^{\bullet-}$) without generating the PDI^{2-} species (Figure 39a). The LEDs wavelengths were selected according to target different portions of the anion radical spectrum (Figure 39b).

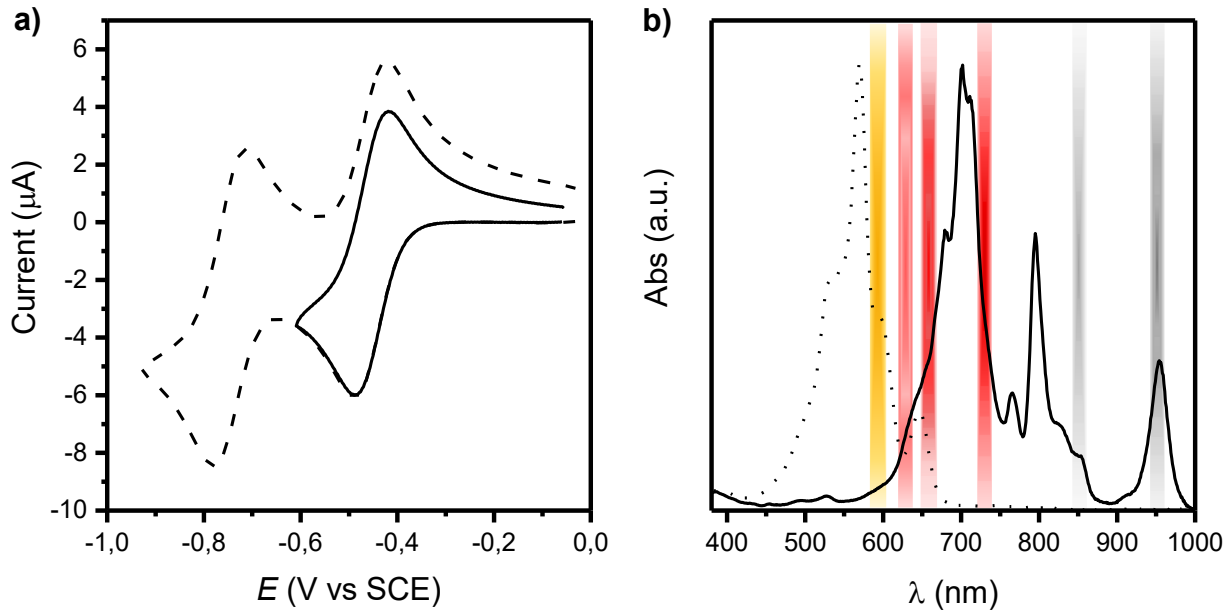

Figure 39. (a) CV of 1 mM PDI in DMF + 0.1 M n-Bu4NBF4 on a GC electrode (A = 7,07 mm^2) at T = 25 °C. Scan rate = 0,03 V s^{-1}. CV in the dashed line was recorded with a more negative inversion potential. (b) Spectra of $PDI^{\bullet-}$ (full line) and PDI^{2-} (dotted line) with overlapping, colored bands relative to the tested wavelengths. A total of six different wavelengths were tested, ranging from the visible to near infrared region of the spectrum. Reactions were performed and analyzed according to the procedure discussed in detail in section 2 (experimental).

Each tested wavelength produced different results, suggesting that the absorption band corresponded to distinct electronic transitions, resulting in unique reactivity for each case. The obtained results from polymerization reactions are reported in Table 9. A set of control experiments were conducted to better probe the reactivity of the system (entries 1 to 3, Table 9).

Table 9. Effect of irradiation wavelength on PET-eRAFT polymerizations with constant applied potential [a].

Entry	λ [b] (nm)	ε [c] (M^{-1} cm^{-1})	$k_{p,app} \times 10^5$ [d] (s^{-1})	t_{ind} [e] (h)	Conv [f] (%)	$M_{n,th}$ [g]	$M_{n,GPC}$ [h]	Đ [h]	I* [i] (%)	Q [j] (C)
1*	None	/	/	/	0	/	/	/	/	/
2§	630	16013	/	/	11,3	2651	6341	1,28	41,8	/
3†	630	16013	/	/	0	/	/	/	/	/
4‡	630	16013	/	/	0	/	/	/	/	/
5	595	5566	0	/	0	/	/	/	/	−1,99
6	630	16013	3,8	1,4	54,9	11243	8682	1,17	129,5	−2,34
7	660	30926	3,7	1,5	53,1	11090	10603	1,19	104,6	−3,49
8	730	38676	1,6	0,35	33,7	7069	6093	1,18	89,8	−2,64
9	850	11649	0,21	0	4,1	1229	3928	1,21	31,3	−1,25
10	950	27288	0	/	0	/	/	/	/	−3,04

[a] Conditions: [MMA]:[CDTPA]:[PDI]=[200]:[1]:[0,02]; 6,7 mL of solvent (DMF) + 0,1 M Bu_4NBF_4, 3,3 mL of MMA; platinum gauze as working electrode; separated cell; constant applied potential of -0,51 V vs SCE, measured under polymerization conditions; T = 35 °C. [b] Different LEDs used as light source (for further information see experimental section). [c] Data obtained from spectroelectrochemistry of PDI in a 1,5 mm quartz cuvette. [d] Calculated as the slope of linear fitting of the logarithmic plot (see Figure 40a below). [e] Calculated as the x axis intercept of the linear fitting of the logarithmic plot. [f] Calculated after 7h via ^{1}H NMR (400 MHz). [g] Calculated as $\text{Conv} \times MW_{MMA} \times \frac{C^0_{MMA}}{C^0_{CDPTA}} + MW_{CDTPA}$. [h] Determined after 7h by Gel Permeation Chromatography in DMF (PMMA standard, 60°C). [i] I*=($M_{n,th}/M_{n,GPC}$) ×100. [j] Charge passed after 7h of polymerization, defined as the integral of the current over time. * General conditions respected with no irradiation; the cell was carefully kept away from any light source. § No potential applied. † No CDTPA was added to the reaction mixture. ‡ No PDI was added to the reaction mixture.

No polymerization was observed in the absence of light (entry 1). Performing the reaction without applying potential bias (Entry 2, Table 9) we observed traces of polymer after 7h (11% conversion). This is probably due to a small overlap between the tail of the 630 nm LED emission and PDI absorption spectrum. The resulting mechanism has not been investigated as it remains sluggish and bare little to no interest for the study of the system. Very slow polymerization was observed in the absence of applied potential (entry 2). This might be due to slight light absorption by neutral PDI. No polymerization was also observed in the absence of CTA (entry 3) or catalyst (entry 4). In the presence of the

complete e-PRC system (CTA, PDI, light and applied potential) most reactions showed a good conversion and a good amount of control over the molecular weight distribution, indicating the successful catalytic reduction of CDTPA.

The catalytic character of the reaction is also indicated by the color of the solution: when PDI is reduced at the electrode in the presence of the CTA it retains its original bright orange color (typical of a neutral PDI solution) while if PDI is reduced without the RAFT agent the solution turns to dark green (characteristic color of $PDI^{\bullet-}$, which accumulates in solution in the absence of a substrate).

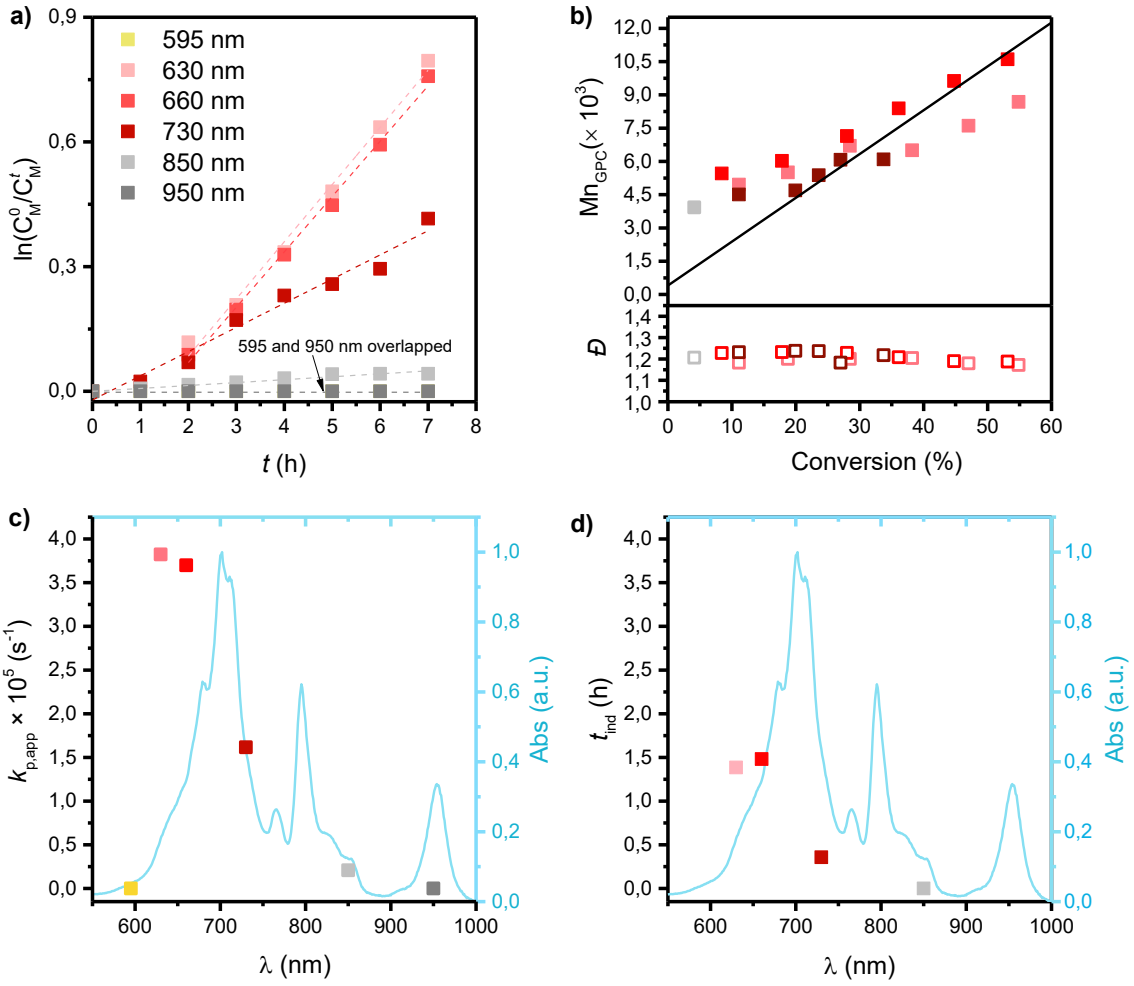

Figure 40. a) Comparison between the kinetics of the various polymerizations conducted with different wavelengths. b) Average molecular weight and dispersity with conversion. The full black line represents the theoretical M_n. c) Variation of apparent rate constant of polymerization with different excitation wavelengths. The absorption spectrum of $PDI^{\bullet-}$ is overlapped. d) Variation of the induction period with the different excitation wavelengths.

The variables of interest are reaction rate (measured with $k_{p,app}$, the slope of the semilogarithmic plot), dispersity ($Đ$), average molar weight (M_n) and the induction period.

The rate of polymerization is somehow correlated with the molar absorption coefficient (ε) of $PDI^{\bullet-}$. No conversion was observed with the yellow light, where the absorption coefficient is minimum. A rapid reaction was observed with the red lights, but the trend did not precisely match that of ε. Slow polymerization was observed with 850 nm NIR lamp, and no polymerization with 950 nm NIR lamp. This can indicate that different electronic states are excited by the different lamps, and each electron level is contributing in a specific way to the reactivity.

In Table 9, the induction period indicates the time after which a detectable value of conversion is registered. It corresponds to the effective "zero time" indicating the start of polymerization.

The results obtained indicate a good control over the polymerization. The GPC signals support the results indicating a controlled process. The chromatographic traces show a progressively narrower distribution and increasing molecular weight (Figure 41b).

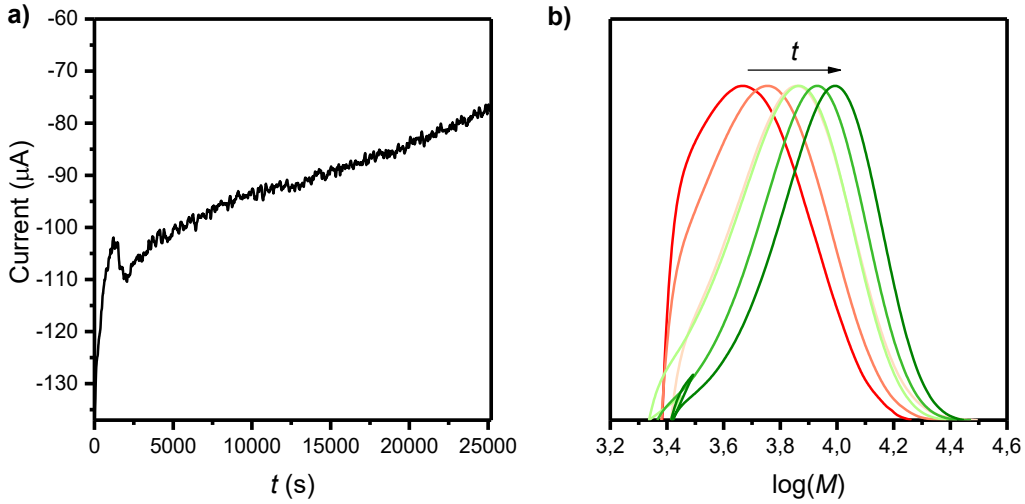

Figure 41. a) Chronoamperometry of the polymerization reaction. The signal accounts for the reduction at the electrode. b) GPC traces of the reaction from 2h to 7h

From the current vs time plot (chronoamperometry, Figure 41a) it was possible to determine the charge passed (Q) while the theoretical charge (Q_{th}) was calculated by using Faraday's law of electrolysis:

$$Q = \int_0^t I(t)\,\mathrm{d}t = zFn \tag{3.3. 1}$$

$$Q_{th} = zFn \tag{3.3.2}$$

where and z is the number of electrons required for the redox process, F is the Faraday's constant and n is the number of moles of the substrate.

Comparing the obtained value with the theoretical charge (Q_{th}) to reduce PDI to $PDI^{\bullet-}$ or PDI^{2-} it is possible to determine the number of cycles carried out. The theoretical charge is calculated with equation 3.3.2 using $z = 1$ for the reduction of PDI to $PDI^{\bullet-}$ and $z = 2$ to PDI^{2-}. Taking in exam the polymerization performed with a 630 nm LED (entry 6,Table 9) a total of 8 reduction cycles (i.e. turnover number) for the catalyst were calculated. It must be noted that the obtained value takes into consideration the self-oxidation of the $PDI^{\bullet-}$ in addition to the catalytic reaction. From the passed charge it is possible to estimate the percentage of CDTPA still present after the electrolysis time. In the specific case of entry 6 it resulted that 84% of the CTA was still present.

ii) Effect of applied potential

After observing the behavior of different excitation wavelengths on $PDI^{\bullet-}$ the second external stimulus was varied. A set of applied potential variations was studied to observe the change in reactivity and polymerization parameters while keeping the same 630 nm irradiation (Table 10).

Table 10. Effect of applied potential on PET-eRAFT polymerizations with constant irradiation wavelength [a].

Entry	E_{app} [b] (V vs SCE)		$k_{p,app} \times 10^{-5}$ [c] (s^{-1})	t_{ind} [d] (h)	Conv [e] (%)	$M_{n,th}$ [f]	$M_{n,GPC}$ [g]	$Đ$ [g]	I* [h] (%)	Q [j] (C)
2	$E^{I}_{1/2}$ + 20 mV	− 0,43	2,61	2,2	38,7	8060	7945	1,21	101,4	−1,22
3	$E^{I}_{1/2}$	− 0,45	2,58	1,1	41,5	8595	9643	1,17	89,1	−1,61
4	$E^{I}_{1/2}$− 60 mV	− 0,51	3,82	1,4	54,9	11243	8682	1,17	129,5	−2,34
5	$E^{I}_{1/2}$− 120 mV	− 0,57	3,92	1,8	53,1	11081	8809	1,18	125,8	−3,57
6	$E^{II}_{1/2}$+ 60 mV	− 0,68	4,43	2,5	48,8	10183	11190	1,20	91,0	−6,55
7	$E^{II}_{1/2}$	− 0,74	5,63	3,8	49,2	10245	10424	1,21	98,3	−7,52

[a] Conditions: [MMA]:[CDTPA]:[PDI]=[200]:[1]:[0,02]; 6,7 mL of solvent (DMF) + 0,1 M Bu_4NBF_4, 3,3 mL of MMA; platinum gauze as working electrode; polymerization performed with a 630 nm red LED as light source; T = 35 °C. [b] Applied potential vs SCE,

measured under polymerization conditions. [c] Calculated as the slope of linear fitting of the logarithmic plot (see Figure 42a below). [d] Calculated as the x axis intercept of the linear fitting of the logarithmic plot. .[e] Calculated after 7 h via ^{1}H NMR (400 Mhz). [f] Calculated as Conv × MW_{MMA} × $\frac{C^0_{MMA}}{C^0_{CDTPA}}$ + MW_{CDTPA}. [g] Determined after 7 h by Gel Permeation Chromatography in DMF (PMMA standard, 60°C). [h] I*=($M_{n,th}/M_{n,GPC}$) ×100. [j] Charge passed after 7h of polymerization, defined as the integral of the current over time.

For this series both the first and second reduced forms of the catalyst have been evaluated. The explored potentials always refer to the nearest halfwave potential, so that $E^{I}_{1/2}$ indicates the halfwave potential for the first reduction and $E^{II}_{1/2}$ the halfwave potential for the second reduction. Being in both cases reversible peaks, the halfwave potential corresponds to the standard reduction potential.

The charge passed was evaluated for this set of experiments as well. The values of charge passed roughly increase in module according to the applied potential, with more negative potentials inducing more charge consumption.

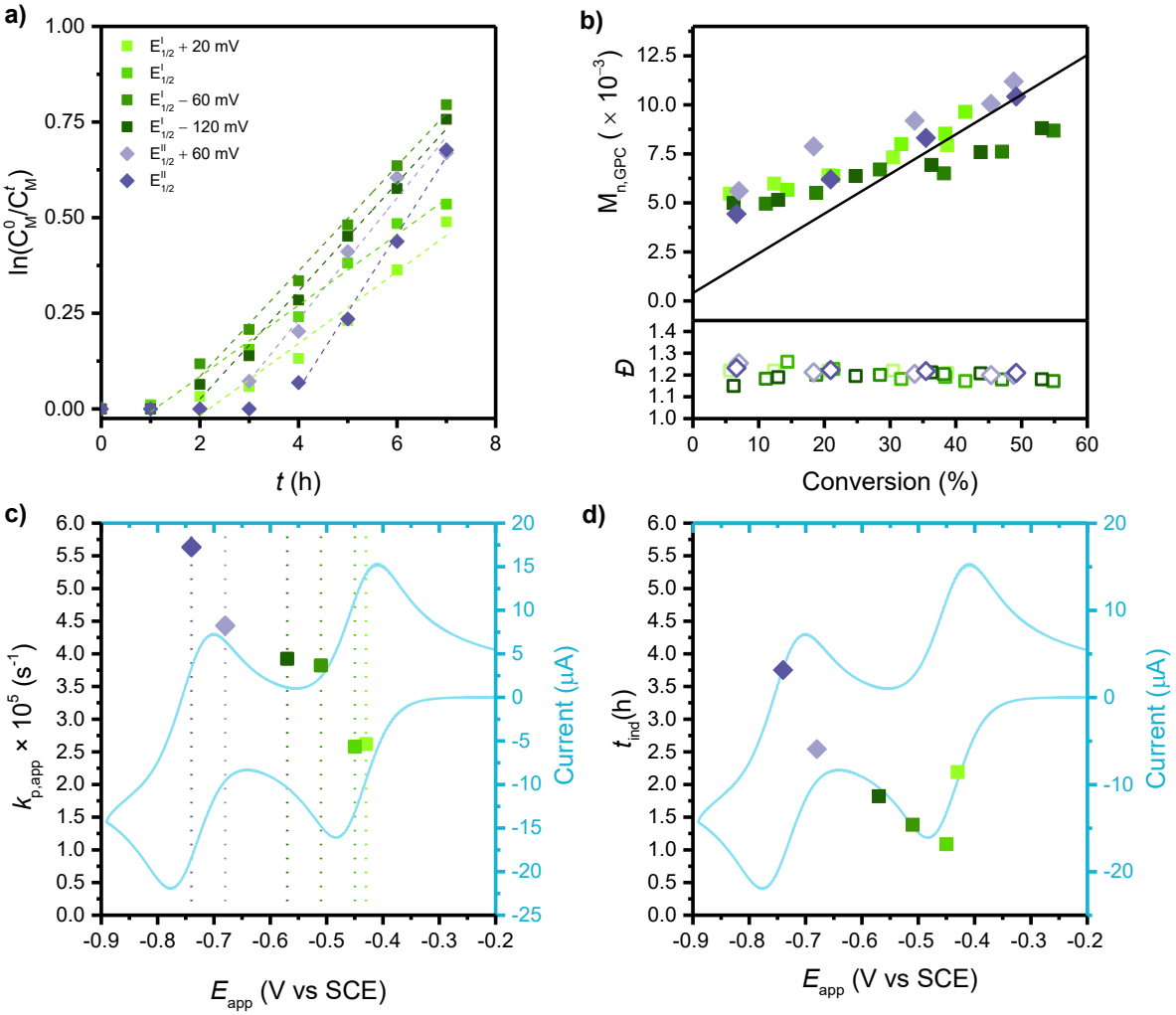

Figure 42. a) Comparison between the kinetics of the various polymerizations conducted with different applied potentials. b) Average molecular weight and dispersity with conversion. The full black line represents the theoretical M_n. c) Variation of apparent rate constant

of polymerization with different applied potentials. The CV of PDI is overlapped. d) Variation of the induction period with the different applied potentials.

In this case it is possible to notice a correlation between rate of polymerization and applied potential. More specifically the polymerization rate appears to be higher when the potential is more negative. This is coherent with the basic principle by which a higher concentration of the reducing agent produces a higher quantity of cleaved chain transfer agent. An even faster rate of polymerization is observed when the potential is applied in a region where the dianion PDI^{2-} is generated.

The induction period indicates the time after which a detectable value of conversion is registered. It corresponds to the effective zero time indicating the start of polymerization. The induction time also increases when more negative potential is applied. This correlation between applied potential and induction period, as well as its counterintuitive relationship with $k_{p,app}$, remains unclear. Further experiments are needed to clarify these trends.

4. Conclusions and outlook

This research has focused on exploring the photo-electrochemical control of Reversible Addition-Fragmentation Chain Transfer (RAFT) polymerization using an electrochemically mediated photoredox catalysis (e-PRC) system, with the organic dye *N*,*N*-bis(2,6-diisopropylphenyl)perylene-3,4,9,10-bis(dicarboximide) (PDI) serving as the catalyst. Two major objectives were addressed: i) the determination of rate constants for radical generation using cyclic voltammetry (CV), complemented by comparison of the obtained data with Marcus-Savéant outer-sphere electron transfer (OSET) theory and time-correlated single-photon counting (TCSPC); and ii) the application of the electrophotocatalytic system to RAFT polymerization, utilizing dual control switches—excitation wavelength and applied potential.

i) CV Analysis and Radical Generation Rate Constants

Cyclic voltammetry was employed to study the electrochemical behavior of PDI and its ability to generate radicals. The reduced forms of PDI in their excited state (*$PDI^{\bullet-}$ and *PDI^{2-}) were found to exhibit effective catalytic activity towards the targeted substrates (alkyl and aryl halides). The CV analysis allowed for the quantification of radical generation rate constants, which were subsequently compared with theoretical values derived from Marcus-Savéant OSET theory. This comparison validated the experimental data obtained by CV and highlighted that the radical generation process adhered to dissociative electron transfer (DET) pathways. These findings highlight the effectiveness of CV analysis in understanding the kinetics and mechanisms of the e-PRC process. This method proves valuable for possible broader applications in studying of e-PRC systems, demonstrating robustness despite the complexity added by the photochemical steps. The integration of CV analysis with the predictive capabilities of Marcus theory offers a comprehensive framework for both theoretical and experimental investigation of e-PRC systems. Additionally, TCSPC measurements provided insights into the excited-state dynamics and fluorescence lifetimes of *PDI^{2-}, offering complementary data to CV analysis and further supporting the method.

ii) Application to RAFT Polymerization

The second major objective was to apply the PDI-catalyzed e-PRC system to RAFT polymerization, aiming to exploit its ability to operate under mild conditions with low-energy light (630 nm and above) and mild electrochemical potentials (down to −0.43 V vs SCE). The unique feature of this system is its dual control, where both the excitation wavelength and the applied potential can be used

as independent switches to regulate the polymerization process. This approach offers unprecedented flexibility, making it possible to tune polymerization conditions operating on two diverse sources.

During these polymerization experiments, it was observed that the induction period and polymerization rate exhibited a counterintuitive relationship, raising questions about the underlying mechanisms. This phenomenon suggests complex interactions between the photochemical and electrochemical parameters, which may involve competing processes such as radical generation and deactivation.

iii) Outlook

The integration of cyclic voltammetry (CV) analysis with the predictive power of Marcus theory has proven effective in studying the kinetics and mechanisms of e-PRC systems, even under the complexity introduced by light irradiation. This study highlights the potential of CV analysis as a powerful tool for investigating electro-photocatalytic reactions. Future work should focus on applying the developed CV technique to study and improve the mechanism of highly reactive e-PRC catalysts. This could include integrating advanced spectroscopic techniques such as transient absorption spectroscopy (TAS), as well as time-correlated single-photon counting (TCSPC) to better capture catalyst behavior in different timescales and gain deeper mechanistic insights. Developing standardized protocols for these analyses could enable the broader application of CV in studying a wide range of electrophotochemical reactions, providing critical kinetic and mechanistic data to advance the field of e-PRC.

In parallel, the findings of this study provide a solid foundation for further exploration of photoelectrochemical RAFT polymerization and other RDRP techniques using e-PRC systems. Future research should delve deeper into understanding the relationship between induction periods, polymerization rates, and the roles of catalyst concentration, excitation wavelength and applied potential. The polymerization under NIR irradiation (850 nm) should be further investigated and optimized.

In conclusion, this thesis has demonstrated the potential of combining photochemical and electrochemical techniques to generate radicals and achieve controlled radical polymerization, contributing valuable insights to the fields of polymer chemistry.

References

(1) Hedstrand, D. M.; Kruizinga, W. H.; Kellogg, R. M. Light Induced and Dye Accelerated Reductions of Phenacyl Onium Salts by 1,4-Dihydropyridines. *Tetrahedron Lett.* **1978**, *19* (14), 1255–1258. https://doi.org/10.1016/S0040-4039(01)94515-0.

(2) Pac, C.; Ihama, M.; Yasuda, M.; Miyauchi, Y.; Sakurai, H. Tris(2,2'-Bipyridine)Ruthenium(2+)-Mediated Photoreduction of Olefins with 1-Benzyl-1,4-Dihydronicotinamide: A Mechanistic Probe for Electron-Transfer Reactions of NAD(P)H-Model Compounds. *J. Am. Chem. Soc.* **1981**, *103* (21), 6495–6497. https://doi.org/10.1021/ja00411a040.

(3) Hironaka, K.; Fukuzumi, S.; Tanaka, T. Tris(Bipyridyl)Ruthenium(II)-Photosensitized Reaction of 1-Benzyl-1,4-Dihydronicotinamide with Benzyl Bromide. *J. Chem. Soc. Perkin Trans. 2* **1984**, No. 10, 1705. https://doi.org/10.1039/p29840001705.

(4) Okada, K.; Okamoto, K.; Morita, N.; Okubo, K.; Oda, M. Photosensitized Decarboxylative Michael Addition through N-(Acyloxy)Phthalimides via an Electron-Transfer Mechanism. *J. Am. Chem. Soc.* **1991**, *113* (24), 9401–9402. https://doi.org/10.1021/ja00024a074.

(5) Prier, C. K.; Rankic, D. A.; MacMillan, D. W. C. Visible Light Photoredox Catalysis with Transition Metal Complexes: Applications in Organic Synthesis. *Chem. Rev.* **2013**, *113* (7), 5322–5363. https://doi.org/10.1021/cr300503r.

(6) Shaw, M. H.; Twilton, J.; MacMillan, D. W. C. Photoredox Catalysis in Organic Chemistry. *J. Org. Chem.* **2016**, *81* (16), 6898–6926. https://doi.org/10.1021/acs.joc.6b01449.

(7) Romero, N. A.; Nicewicz, D. A. Organic Photoredox Catalysis. *Chem. Rev.* **2016**, *116* (17), 10075–10166. https://doi.org/10.1021/acs.chemrev.6b00057.

(8) Nicewicz, D. A.; MacMillan, D. W. C. Merging Photoredox Catalysis with Organocatalysis: The Direct Asymmetric Alkylation of Aldehydes. *Science* **2008**, *322* (5898), 77–80. https://doi.org/10.1126/science.1161976.

(9) Zuo, Z.; Ahneman, D. T.; Chu, L.; Terrett, J. A.; Doyle, A. G.; MacMillan, D. W. C. Merging Photoredox with Nickel Catalysis: Coupling of α-Carboxyl Sp^3 -Carbons with Aryl Halides. *Science* **2014**, *345* (6195), 437–440. https://doi.org/10.1126/science.1255525.

(10) Corcoran, E. B.; Pirnot, M. T.; Lin, S.; Dreher, S. D.; DiRocco, D. A.; Davies, I. W.; Buchwald, S. L.; MacMillan, D. W. C. Aryl Amination Using Ligand-Free Ni(II) Salts and Photoredox Catalysis. *Science* **2016**, *353* (6296), 279–283. https://doi.org/10.1126/science.aag0209.

(11) Cismesia, M. A.; Yoon, T. P. Characterizing Chain Processes in Visible Light Photoredox Catalysis. *Chem. Sci.* **2015**, *6* (10), 5426–5434. https://doi.org/10.1039/C5SC02185E.

(12) Du, J.; Skubi, K. L.; Schultz, D. M.; Yoon, T. P. A Dual-Catalysis Approach to Enantioselective [2 + 2] Photocycloadditions Using Visible Light. *Science* **2014**, *344* (6182), 392–396. https://doi.org/10.1126/science.1251511.

(13) Narayanam, J. M. R.; Tucker, J. W.; Stephenson, C. R. J. Electron-Transfer Photoredox Catalysis: Development of a Tin-Free Reductive Dehalogenation Reaction. *J. Am. Chem. Soc.* **2009**, *131* (25), 8756–8757. https://doi.org/10.1021/ja9033582.

(14) Nguyen, J. D.; D'Amato, E. M.; Narayanam, J. M. R.; Stephenson, C. R. J. Engaging Unactivated Alkyl, Alkenyl and Aryl Iodides in Visible-Light-Mediated Free Radical Reactions. *Nat. Chem.* **2012**, *4* (10), 854–859. https://doi.org/10.1038/nchem.1452.

(15) Kotani, H.; Ohkubo, K.; Fukuzumi, S. Photocatalytic Oxygenation of Anthracenes and Olefins with Dioxygen via Selective Radical Coupling Using 9-Mesityl-10-Methylacridinium Ion as an Effective Electron-Transfer Photocatalyst. *J. Am. Chem. Soc.* **2004**, *126* (49), 15999–16006. https://doi.org/10.1021/ja048353b.

(16) Ohkubo, K.; Kobayashi, T.; Fukuzumi, S. Direct Oxygenation of Benzene to Phenol Using Quinolinium Ions as Homogeneous Photocatalysts. *Angew. Chem. Int. Ed.* **2011**, *50* (37), 8652–8655. https://doi.org/10.1002/anie.201102931.

(17) Fukuzumi, S.; Ohkubo, K. Organic Synthetic Transformations Using Organic Dyes as Photoredox Catalysts. *Org Biomol Chem* **2014**, *12* (32), 6059–6071. https://doi.org/10.1039/C4OB00843J.
(18) Romero, N. A.; Margrey, K. A.; Tay, N. E.; Nicewicz, D. A. Site-Selective Arene C-H Amination via Photoredox Catalysis. *Science* **2015**, *349* (6254), 1326–1330. https://doi.org/10.1126/science.aac9895.
(19) Hamilton, D. S.; Nicewicz, D. A. Direct Catalytic Anti-Markovnikov Hydroetherification of Alkenols. *J. Am. Chem. Soc.* **2012**, *134* (45), 18577–18580. https://doi.org/10.1021/ja309635w.
(20) Hari, D. P.; Schroll, P.; König, B. Metal-Free, Visible-Light-Mediated Direct C–H Arylation of Heteroarenes with Aryl Diazonium Salts. *J. Am. Chem. Soc.* **2012**, *134* (6), 2958–2961. https://doi.org/10.1021/ja212099r.
(21) Romero, K. J.; Galliher, M. S.; Pratt, D. A.; Stephenson, C. R. J. Radicals in Natural Product Synthesis. *Chem. Soc. Rev.* **2018**, *47* (21), 7851–7866. https://doi.org/10.1039/C8CS00379C.
(22) Glaser, F.; Kerzig, C.; Wenger, O. S. Multi-Photon Excitation in Photoredox Catalysis: Concepts, Applications, Methods. *Angew. Chem. Int. Ed.* **2020**, *59*, 10266–10284. https://doi.org/doi.org/10.1002/anie.201915762.
(23) Faraday, M. VI. Experimental Researches in Electricity.-Seventh Series. *Philos. Trans. R. Soc. Lond. R. Soc.* **1834**, *124*, 77–122. https://doi.org/10.1098/rstl.1834.0008.
(24) Kolbe, H. Untersuchungen über die Elektrolyse organischer Verbindungen. *Justus Liebigs Ann. Chem.* **1849**, *69* (3), 257–294. https://doi.org/10.1002/jlac.18490690302.
(25) Wiebe, A.; Gieshoff, T.; Möhle, S.; Rodrigo, E.; Zirbes, M.; Waldvogel, S. R. Electrifying Organic Synthesis. *Angew. Chem. Int. Ed.* **2018**, *57* (20), 5594–5619. https://doi.org/10.1002/anie.201711060.
(26) Dai, C.; Meschini, F.; Narayanam, J. M. R.; Stephenson, C. R. J. Friedel–Crafts Amidoalkylation via Thermolysis and Oxidative Photocatalysis. *J. Org. Chem.* **2012**, *77* (9), 4425–4431. https://doi.org/10.1021/jo300162c.
(27) Jeffrey, J. L.; Terrett, J. A.; MacMillan, D. W. C. O–H Hydrogen Bonding Promotes H-Atom Transfer from α C–H Bonds for C-Alkylation of Alcohols. *Science* **2015**, *349* (6255), 1532–1536. https://doi.org/10.1126/science.aac8555.
(28) Montanaro, S.; Ravelli, D.; Merli, D.; Fagnoni, M.; Albini, A. Decatungstate As Photoredox Catalyst: Benzylation of Electron-Poor Olefins. *Org. Lett.* **2012**, *14* (16), 4218–4221. https://doi.org/10.1021/ol301900p.
(29) Ravelli, D.; Fagnoni, M.; Fukuyama, T.; Nishikawa, T.; Ryu, I. Site-Selective C–H Functionalization by Decatungstate Anion Photocatalysis: Synergistic Control by Polar and Steric Effects Expands the Reaction Scope. *ACS Catal.* **2018**, *8* (1), 701–713. https://doi.org/10.1021/acscatal.7b03354.
(30) Tarantino, K. T.; Liu, P.; Knowles, R. R. Catalytic Ketyl-Olefin Cyclizations Enabled by Proton-Coupled Electron Transfer. *J. Am. Chem. Soc.* **2013**, *135* (27), 10022–10025. https://doi.org/10.1021/ja404342j.
(31) Choi, G. J.; Knowles, R. R. Catalytic Alkene Carboaminations Enabled by Oxidative Proton-Coupled Electron Transfer. *J. Am. Chem. Soc.* **2015**, *137* (29), 9226–9229. https://doi.org/10.1021/jacs.5b05377.
(32) Barber, J.; Andersson, B. Revealing the Blueprint of Photosynthesis. *Nature* **1994**, *370* (6484), 31–34. https://doi.org/10.1038/370031a0.
(33) Padghan, S. D.; Puyad, A. L.; Bhosale, R. S.; Bhosale, S. V.; Bhosale, S. V. A Pyrene Based Fluorescent Turn-on Chemosensor: Aggregation-Induced Emission Enhancement and Application towards Fe3+ and Fe2+ Recognition. *Photochem. Photobiol. Sci.* **2017**, *16* (11), 1591–1595. https://doi.org/10.1039/c7pp00329c.

(34) Ghosh, I.; Ghosh, T.; Bardagi, J. I.; König, B. Reduction of Aryl Halides by Consecutive Visible Light-Induced Electron Transfer Processes. *Science* **2014**, *346* (6210), 725–728. https://doi.org/10.1126/science.1258232.
(35) Ghosh, I.; König, B. Chromoselective Photocatalysis:Controlled Bond Activation through Light-Color Regulation of Redox Potentials. *Angew. Chem. Int. Ed.* **2016**, *55*, 7676–7679. https://doi.org/10.1002/anie.201602349.
(36) Fantin, M.; Lorandi, F.; Ribelli, T. G.; Szczepaniak, G.; Enciso, A. E.; Fliedel, C.; Thevenin, L.; Isse, A. A.; Poli, R.; Matyjaszewski, K. Impact of Organometallic Intermediates on Copper-Catalyzed Atom Transfer Radical Polymerization. *Macromolecules* **2019**, *52* (11), 4079–4090. https://doi.org/10.1021/acs.macromol.9b00870.
(37) Moutet, J.-C.; Reverdy, G. Photochemistry of Cation Radicals in Solution: Photoinduced Oxidation by the Phenothiazine Cation Radical. *Tetrahedron Lett.* **1979**, *26*, 2389–2392. https://doi.org/10.1016/S0040-4039(01)86300-0.
(38) Moutet, J.-C.; Reverdy, G. Phototochemistry of Cation Radicals in Solution; Photoinduced Electron-Transfer Reactions between Alcholos and the N,N,N′,N′,-Tetraphenyl-p-Phenylenediamine Cation Radical. *J. Chem. Soc. Chem. Commun.* **1982**, No. 12, 654–655. https://doi.org/10.1039/C39820000654.
(39) Scheffold, R.; Orlinski, R. Synthesis and Reactions of Porphine-Type Metal Complexes. 15. Carbon-Carbon Bond Formation by Light Assisted B12-Catalysis. Nucleophilic Acylation of Michael Olefins. *J. Am. Chem. Soc.* **1983**, *105* (24), 7200–7202. https://doi.org/10.1021/ja00362a047.
(40) Grimaud, L.; Lakhdar, S.; Vitale, M. R. Electrophotocatalysis: Taking the Best from the Two Worlds. *Curr. Opin. Electrochem.* **2023**, *40*, 101307. https://doi.org/10.1016/j.coelec.2023.101307.
(41) Huang, H.; Steiniger, K. A.; Lambert, T. H. Electrophotocatalysis: Combining Light and Electricity to Catalyze Reactions. *J. Am. Chem. Soc.* **2022**, *144* (28), 12567–12583. https://doi.org/10.1021/jacs.2c01914.
(42) Qian, L.; Shi, M. Contemporary Photoelectrochemical Strategies and Reactions in Organic Synthesis. *Chem. Commun.* **2023**, *59* (24), 3487–3506. https://doi.org/10.1039/D3CC00437F.
(43) Wu, S.; Kaur, J.; Karl, T. A.; Tian, X.; Barham, J. P. Synthetic Molecular Photoelectrochemistry: New Frontiers in Synthetic Applications, Mechanistic Insights and Scalability. *Angew. Chem. Int. Ed.* **2022**, *61* (12), e202107811. https://doi.org/10.1002/anie.202107811.
(44) Bessegato, G. G.; Guaraldo, T. T.; De Brito, J. F.; Brugnera, M. F.; Zanoni, M. V. B. Achievements and Trends in Photoelectrocatalysis: From Environmental to Energy Applications. *Electrocatalysis* **2015**, *6* (5), 415–441. https://doi.org/10.1007/s12678-015-0259-9.
(45) Wang, F.; Stahl, S. S. Merging Photo Chemistry with Electrochemistry: Functional-Group Tolerant Electrochemical Amination ofC(Sp3)-HBonds. *Angew. Chem. Int. Ed.* **2019**, *58*, 6385–6390. https://doi.org/10.1002/anie.20181396.
(46) Barham, J. P.; König, B. Synthetic Photoelectrochemistry. *Angew. Chem. Int. Ed.* **2020**, *59* (29), 11732–11747. https://doi.org/10.1002/anie.201913767.
(47) Cowper, N. G. W.; Chernowsky, C. P.; Williams, O. P.; Wickens, Z. K. Potent Reductants via Electron-Primed Photoredox Catalysis: Unlocking Aryl Chlorides for Radical Coupling. *J. Am. Chem. Soc.* **2020**, *142* (5), 2093–2099. https://doi.org/10.1021/jacs.9b12328.
(48) Tian, X.; Karl, T. A.; Reiter, S.; Yakubov, S.; de Vivie-Riedle, R.; König, B.; Barham, J. P. Electro-Mediated PhotoRedox Catalysisfor Selective C(Sp3)–O Cleavages of Phosphinated Alcohols to Carbanions. *Angew. Chem. Int. Ed.* **2021**, *60*, 20817–20825. https://doi.org/doi.org/10.1002/anie.202105895.
(49) Shen, T.; Lambert, T. H. Electrophotocatalytic Diamination of Vicinal C–H Bonds. *Science* **2021**, *371* (6529), 620–626. https://doi.org/10.1126/science.abf2798.
(50) Shen, T.; Lambert, T. H. C–H Amination via Electrophotocatalytic Ritter-Type Reaction. *J. Am. Chem. Soc.* **2021**, *143* (23), 8597–8602. https://doi.org/10.1021/jacs.1c03718.

(51) Huang, H.; Strater, Z. M.; Lambert, T. H. Electrophotocatalytic C–H Functionalization of Ethers with High Regioselectivity. *J. Am. Chem. Soc.* **2020**, *142* (4), 1698–1703. https://doi.org/10.1021/jacs.9b11472.
(52) Wu, S.; Žurauskas, J.; Domański, M.; Hitzfeld, P. S.; Butera, V.; Scott, D. J.; Rehbein, J.; Kumar, A.; Thyrhaug, E.; Hauer, J.; Barham, J. P. Hole-Mediated Photoredox Catalysis: Tris(*p* -Substituted)Biarylaminium Radical Cations as Tunable, Precomplexing and Potent Photooxidants. *Org. Chem. Front.* **2021**, *8* (6), 1132–1142. https://doi.org/10.1039/D0QO01609H.
(53) Cole, J. P.; Chen, D.-F.; Kudisch, M.; Pearson, R. M.; Lim, C.-H.; Miyake, G. M. Organocatalyzed Birch Reduction Driven by Visible Light. *J. Am. Chem. Soc.* **2020**, *142* (31), 13573–13581. https://doi.org/10.1021/jacs.0c05899.
(54) Rieth, A. J.; Gonzalez, M. I.; Kudisch, B.; Nava, M.; Nocera, D. G. How Radical Are "Radical" Photocatalysts? A Closed-Shell Meisenheimer Complex Is Identified as a Super-Reducing Photoreagent. *J. Am. Chem. Soc.* **2021**, *143* (35), 14352–14359. https://doi.org/10.1021/jacs.1c06844.
(55) Jeong, D. Y.; Lee, D. S.; Lee, H. L.; Nah, S.; Lee, J. Y.; Cho, E. J.; You, Y. Evidence and Governing Factors of the Radical-Ion Photoredox Catalysis. *ACS Catal.* **2022**, *12* (10), 6047–6059. https://doi.org/10.1021/acscatal.2c00763.
(56) Horsewill, S. J.; Hierlmeier, G.; Farasat, Z.; Barham, J. P.; Scott, D. J. Shining Fresh Light on Complex Photoredox Mechanisms through Isolation of Intermediate Radical Anions. *ACS Catal.* **2023**, *13* (14), 9392–9403. https://doi.org/10.1021/acscatal.3c02515.
(57) Mandigma, M. J. P.; Kaur, J.; Barham, J. P. Organophotocatalytic Mechanisms: Simplicity or Naïvety? Diverting Reactive Pathways by Modifications of Catalyst Structure, Redox States and Substrate Preassemblies. *ChemCatChem* **2023**, *15* (11), e202201542. https://doi.org/10.1002/cctc.202201542.
(58) Sau, A.; Pompetti, N. F.; Green, A. R.; Popescu, M. V.; Paton, R. S.; Miyake, G. M.; Damrauer, N. H. Mechanistic Investigation of a Photocatalyst Model Reveals Function by Perylene-Like Closed Shell Super-Photoreductant Capable of Reducing Unactivated Arenes. *ACS Catal.* **2024**, *14* (4), 2252–2263. https://doi.org/10.1021/acscatal.3c05386.
(59) Pfund, B.; Gejsnæs-Schaad, D.; Lazarevski, B.; Wenger, O. S. Picosecond Reactions of Excited Radical Ion Super-Reductants. *Nat. Commun.* **2024**, *15* (1), 4738. https://doi.org/10.1038/s41467-024-49006-5.
(60) Yan, H.; Hou, Z.; Xu, H. Photoelectrochemical C−H Alkylation of Heteroarenes with Organotrifluoroborates. *Angew. Chem.* **2019**, *131* (14), 4640–4643. https://doi.org/10.1002/ange.201814488.
(61) Lai, X.; Shu, X.; Song, J.; Xu, H. Electrophotocatalytic Decarboxylative C−H Functionalization of Heteroarenes. *Angew. Chem.* **2020**, *132* (26), 10713–10719. https://doi.org/10.1002/ange.202002900.
(62) Huang, H.; Lambert, T. H. Electrophotocatalytic S_NAr Reactions of Unactivated Aryl Fluorides at Ambient Temperature and Without Base. *Angew. Chem. Int. Ed.* **2020**, *59* (2), 658–662. https://doi.org/10.1002/anie.201909983.
(63) Huang, H.; Lambert, T. H. Electrophotocatalytic C−H Heterofunctionalization of Arenes. *Angew. Chem. Int. Ed.* **2021**, *60* (20), 11163–11167. https://doi.org/10.1002/anie.202100222.
(64) Miscellaneous Pigments. In *Industrial Organic Pigments*; 2004; pp 567–583. https://doi.org/10.1002/3527602429.ch4.
(65) Dimitrakopoulos, C. D.; Malenfant, P. R. L. Organic Thin Film Transistors for Large Area Electronics. *Adv. Mater.* **2002**, *14* (2), 99–117. https://doi.org/10.1002/1521-4095(20020116)14:2<99::AID-ADMA99>3.0.CO;2-9.
(66) Kozma, E.; Catellani, M. Perylene Diimides Based Materials for Organic Solar Cells. *Dyes Pigments* **2013**, *98* (1), 160–179. https://doi.org/10.1016/j.dyepig.2013.01.020.

(67) Gosztola, D.; Niemczyk, M. P.; Svec, W.; Lukas, A. S.; Wasielewski, M. R. Excited Doublet States of Electrochemically Generated Aromatic Imide and Diimide Radical Anions. *J. Phys. Chem. A* **2000**, *104* (28), 6545–6551. https://doi.org/10.1021/jp000706f.
(68) Renner, R.; Stolte, M.; Heitmüller, J.; Brixner, T.; Lambert, C.; Würthner, F. Substituent-Dependent Absorption and Fluorescence Properties of Perylene Bisimide Radical Anions and Dianions. *Mater. Horiz.* **2022**, *9* (1), 350–359. https://doi.org/10.1039/D1MH01019K.
(69) Würthner, F. Perylene Bisimide Dyes as Versatile Building Blocks for Functional Supramolecular Architectures. *Chem. Commun.* **2004**, No. 14, 1564–1579. https://doi.org/10.1039/B401630K.
(70) Yang, Y.-Y.; Zhang, P.; Hadjichristidis, N. Two-Photon Excitation Photoredox Catalysis Enabled Atom Transfer Radical Polymerization. *J. Am. Chem. Soc.* **2023**, *145* (23), 12737–12744. https://doi.org/10.1021/jacs.3c02832.
(71) La Porte, N. T.; Martinez, J. F.; Chaudhuri, S.; Hedström, S.; Batista, V. S.; Wasielewski, M. R. Photoexcited Radical Anion Super-Reductants for Solar Fuels Catalysis. *Coord. Chem. Rev.* **2018**, *361*, 98–119. https://doi.org/10.1016/j.ccr.2018.01.018.
(72) Zeman, C. J. I.; Kim, S.; Zhang, F.; Schanze, K. S. Direct Observation of the Reduction of Aryl Halides by a Photoexcited Perylene Diimide Radical Anion. *J. Am. Chem. Soc.* **2020**, *142* (5), 2204–2207. https://doi.org/10.1021/jacs.9b13027.
(73) Carlsson, H. S.; Lund, H. Photochemistry of Radical Ions. II. Influence of Thermal Convection and Photoexcitation on Voltammetric Curves. *Acta Chem. Scand.* **1980**, *34b*, 409–412. https://doi.org/10.3891/acta.chem.scand.34b-0409.
(74) Shukla, S. S.; Rusling, J. F. Photoelectrocatalytic Reduction of 4-Chlorobiphenyl Using Anion Radicals and Visible Light. *J. Phys. Chem.* **1985**, *89* (15), 3353–3358. https://doi.org/10.1021/j100261a039.
(75) Costentin, C.; Fortage, J.; Collomb, M.-N. Electrophotocatalysis: Cyclic Voltammetry as an Analytical Tool. *J. Phys. Chem. Lett.* **2020**, *11* (15), 6097–6104. https://doi.org/10.1021/acs.jpclett.0c01662.
(76) Matyjaszewski, K.; Xia, J. Atom Transfer Radical Polymerization. *Chem. Rev.* **2001**, *101* (9), 2921–2990. https://doi.org/10.1021/cr940534g.
(77) Szwarc, M.; Levy, M.; Milkovich, R. POLYMERIZATION INITIATED BY ELECTRON TRANSFER TO MONOMER. A NEW METHOD OF FORMATION OF BLOCK POLYMERS [1]. *J. Am. Chem. Soc.* **1956**, *78* (11), 2656–2657. https://doi.org/10.1021/ja01592a101.
(78) Szwarc, M. "LIVING" POLYMERS. *Nature* **1956**, *178*, 1168–1169. https://doi.org/10.1038/1781168a0.
(79) Fellows, C. M.; Jones, R. G.; Keddie, D. J.; Luscombe, C. K.; Matson, J. B.; Matyjaszewski, K.; Merna, J.; Moad, G.; Nakano, T.; Penczek, S.; Russell, G. T.; Topham, P. D. Terminology for Chain Polymerization (IUPAC Recommendations 2021). *Pure Appl. Chem.* **2022**, *94* (9), 1093–1147. https://doi.org/10.1515/pac-2020-1211.
(80) Moad, G. Terminology in Reversible Deactivation Radical Polymerization (RDRP) and Reversible Addition–Fragmentation Chain Transfer (RAFT) Polymerization. In *RAFT Polymerization*; 2021; pp 15–24. https://doi.org/10.1002/9783527821358.ch2.
(81) Penczek, S.; Moad, G. Glossary of Terms Related to Kinetics, Thermodynamics, and Mechanisms of Polymerization (IUPAC Recommendations 2008). *Pure Appl. Chem.* **2008**, *80* (10), 2163–2193. https://doi.org/10.1351/pac200880102163.
(82) Jenkins, A. D.; Jones, R. G.; Moad, G. Terminology for Reversible-Deactivation Radical Polymerization Previously Called "Controlled" Radical or "Living" Radical Polymerization (IUPAC Recommendations 2010). *Pure Appl. Chem.* **2009**, *82* (2), 483–491. https://doi.org/10.1351/PAC-REP-08-04-03.
(83) Goto, A.; Fukuda, T. Kinetics of Living Radical Polymerization. *Prog. Polym. Sci.* **2004**, *29* (4), 329–385. https://doi.org/10.1016/j.progpolymsci.2004.01.002.

(84) Matyjaszewski, K. General Concepts and History of Living Radical Polymerization. In *Handbook of Radical Polymerization*; 2002; pp 361–406. https://doi.org/10.1002/0471220450.ch8.
(85) Wang, J.-S.; Matyjaszewski, K. Controlled/"living" Radical Polymerization. Atom Transfer Radical Polymerization in the Presence of Transition-Metal Complexes. *J. Am. Chem. Soc.* **1995**, *117* (20), 5614–5615. https://doi.org/10.1021/ja00125a035.
(86) Kato, M.; Kamigaito, M.; Sawamoto, M.; Higashimura, T. Polymerization of Methyl Methacrylate with the Carbon Tetrachloride/Dichlorotris- (Triphenylphosphine)Ruthenium(II)/Methylaluminum Bis(2,6-Di-Tert-Butylphenoxide) Initiating System: Possibility of Living Radical Polymerization. *Macromolecules* **1995**, *28* (5), 1721–1723. https://doi.org/10.1021/ma00109a056.
(87) Rizzardo, E.; Hill, W. 73) Assignee: Commonwealth Scientific and Industrial Research Organization,.
(88) Chiefari, J.; Chong, Y. K. (Bill); Ercole, F.; Krstina, J.; Jeffery, J.; Le, T. P. T.; Mayadunne, R. T. A.; Meijs, G. F.; Moad, C. L.; Moad, G.; Rizzardo, E.; Thang, S. H. Living Free-Radical Polymerization by Reversible Addition−Fragmentation Chain Transfer: The RAFT Process. *Macromolecules* **1998**, *31* (16), 5559–5562. https://doi.org/10.1021/ma9804951.
(89) Le Tam, P.; Moad, G.; Rizzardo, E.; Thang, S. H. Polymerization with Living Charachteristics. WO/9801478, January 1998.
(90) Fischer, H. The Persistent Radical Effect: A Principle for Selective Radical Reactions and Living Radical Polymerizations. *Chem. Rev.* **2001**, *101* (12), 3581–3610. https://doi.org/10.1021/cr990124y.
(91) Perrier, S. 50th Anniversary Perspective</i> : RAFT Polymerization—A User Guide. *Macromolecules* **2017**, *50* (19), 7433–7447. https://doi.org/10.1021/acs.macromol.7b00767.
(92) Barner-Kowollik, C. *Handbook of RAFT Polymerization*; Wiley: Germany, 2008.
(93) Van Hook, J. P.; Tobolsky, A. V. The Thermal Decomposition of 2,2'-Azo-Bis-Isobutyronitrile. *J. Am. Chem. Soc.* **1958**, *80* (4), 779–782. https://doi.org/10.1021/ja01537a006.
(94) McKenzie, T. G.; Fu, Q.; Uchiyama, M.; Satoh, K.; Xu, J.; Boyer, C.; Kamigaito, M.; Qiao, G. G. Beyond Traditional RAFT: Alternative Activation of Thiocarbonylthio Compounds for Controlled Polymerization. *Adv. Sci.* **2016**, *3* (9), 1500394. https://doi.org/10.1002/advs.201500394.
(95) Zheng, H.; Bai, W.; Hu, K.; Bai, R.; Pan, C. Facile Room Temperature RAFT Polymerization via Redox Initiation. *J. Polym. Sci. Part Polym. Chem.* **2008**, *46* (7), 2575–2580. https://doi.org/10.1002/pola.22590.
(96) Reyhani, A.; McKenzie, T. G.; Ranji-Burachaloo, H.; Fu, Q.; Qiao, G. G. Fenton-RAFT Polymerization: An "On-Demand" Chain-Growth Method. *Chem. – Eur. J.* **2017**, *23* (30), 7221–7226. https://doi.org/10.1002/chem.201701410.
(97) Nothling, M. D.; McKenzie, T. G.; Reyhani, A.; Qiao, G. G. Tunable, Quantitative Fenton-RAFT Polymerization via Metered Reagent Addition. *Macromol. Rapid Commun.* **2018**, *39* (19), 1800179. https://doi.org/10.1002/marc.201800179.
(98) Eggers, S.; Abetz, V. Hydroperoxide Traces in Common Cyclic Ethers as Initiators for Controlled RAFT Polymerizations. *Macromol. Rapid Commun.* **2018**, *39* (7), 1700683. https://doi.org/10.1002/marc.201700683.
(99) Fantin, M.; Isse, A. A.; Venzo, A.; Gennaro, A.; Matyjaszewski, K. Atom Transfer Radical Polymerization of Methacrylic Acid: A Won Challenge. *J. Am. Chem. Soc.* **2016**, *138* (23), 7216–7219. https://doi.org/10.1021/jacs.6b01935.
(100) Chmielarz, P.; Fantin, M.; Park, S.; Isse, A. A.; Gennaro, A.; Magenau, A. J. D.; Sobkowiak, A.; Matyjaszewski, K. Electrochemically Mediated Atom Transfer Radical Polymerization (eATRP). *Prog. Polym. Sci.* **2017**, *69*, 47–78. https://doi.org/10.1016/j.progpolymsci.2017.02.005.

(101) De Bon, F.; Isse, A. A.; Gennaro, A. Electrochemically Mediated Atom Transfer Radical Polymerization of Methyl Methacrylate: The Importance of Catalytic Halogen Exchange. *ChemElectroChem* **2019**, *6* (16), 4257–4265. https://doi.org/10.1002/celc.201900192.
(102) Wang, Y.; Fantin, M.; Park, S.; Gottlieb, E.; Fu, L.; Matyjaszewski, K. Electrochemically Mediated Reversible Addition–Fragmentation Chain-Transfer Polymerization. *Macromolecules* **2017**, *50* (20), 7872–7879. https://doi.org/10.1021/acs.macromol.7b02005.
(103) Lorandi, F.; Fantin, M.; Shanmugam, S.; Wang, Y.; Isse, A. A.; Gennaro, A.; Matyjaszewski, K. Toward Electrochemically Mediated Reversible Addition–Fragmentation Chain-Transfer (*e* RAFT) Polymerization: Can Propagating Radicals Be Efficiently Electrogenerated from RAFT Agents? *Macromolecules* **2019**, *52* (4), 1479–1488. https://doi.org/10.1021/acs.macromol.9b00112.
(104) Strover, L. T.; Postma, A.; Horne, M. D.; Moad, G. Anthraquinone-Mediated Reduction of a Trithiocarbonate Chain-Transfer Agent to Initiate Electrochemical Reversible Addition–Fragmentation Chain Transfer Polymerization. *Macromolecules* **2020**, *53* (23), 10315–10322. https://doi.org/10.1021/acs.macromol.0c02392.
(105) Chen, M.; Zhong, M.; Johnson, J. A. Light-Controlled Radical Polymerization: Mechanisms, Methods, and Applications. *Chem. Rev.* **2016**, *116* (17), 10167–10211. https://doi.org/10.1021/acs.chemrev.5b00671.
(106) Corrigan, N.; Shanmugam, S.; Xu, J.; Boyer, C. Photocatalysis in Organic and Polymer Synthesis. *Chem. Soc. Rev.* **2016**, *45* (22), 6165–6212. https://doi.org/10.1039/C6CS00185H.
(107) Konkolewicz, D.; Schröder, K.; Buback, J.; Bernhard, S.; Matyjaszewski, K. Visible Light and Sunlight Photoinduced ATRP with Ppm of Cu Catalyst. *ACS Macro Lett.* **2012**, *1* (10), 1219–1223. https://doi.org/10.1021/mz300457e.
(108) Fors, B. P.; Hawker, C. J. Control of a Living Radical Polymerization of Methacrylates by Light. *Angew. Chem. Int. Ed.* **2012**, *51* (35), 8850–8853. https://doi.org/10.1002/anie.201203639.
(109) Dadashi-Silab, S.; Atilla Tasdelen, M.; Yagci, Y. Photoinitiated Atom Transfer Radical Polymerization: Current Status and Future Perspectives. *J. Polym. Sci. Part Polym. Chem.* **2014**, *52* (20), 2878–2888. https://doi.org/10.1002/pola.27327.
(110) Miyake, G. M.; Theriot, J. C. Perylene as an Organic Photocatalyst for the Radical Polymerization of Functionalized Vinyl Monomers through Oxidative Quenching with Alkyl Bromides and Visible Light. *Macromolecules* **2014**, *47* (23), 8255–8261. https://doi.org/10.1021/ma502044f.
(111)Treat, N. J.; Sprafke, H.; Kramer, J. W.; Clark, P. G.; Barton, B. E.; Read de Alaniz, J.; Fors, B. P.; Hawker, C. J. Metal-Free Atom Transfer Radical Polymerization. *J. Am. Chem. Soc.* **2014**, *136* (45), 16096–16101. https://doi.org/10.1021/ja510389m.
(112) Xu, J.; Shanmugam, S.; Duong, H. T.; Boyer, C. Organo-Photocatalysts for Photoinduced Electron Transfer-Reversible Addition–Fragmentation Chain Transfer (PET-RAFT) Polymerization. *Polym. Chem.* **2015**, *6* (31), 5615–5624. https://doi.org/10.1039/C4PY01317D.
(113) Theriot, J. C.; Lim, C.-H.; Yang, H.; Ryan, M. D.; Musgrave, C. B.; Miyake, G. M. Organocatalyzed Atom Transfer Radical Polymerization Driven by Visible Light. *Science* **2016**, *352* (6289), 1082–1086. https://doi.org/10.1126/science.aaf3935.
(114) Quinn, J. F.; Barner, L.; Barner-Kowollik, C.; Rizzardo, E.; Davis, T. P. Reversible Addition−Fragmentation Chain Transfer Polymerization Initiated with Ultraviolet Radiation. *Macromolecules* **2002**, *35* (20), 7620–7627. https://doi.org/10.1021/ma0204296.
(115) Otsu, T.; Yoshida, M. Role of Initiator-Transfer Agent-Terminator (Iniferter) in Radical Polymerizations: Polymer Design by Organic Disulfides as Iniferters. *Makromol. Chem. Rapid Commun.* **1982**, *3* (2), 127–132. https://doi.org/10.1002/marc.1982.030030208.
(116) Otsu, T. Iniferter Concept and Living Radical Polymerization. *J. Polym. Sci. Part Polym. Chem.* **2000**, *38* (12), 2121–2136. https://doi.org/10.1002/(SICI)1099-0518(20000615)38:12<2121::AID-POLA10>3.0.CO;2-X.

(117) McKenzie, T. G.; Fu, Q.; Wong, E. H. H.; Dunstan, D. E.; Qiao, G. G. Visible Light Mediated Controlled Radical Polymerization in the Absence of Exogenous Radical Sources or Catalysts. *Macromolecules* **2015**, *48* (12), 3864–3872. https://doi.org/10.1021/acs.macromol.5b00965.
(118) Xu, J.; Shanmugam, S.; Corrigan, N. A.; Boyer, C. Catalyst-Free Visible Light-Induced RAFT Photopolymerization. In *Controlled Radical Polymerization: Mechanisms*; ACS Symposium Series; American Chemical Society, 2015; Vol. 1187, pp 247–267. https://doi.org/10.1021/bk-2015-1187.ch013.
(119) Lee, Y.; Boyer, C.; Kwon, M. S. Photocontrolled RAFT Polymerization: Past, Present, and Future. *Chem. Soc. Rev.* **2023**, *52* (9), 3035–3097. https://doi.org/10.1039/D1CS00069A.
(120) Xu, J.; Jung, K.; Atme, A.; Shanmugam, S.; Boyer, C. A Robust and Versatile Photoinduced Living Polymerization of Conjugated and Unconjugated Monomers and Its Oxygen Tolerance. *J. Am. Chem. Soc.* **2014**, *136* (14), 5508–5519. https://doi.org/10.1021/ja501745g.
(121) Phommalysack-Lovan, J.; Chu, Y.; Boyer, C.; Xu, J. PET-RAFT Polymerisation: Towards Green and Precision Polymer Manufacturing. *Chem. Commun.* **2018**, *54* (50), 6591–6606. https://doi.org/10.1039/C8CC02783H.
(122) Bellotti, V.; Simonutti, R. New Light in Polymer Science: Photoinduced Reversible Addition-Fragmentation Chain Transfer Polymerization (PET-RAFT) as Innovative Strategy for the Synthesis of Advanced Materials. *Polymers* **2021**, *13* (7). https://doi.org/10.3390/polym13071119.
(123) Tian, X.; Ding, J.; Zhang, B.; Qiu, F.; Zhuang, X.; Chen, Y. Recent Advances in RAFT Polymerization: Novel Initiation Mechanisms and Optoelectronic Applications. *Polymers* **2018**, *10* (3). https://doi.org/10.3390/polym10030318.
(124) Allegrezza, M. L.; Konkolewicz, D. PET-RAFT Polymerization: Mechanistic Perspectives for Future Materials. *ACS Macro Lett.* **2021**, *10* (4), 433–446. https://doi.org/10.1021/acsmacrolett.1c00046.
(125) Strover, L. T.; Cantalice, A.; Lam, J. Y. L.; Postma, A.; Hutt, O. E.; Horne, M. D.; Moad, G. Electrochemical Behavior of Thiocarbonylthio Chain Transfer Agents for RAFT Polymerization. *ACS Macro Lett.* **2019**, *8* (10), 1316–1322. https://doi.org/10.1021/acsmacrolett.9b00598.
(126) Strieth-Kalthoff, F.; Glorius, F. Triplet Energy Transfer Photocatalysis: Unlocking the Next Level. *Chem* **2020**, *6* (8), 1888–1903. https://doi.org/10.1016/j.chempr.2020.07.010.
(127) Mazzucato, M.; Isse, A. A.; Durante, C. Dissociative Electron Transfer Mechanism and Application in the Electrocatalytic Activation of Organic Halides. *Curr. Opin. Electrochem.* **2023**, *39*, 101254. https://doi.org/10.1016/j.coelec.2023.101254.
(128) Marcus, R. A.; Sutin, N. Electron Transfers in Chemistry and Biology. *Biochim. Biophys. Acta BBA - Rev. Bioenerg.* **1985**, *811* (3), 265–322. https://doi.org/10.1016/0304-4173(85)90014-X.
(129) Marcus, R. A. Calculation of Thermodynamic Properties of Polyelectrolytes. *J. Chem. Phys.* **1955**, *23* (6), 1057–1068. https://doi.org/10.1063/1.1742191.
(130) Hush, N. S. Adiabatic Rate Processes at Electrodes. I. Energy-Charge Relationships. *J. Chem. Phys.* **1958**, *28* (5), 962–972. https://doi.org/10.1063/1.1744305.
(131) Antonello, S.; Maran, F. Intramolecular Dissociative Electron Transfer. *Chem. Soc. Rev.* **2005**, *34* (5), 418. https://doi.org/10.1039/b300085k.
(132) Bao, D.; Millare, B.; Xia, W.; Steyer, B. G.; Gerasimenko, A. A.; Ferreira, A.; Contreras, A.; Vullev, V. I. Electrochemical Oxidation of Ferrocene: A Strong Dependence on the Concentration of the Supporting Electrolyte for Nonpolar Solvents. *J. Phys. Chem. A* **2009**, *113* (7), 1259–1267. https://doi.org/10.1021/jp809105f.
(133) Bard, A. J.; Faulkner, L. R. *Electrochemical Methods: Fundamentals and Applications.*, 2nd ed.; Wiley: Germany, 2001.

(134) Li, H.; Wenger, O. S. Photophysics of Perylene Diimide Dianions and Their Application in Photoredox Catalysis. *Angew. Chem. Int. Ed.* **2022**, *61* (5), e202110491. https://doi.org/10.1002/anie.202110491.
(135) Marcus, R. A. On the Theory of Oxidation-Reduction Reactions Involving Electron Transfer. I. *J. Chem. Phys.* **1956**, *24* (5), 966–978. https://doi.org/10.1063/1.1742723.
(136) Alam, Md. S.; Ashokkumar, B.; Siddiq, A. M. The Density, Dynamic Viscosity and Kinematic Viscosity of Protic and Aprotic Polar Solvent (Pure and Mixed) Systems: An Experimental and Theoretical Insight of Thermophysical Properties. *J. Mol. Liq.* **2019**, *281*, 584–597. https://doi.org/10.1016/j.molliq.2019.02.097.
(137) Bortolamei, N.; Isse, A. A.; Gennaro, A. Estimation of Standard Reduction Potentials of Alkyl Radicals Involved in Atom Transfer Radical Polymerization. *Electrochimica Acta* **2010**, *55* (27), 8312–8318. https://doi.org/10.1016/j.electacta.2010.02.099.
(138) Pedersen, S. U.; Lund, T.; Norin, T.; Csöregh, I.; Ertan, A.; Kleinpeter, E. Homogeneous Rate Constants for Coupling between Electrochemically Generated Aromatic Anion Radicals and Alkyl Radicals. *Acta Chem. Scand.* **1991**, *45*, 397–402. https://doi.org/10.3891/acta.chem.scand.45-0397.
(139) Pedersen, S. U.; Lund, T.; Daasbjerg, K.; Pop, M.; Fussing, I.; Lund, H.; Mikkelsen, K. V.; Senning, A. Kinetic Studies of the Homogeneous Coupling Reaction between Electrochemically Generated Aromatic Radical Anions and Alkyl Radicals. *Acta Chem. Scand.* **1998**, *52*, 657–671. https://doi.org/10.3891/acta.chem.scand.52-0657.
(140) Lund, H.; Daasbjerg, K.; Lund, T.; Occhailini, D.; Pedersen, S. U.; Niinistö, L.; Styring, S.; Tommos, C.; Warncke, K.; Wood, B. R. On Radical Anions in Elucidation of Mechanisms of Organic Reactions. *Acta Chem. Scand.* **1997**, *51*, 135–144. https://doi.org/10.3891/acta.chem.scand.51-0135.
(141) Valencia, D. P.; González, F. J. Estimation of Diffusion Coefficients by Using a Linear Correlation between the Diffusion Coefficient and Molecular Weight. *J. Electroanal. Chem.* **2012**, *681*, 121–126. https://doi.org/10.1016/j.jelechem.2012.06.013.
(142) Enemærke, R. J.; Christensen, T. B.; Jensen, H.; Daasbjerg, K. Application of a New Kinetic Method in the Investigation of Cleavage Reactions of Haloaromatic Radical Anions†. *J. Chem. Soc. Perkin Trans. 2* **2001**, No. 9, 1620–1630. https://doi.org/10.1039/b102835a.
(143) Isse, A. A.; Lin, C. Y.; Coote, M. L.; Gennaro, A. Estimation of Standard Reduction Potentials of Halogen Atoms and Alkyl Halides. *J. Phys. Chem. B* **2011**, *115* (4), 678–684. https://doi.org/10.1021/jp109613t.
(144) Kojima, H.; Bard, A. J. Determination of Rate Constants for the Electroreduction of Aromatic Compounds and Their Correlation with Homogeneous Electron Transfer Rates. *J. Am. Chem. Soc.* **1975**, *97* (22), 6317–6324. https://doi.org/10.1021/ja00855a005.
(145) Donkers, R. L.; Maran, F.; Wayner, D. D. M.; Workentin, M. S. Kinetics of the Reduction of Dialkyl Peroxides. New Insights into the Dynamics of Dissociative Electron Transfer [1]. *J. Am. Chem. Soc.* **1999**, *121* (31), 7239–7248. https://doi.org/10.1021/ja9906148.
(146) Saveant, J. M. A Simple Model for the Kinetics of Dissociative Electron Transfer in Polar Solvents. Application to the Homogeneous and Heterogeneous Reduction of Alkyl Halides. *J. Am. Chem. Soc.* **1987**, *109* (22), 6788–6795. https://doi.org/10.1021/ja00256a037.
(147) Saveant, J. M. Dissociative Electron Transfer. New Tests of the Theory in the Electrochemical and Homogeneous Reduction of Alkyl Halides. *J. Am. Chem. Soc.* **1992**, *114* (26), 10595–10602. https://doi.org/10.1021/ja00052a065.
(148) Rumble, J. *Handbook of Chemistry and Physiscs*, 105th ed.; CRC, 2024.
(149) Isse, A. A.; Gennaro, A.; Lin, C. Y.; Hodgson, J. L.; Coote, M. L.; Guliashvili, T. Mechanism of Carbon−Halogen Bond Reductive Cleavage in Activated Alkyl Halide Initiators Relevant to Living Radical Polymerization: Theoretical and Experimental Study. *J. Am. Chem. Soc.* **2011**, *133* (16), 6254–6264. https://doi.org/10.1021/ja110538b.

(150) Cardinale, A.; Isse, A. A.; Gennaro, A.; Robert, M.; Savéant, J.-M. Dissociative Electron Transfer to Haloacetonitriles. An Example of the Dependency of In-Cage Ion-Radical Interactions upon the Leaving Group. *J. Am. Chem. Soc.* **2002**, *124* (45), 13533–13539. https://doi.org/10.1021/ja0275212.
(151) Beatty, J. W.; Stephenson, C. R. J. Amine Functionalization via Oxidative Photoredox Catalysis: Methodology Development and Complex Molecule Synthesis. *Acc. Chem. Res.* **2015**, *48* (5), 1474–1484. https://doi.org/10.1021/acs.accounts.5b00068.
(152) Marcus, R. A. On the Theory of Electron-Transfer Reactions. VI. Unified Treatment for Homogeneous and Electrode Reactions. *J. Chem. Phys.* **1965**, *43* (2), 679–701. https://doi.org/10.1063/1.1696792.
(153) Nicholson, R. S. Theory and Application of Cyclic Voltammetry for Measurement of Electrode Reaction Kinetics. *Anal. Chem.* **1965**, *37* (11), 1351–1355. https://doi.org/10.1021/ac60230a016.

Appendix

A – Experimental data of CV analysis for targeted substrates

Here are reported all the voltametric data with relative simulations used for the evaluation of $k_{cat,I}$ values relative to Ehtyl-αbromoisobutyrate (EBiB) and Bromoacetonitrile (BrACN)

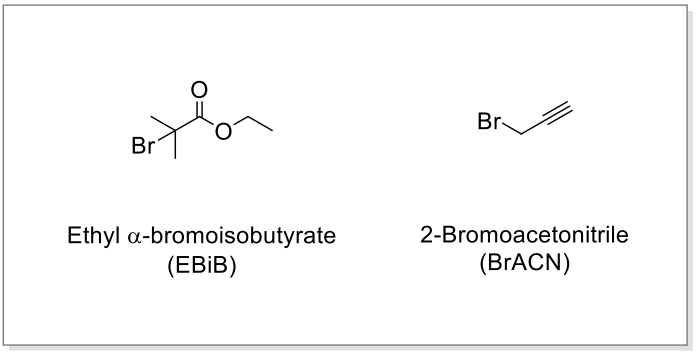

EBiB:

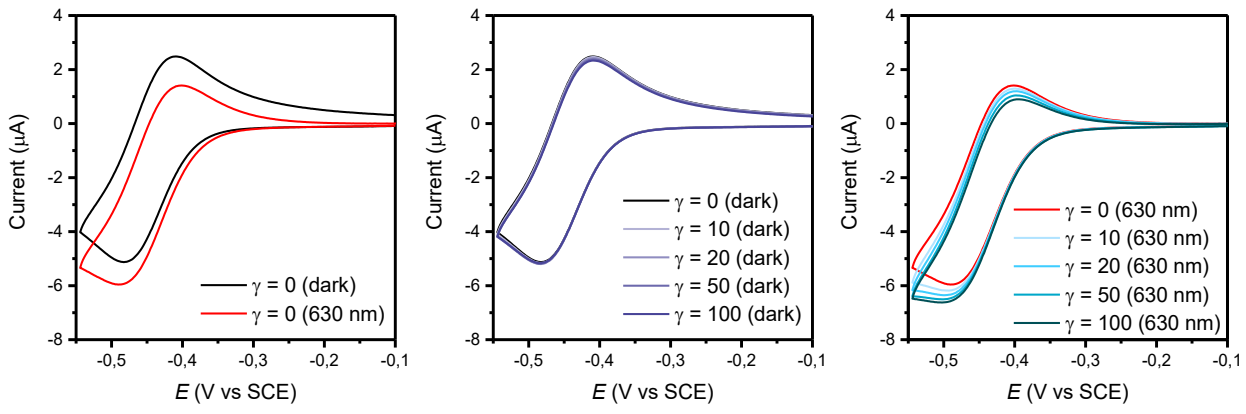

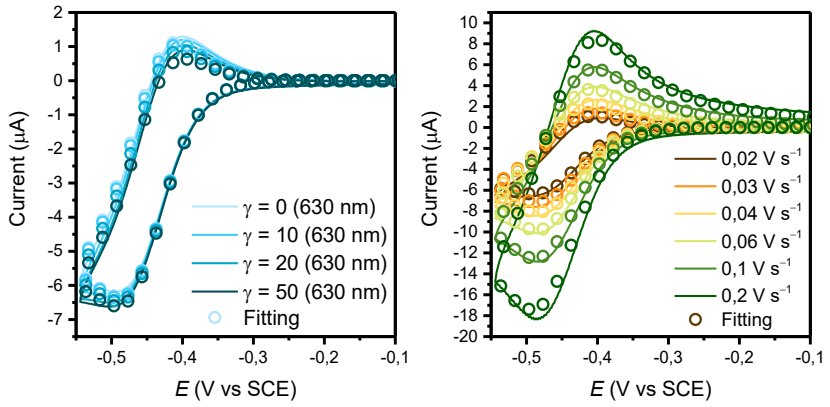

BrACN:

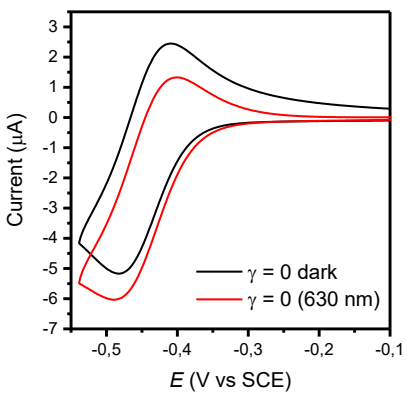
Current (µA)
E (V vs SCE)
γ = 0 dark
γ = 0 (630 nm)

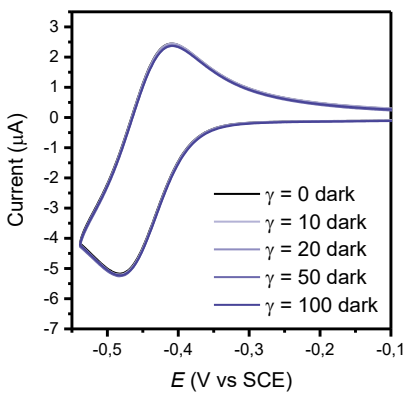
Current (µA)
E (V vs SCE)
γ = 0 dark
γ = 10 dark
γ = 20 dark
γ = 50 dark
γ = 100 dark

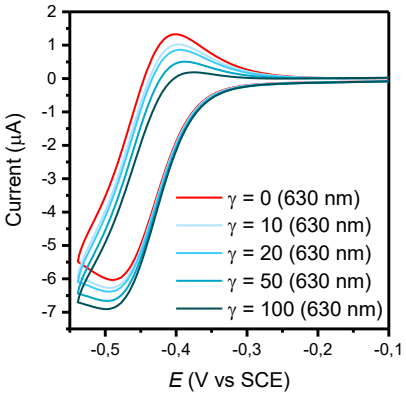
Current (µA)
E (V vs SCE)
γ = 0 (630 nm)
γ = 10 (630 nm)
γ = 20 (630 nm)
γ = 50 (630 nm)
γ = 100 (630 nm)

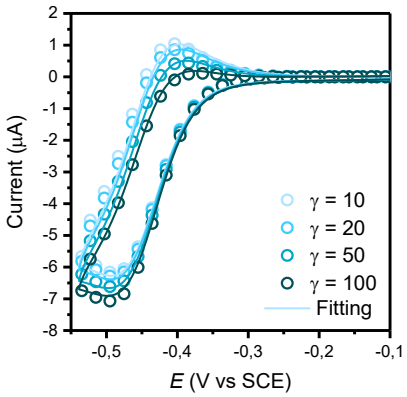
Current (µA)
E (V vs SCE)
γ = 10
γ = 20
γ = 50
γ = 100
Fitting

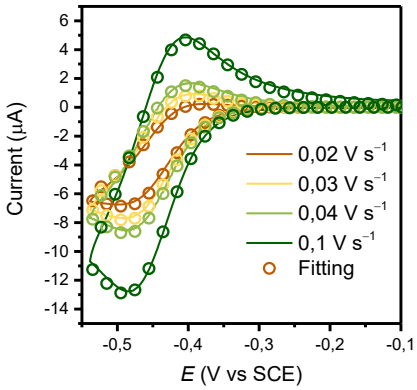
Current (µA)
E (V vs SCE)
0,02 V s−1
0,03 V s−1
0,04 V s−1
0,1 V s−1
Fitting

B – Determination of the heterogeneous electron transfer rate constant

The electron transfer rate constant (k_s) measures the rate of electron transfer (ET) from the electrode to the redox species, depending on the energy barrier and system reorganization after changes in oxidation state and charge. This barrier includes internal reorganization (changes in bond angles/lengths), often negligible for metal complexes but significant for alkyl halides, and external reorganization (movement of surrounding solvation sphere molecules)[152], which affects ET rates based on the solvent and electrolyte. For slow ET with high activation energy, cyclic voltammetry shows a completely irreversible signal.

For quasi-reversible electron transfers, cyclic voltammetry can assess the ET rate, as the voltammogram shape depends on the kinetic parameter Ψ and the transfer coefficient α. The response varies with the scan rate: higher rates allow less time for the redox species and its solvation sphere to reorganize, making the system appear more irreversible. Using the Nicholson method, ET kinetics can be evaluated by examining how the peak separation (ΔE_p) changes with the scan rate[133]:

$$\Psi = \frac{\left(\frac{D_O}{D_R}\right)^{\alpha/2} k_s}{\left[\left(\frac{nF}{RT}\right)\pi D_O v\right]^{1/2}} \quad \text{(B.1)}$$

Theoretical data[153] linking ΔE_p to Ψ, are the basis for estimating k_s for a quasi-reversible ET. The equation B.1 for Ψ can be simplified by assuming that the diffusion coefficients of the oxidized and reduced species (D_O and D_R) are equal:

$$\Psi = \frac{k_s}{\left[\left(\frac{nF}{RT}\right)\pi D_O v\right]^{1/2}} \quad \text{(B.2)}$$

Plotting theoretical values of ΔE_p against log(Ψ) yields a working curve fitted by a fifth-degree polynomial (Figure 43a):

$$y = 0{,}08391 - 0{,}05274x + 0{,}05387x^2 - 0{,}02649x^3 - 0{,}00086x^4 + 0{,}00411x^5 \quad \text{(B.3)}$$

Where $y = \Delta E_p$ and $x = \log\Psi$.

Experimental ΔE_p values can be fitted to the theoretical curve to determine k_s (Figure 43b and c). A series of voltammograms is recorded at different scan rates, measuring ΔE_p for each rate to calculate the parameter log(Ψ′):

$$\log \Psi' = \log\left\{\frac{1}{\left[\left(\frac{nF}{RT}\right)\pi D_O v\right]^{1/2}}\right\} \tag{B.4}$$

The resulting k_s value for both heterogeneous electron transfer reactions is 0,0108 ± 0,0003 cm s^{-1}.

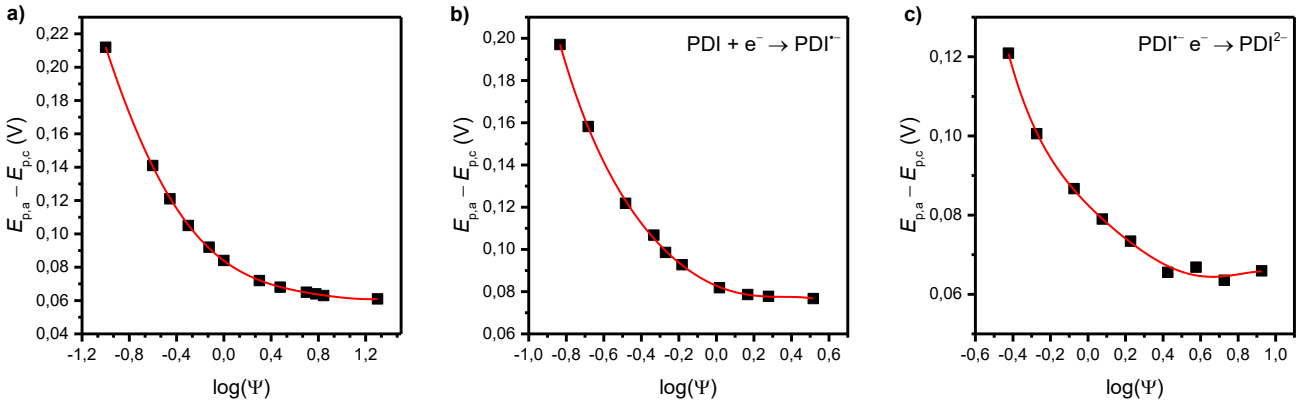

Figure 43. Fitting of a) literature data, b) data relative to the first reversible reduction of PDI and c) data relative to the second reversible reduction of PDI.

C – Two-photon ATRP experiments

In addition to what reported in Section 3.3.1 (here entry 1, Table 11), other experiments were conducted to evaluate the two-photon ATRP mechanisms. The results are reported in Table 11.

Table 11. Two-photon ATRP experiments. [a]

Entry	[MMA]:[RX]:[PDI]	RX	Conv (%)[b]	$M_{n,th}$[c]	$M_{n,GPC}$[d]	$M_{w,GPC}$[d]	$Đ$[d]	I*(%)[e]
1	100:1:0,01	EBP	63,7	6440	10500	21800	2,06	59,1
2*	200:1:10:0,02	MBP	20,2	2147	18614	39500	2,12	/
3	200:1:5:0,01	MBP	91,2	9101	16441	11230	1,50	96,
4	200:1:5:0,01	MBP	85,3	n.a.	n.a.	n.a.	1,94	n.a.

[a] Conditions: 2,5 mL of solvent (DMF) + 2,5 mL of MMA; degassing by FPT cycles; irradiation with a Kessil 456 nm LED at 5 cm distance and 100% intensity; room temperature. [b] Calculated after 6h via ^{1}H NMR (400 Mhz). [c] Calculated as Conv×MW_{MMA}×$[MMA]_0/[RX]$ + MW_{RX} Determined after 7h by Gel Permeation Chromatography in DMF (PMMA standard, 60°C). [e] $I^*=(M_{n,th}/M_{n,GPC})\times100$. * Polymerization stopped after 4,5h.

The reported experiments exhibited poor control over the polymerization process, consistently with the hypothesized absence of an effective deactivation pathway.

D – Determination of absolute irradiance for the used light sources

The effective irradiance of used LEDs was measured with a portable UV-Vis probe.

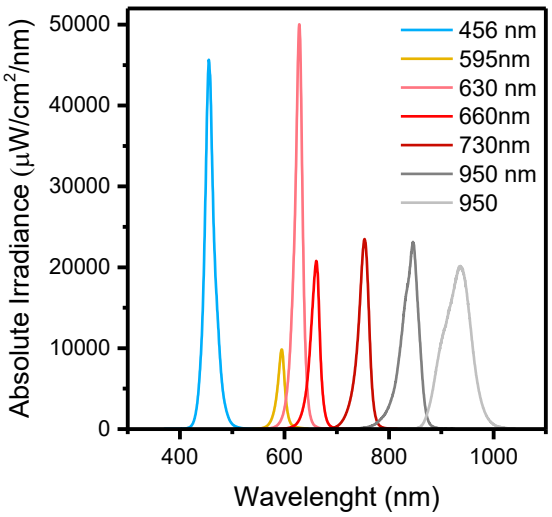

Figure 44. Measured irradiance for the used light sources recorded with the portable spectrometer AvaSpec (Avantes)

From the integral of the experimental data in Figure 44 it is possible to obtain the absolute irradiance in W cm^{-2} (Table 12).

Table 12. Absolute irradiance for the used light sources.

λ (nm)	Absolute irradiance (W cm^{-2})
456	1,08
595	0,18
630	0,98
660	0,48
730	0,63
850	0,90
950	1,28